Republic of Iraq

Ministry of Higher Education and Scientific Research

University of Babylon / College of Science

Department of Physics

Fabrication of Multilayer Solar Cell Based on n-Si Substrate

A Thesis Submitted to the Council of College of Science, University of Babylon in Partial Fulfillment of the Requirements of the Degree of Doctor of Philosophy in Physics

by

Inass Abdulah Zgair Taha

B.Sc. in Physics 2005
M.Sc. in Physics 2015

Supervised by

Prof. Dr. **Abdulazeez O. Mousa Al-Ogaili**

Prof. Dr. **Khalid Haneen Abass Hassan**

2023 A.D. **1445 A.H.**

﴿ يَرْفَعِ اللهُ الَّذِينَ آَمَنُوا مِنكُمْ والَّذينَ أُوتُوا الْعِلْمَ دَرَجَاتٍ وَاللهُ بِمَا تَعْمَلُونَ خَبِير﴾

صدق الله العلي العظيم

سُورَة المجادلة آيه (١١)

Supervisors Certification

We certify that this thesis is titled (**Fabrication of Multilayer Solar Cell Based on n-Si Substrate**) will be prepared by (**Inass Abdulah Zgair Taha**) under our supervision at Department of Physics, College of Science, University of Babylon, as a partial fulfillment of the requirements of Ph.D. degree in Physics.

Signature:

Supervisor: **Dr. Abdulazeez O. Mousa Al-Ogaili**

Title: Professor

Address: Department of Physics - College of Science - University of Babylon

Date: / / 2023

Signature:

Supervisor: Dr. Khalid Haneen Abass Hassan

Title: Professor

Address: Department of physics- College of Education for Pure Sciences -University of Babylon

Date: / / 2023

Certification of the Head of the Department

In view of the available recommendation, I forward latter thesis for debate by the examination committee.

Signature

Name: Dr. Samira Adnan Mahdi

Title: Assistant Professor

Address: Head of Physics Department, College of Science, University of Babylon

Date: / / 2023

Dedication

To the memory of my father

my mother

To my close friends

Inass

Acknowledgments

In the name of Allah (the Almighty), Great is the most gracious and the most merciful. Praise be to Allah (the Almighty), the lord of earth and heaven, for completing my dissertation.

I would like to thank my supervisors, Prof. Dr. Abdulazeez O. Mousa Al-Ogaili, and Prof. Dr. Khalid Haneen Abass Hassan for suggesting this topic to me and for their distinguished efforts and sound advice and directions that helped me. In alleviating all the difficulties, I encountered during my work.

I would like to express my deep gratitude and appreciation to the staff in the Department of Physics, College of Science, University of Babylon, and College of Education for Pure Sciences, University of Babylon for offering me the opportunity to complete my study.

My deep thanks to all the staff of the Faculty of Science, University of Kufa, especially, Prof. Dr. Adel H.Omran Al-khayatt, Prof. Dr. Sadiq Kadhum Lafta Al-Zurfi and Lecturer Ameer Farhan Shamkhi for their help throughout the thesis. I wish success to all.

I Apologize for those I haven't mentioned, so My thankfulness to all who took part in this achievement.

Inass

Summary

In this work, Cuprous oxide (Cu_2O), Tin Sulfide (SnS), Cuprous oxide / Tin sulfide (Cu_2O/SnS), and Cuprous oxide: Tin sulfide (Cu_2O:SnS) thin films have been deposited onto glass and silicon substrates using thermal evaporation technique at (1×10^{-7}) mbar and annealed at 200 °C for 2h. Structural, optical, and electrical properties of Cu_2O, SnS, Cu_2O /SnS, and Cu_2O: SnS thin films were investigated and analyzed before and after annealing process.

X-ray diffraction (XRD) results indicated that the structure of all fabricated thin films was polycrystalline in nature and Cu_2O thin films have cubic phase and SnS thin films belonging to the Orthorhombic phase. The values of the average crystalline size of Cu_2O thin films increased from (12 to 16) nm and reduced from (14 to 11) nm, (14 to 12) nm, and (16 to 12) nm for SnS, Cu_2O/SnS, and Cu_2O:SnS thin films, respectively.

The field emission scanning electron microscope (FESEM) image for Cu_2O thin films indicates that the grain size increased after the annealing process, while for SnS, Cu_2O/SnS, and Cu_2O: SnS thin films decreased. The morphology of the thin films appeared relatively uniformly coated. Atomic force microscopy (AFM) results showed that the surface of the films that deposited on a glass substrate has a smooth surface structure.

The absorption coefficient and transmittance spectra were recorded in the wavelength range (300–1100) nm, which exhibited that the absorption edges of Cu_2O thin films were shifted toward longer wavelength after

annealing, while SnS, Cu_2O/SnS, and Cu_2O:SnS thin films was shifted toward shorter wavelength**.**

The energy gap for allowed direct transition decreased from (2.57 to 2.15) eV with respect to the annealing process. The energy gap of SnS thin films was increased from (1.53 to 1.8) eV, energy gap of Cu_2O/SnS increased from (1.75 to 1.80) eV and for Cu_2O: SnS thin films show an increase in energy gap from (3.66 to 3.86) eV after the annealing process. In addition, the effect of annealing process on the optical constant (refractive index and extinction coefficient) have been studied.

The results of Hall measurements varied between an increase and a decrease in Hall parameters such as charge carrier concentration, Hall coefficient, and mobility after the annealing process.

The C-V measurement is indicated that type of heterojunction is abrupt and the maximum value of the built in potential (V_{bi}) belong to SnS/Si solar cell by (0.21) volt. The current– voltage (I–V) characteristics of the solar cells were measured at illumination 100 mW/cm^2.

The results showed that the efficiency of the Cu_2O/n-Si solar cell is (3.37) %, while the SnS/n-Si and Cu_2O/SnS/n-Si solar cells have an efficiency of (6.27) % and (4.62) %, respectively. The highest value for efficiency was for the Cu_2O:SnS/n-Si solar cell about (7.44) %, the value of the short circuit current was (24) mA, the open circuit voltage was (500) mV, and fill factor was 0.99.

Contents

List of Tables

List of Figures

List of Symbols

Symbol	Physical meaning
Voc	Open Circuit Voltage
Isc	Short Current Circuit
F.F	Fill Factor
R_{SH}	Shunt Resistance
R_S	Series Resistance
d	Inter Plane Distance
m	Diffraction Order
θ	Bragg's Angle
D.	Average Crystallite Size
β	FWHM: Full Width at Half Maximum
δ	Dislocation Density
ε	Micro Strain
E_g	Energy Gap
λ	Wavelength
λ_c	Cut off Wavelength
c	Velocity of Light
α	Absorption Coefficient
t	Thickness
I_o	Incident Intensity of Light
I	Transmittance Intensity of Light
hυ	Photon Energy
γ	Constant
A	Absorbance

Symbol	Physical meaning
T	Transmittance
R	Reflectance
ñ	Complex Refractive Index
n	Refractive Index
K_o	Extinction Coefficient
J	Current Density
A	Area
K_B	Boltzmann's Constant
T	Temperature
I_{gen}	Generated Current
I_{sat}	Saturation Current
q	Electron Charge
P_{max}	Maximum Power
I_{max}	Maximum Current
V_{max}	Maximum Voltage
P_{out}	Output Power
P_{in}	Incident Power
η	Efficiency
E_H	Electric Field of Hall
R_H	Hall Coefficient
V_H	Hall Voltage
W	Distance Between Two Electrodes
B	Magnetic Field
n	Electrons Concentration

Symbol	Physical meaning
$\boldsymbol{p}$	Hole Concentration
μ_H	Hall Mobility
$\sigma_{R.T}$	Conductivity at Room Temperature
R**T**	Room Temperature
ρ	Resistivity
a	Cross section area
Re	Resistance
L	Conductor Lenght
E	Electric Field
μ	Mobility
μ_n	Mobility of Electrons
μ_h	Mobility of Holes
ν_n	Electrons Velocity
ν_p	Holes Velocity
M.P	Melting Point
m	Mass of the Evaporated Material
ρ	Density of Material
L	Distance Between the Substrate and the Boat

List of Abbreviations

Symbol	Physical meaning
XRD	X-Ray Diffraction
AFM	Atomic Force Microscope
FESEM	Field Emission Scanning Electron Microscope
(FWHM)	Full Width at Half Maximum
(EDX)	Energy-Dispersive Spectroscope
RMS	Root Mean Square
Vis	Visible Spectrum
UV	Ultra Violet Spectrum
I-V	Current –Voltage
C-V	Capacity – Voltage
AM1.5G	Global Horizontal Irradiance Spectrum
C.B	Conduction Band
V.B	Valance Band

Chapter One

Introduction

1.1 Introduction

The major challenges today are meeting rising energy demand and addressing climate change, as well as the depletion of nonrenewable fossil fuels and global warming. Renewable energy sources are one of the alternative solutions to mitigate all of the above. Renewable energy sources like wind, solar, hydropower, and geothermal are growing rapidly as viable alternatives to traditional fossil fuel sources. Solar energy is considered the most environment-friendly and cost-effective of all renewable energy sources, and it has the potential to provide an unlimited supply of energy with minimal environmental impact [1].

The sun is regarded as the most plentiful source of clean, renewable energy, and solar energy has received considerable interest due to its sustainability. This makes solar cell technology economically feasible and sustainable and enables possible reductions in harmful gas emissions, making it a perfect source of energy that avoids energy and environmental risks [1,2]. Solar cells are the fundamental element of photovoltaic modules which are otherwise named solar panels. Solar cells are referred to be photovoltaic regardless of whether the source of the light is sunlight or an artificial source [3].

In 1954, Chapin *et al*. discovered the first practical solar cell, this discovery was regarded at that time as a very significant invention that leads to converting light directly into electricity. This discovery came after the observation of the photovoltaic effect by Becquerel in 1839. Furthermore, it was supported by Adams and Day when they created the first solid-state solar cell in 1877, a diode device utilizing the chemical element selenium [4].

Solar cells are categorized into three generations: The first-generation cells, also known as traditional, conventional, or wafer-based cells, are composed of crystalline silicon, the widely dominant PV technology, which comprises materials such as mono-crystalline silicon and poly-crystalline silicon [5]. The second generation of solar cells is made from non-silicon materials, such as cadmium telluride (CdTe), copper indium gallium selenide (CIGS), and amorphous silicon [6]. Such solar cells are composed of thin layers with thick a few micrometers deposited sequentially on a large, cost-effective substrate constructed of polymer, metal, or glass. Third generation solar cells: these technologies include polymer solar cells, dye- sensitized hybrid solar cells, photo-electrochemical cells, and nanocrystal solar cells [7,8].

1.2 Tin Sulfide (SnS)

In recent years, semiconductors with layered structures that belong to IV–VI group drawn much interest due to their adequate characteristics like absorbance, high optical transmittance, energy band gap, and electrical futures control for photovoltaic, thermoelectric, and optoelectronic devices. Among them, tin monosulfide (SnS) has gained a great deal of interest in recent years [9,10].

Tin sulfide (SnS), a material that is abundantly available and environmentally friendly, can be employed as an absorber for low-cost thin film photovoltaic cells. In particular, its band gap is situated between Si and GaAs, which is considered one of the pioneering materials in solar energy conversion. Loferski diagrams show that this compound has a theoretical light conversion efficiency of more than 24% [11, 12].

Tin sulfide (SnS) exhibits p-type electrical conduction. Since SnS possesses high optical absorption coefficient ($> 10^4$ cm^{-1}) in the visible and

near-infrared spectral regions, making it an attractive absorber material for photovoltaic applications, owing to the values of direct and indirect band gap between (1.3–1.5) eV and (1.0–1.1) eV, respectively [13,14]. The crystal structure of SnS compound is orthorhombic as shown in Fig. (1-1), where lattice parameters an unit cell are (a = 4.334, b = 11.200, and c = 3.987) nm and this crystal structure can be seen as a distorted rock salt (NaCl) and each layers held together by weak Van der Waals forces [15].

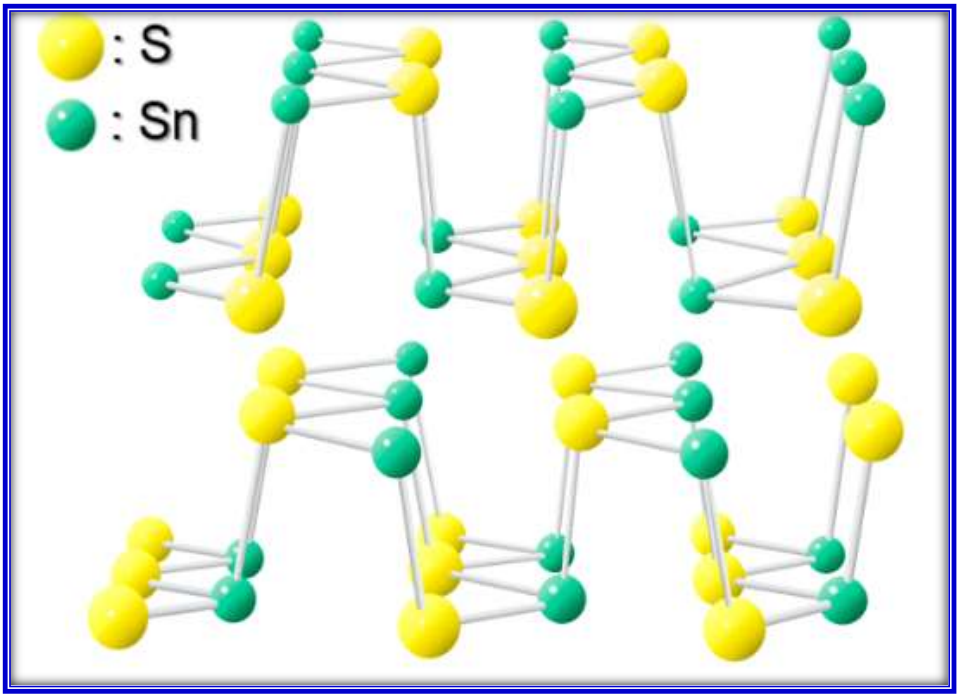

Fig.(1-1): Structure of the orthorhombic SnS crystal [16].

Because of the presence of weak force in SnS layers the surface of material is chemically inert and does not have any dangling bond or surface density state. Consequently, the surface of SnS is liberated from Fermi level pinning. This fact renders SnS chemically and ecologically inert [17]. Table (1-1) tabulated some of the physical characteristics of tin sulfide.

Table (1-1): Physical properties of tin sulfide [18-20].

Property	Values
Conductivity type	Usually p-type and n-type
Structure	Orthorhombic Polycrystalline a=4.334nm, b=11.200 nm and c = 3.987 nm
Indirect bandgap	((1.0-1.1)± 0.02) eV
Direct bandgap	((1. 3-1.5)± 0.2) eV
Carrier concentration	5×10^{17} cm^{-3}
Refractive index	3.5
Resistivity	0.06 Ω.cm
Hole mobility	54 cm^2 V^{-1} S^{-1} , 2000 cm^2 V^{-1} s^{-1}
Absorption coefficient	2×10^4 cm^{-1}
Density	5.22 g/cm^3
Melting point	882 °C
Boling point	1230 °C
Molecular weight	150.77 g/mol

1.3 Cuprous Oxide (Cu_2O)

Metal oxides (MOs) are a significant category of functional materials with various magnetic, electrical, structural and optical characteristics as semiconductors, they are significant materials for photovoltaic applications [21]. Cuprous Oxide (Cu_2O) is a suitable candidate among these oxides due to its non-toxicity, high absorption coefficient high hole mobility and abundance of constituent elements in the earth's crust [22]. Cuprous oxide is an inherent p-type semiconductor due to the high concentration of negatively charged copper vacancies and presumably the presence of interstitial oxygen imperfections [23].

The structure of cuprous oxide is characterized by a cubic unit cell that has a lattice constant of 4.2696 Å and is belongs to the Pn3m space group and each of its unit cells are two ions of copper and four ions of oxygen. These are organized in a cubic lattice structure together with oxygen atoms, and they are surrounded tetrahedrally by copper ions [24]. Its direct bandgap of 2.1 eV is relatively big for a perfect match of the solar spectrum, yet it nevertheless permits a theoretical maximum power conversion efficiency of 20% for a single junction under AM1.5 illumination.

In addition, at energies that lie above the bandgap, the material has a high absorption coefficient in the visible area ($>10^4$ cm^{-1}) consequently, this material is an appropriate absorber for thin-film solar cell [25,26]. Some of physical properties of Cu_2O are listed in Table (1-2).

Table (1-2): Physical properties of cuprous oxide [27,28].

Property	Values
Conductivity type	Usually p-type
Structure	Cubic, a = (4.2696 ±0.0010) Å
Indirect bandgap	1.4 eV
Direct bandgap	2.0 eV to 2.60 eV
Carrier Concentration	1.2×10^{15} cm^{-3}
Refractive index	2.705
Resistivity	2.8×10^{2} Ω·cm
Hole mobility	30, 100, 53 $cm^2 V^{-1} s^{-1}$
Absorption coefficient	$10^4 - 10^5$ cm^{-1}
Density	(5.749–6.140) g/cm^3
Melting point	1232°C
Boling point	1800°C
Molecular weight	143.09 g/mol

1.4 Nanomaterials

Nanomaterials are crystalline or amorphous particles of organic or inorganic materials with dimensions between (1 and 100) nm [29]. Nanomaterials are categorized as either nanophase or nanostructured materials. The former typically refers to dispersive nanoparticles, whereas the latter is composed of dense bulk materials with grain sizes in the nanometer range of size. Nanomaterials may exist in three dimensions as particles, two dimensions as strands or fibres , or one dimension as surface films. They could be found in agglomerated or aggregated,single, or fused forms with irregular shapes, tubular and spherical. The Nanotubes, quantum dots, and fullerenes are common nanomaterial categories [30].

According to the number of dimensions in the nano range (less than 100 nm), nanomaterials are categorized as seen in Fig. (1-2) [30].

a- Zero-dimensional nanomaterials (0-D): the nanomaterials in this class have all their three dimensions in the nanoscale range. Examples are quantum dots, fullerenes, and nanoparticles.

b- One-dimensional nanomaterials (1-D): the nanomaterials in this class have one dimension outside the nanoscale. Examples are nanotubes, nanofibers, nanorods, and nanowires.

c- Two-dimensional nanomaterials (2-D): the nanomaterials in this class have two dimensions outside the nanoscale. Examples are nanosheets, nanofilms, and nanolayers.

d- Three-dimensional nanomaterials (3-D) or bulk nanomaterials: in this class the materials are not confined to the nanoscale in any dimension. This class contains bulk powders, dispersions of nanoparticles, arrays of nanowires and nanotubes, etc.

The nanomaterials can be polycrystalline, crystalline or amorphous. They may be made up of a single phase or multiple phases of chemical elements. There are numerous methods for producing nanostructures; bucky balls, nanoparticles, nanotubes, and macromolecules can be synthesized artificially for specific materials [30,31].

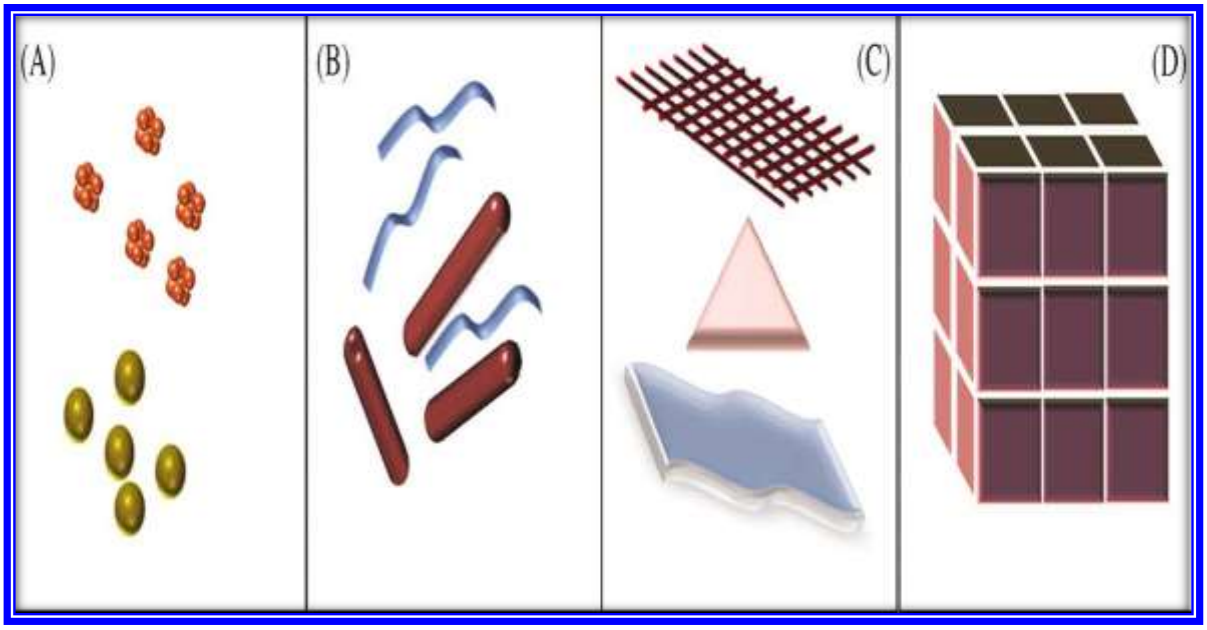

Fig. (1-2): Classification of nanomaterials (a) 0D nanomaterials; (b) 1D nanomaterials; (c) 2D nanomaterials; (d) 3D nanomaterials [31].

1.5 Synthesis of Nanomaterials Methods

In general, top-down and bottom-up are the two main approaches for nanomaterials synthesis [32].

a. Top-down: size reduction from bulk materials.

b. Bottom-up: material synthesis from atomic level.

Top-down approach are included in the typical solid –state processing of the materials. This approach is based with the bulk material and makes it smaller, thus breaking up larger particles by the use of physical processes like crushing, milling or grinding. Usually this approach is not suitable for

preparing uniformly shaped materials, and it is very difficult to realize very small particles even with high energy consumption [31]. The biggest problem with top-down approach is the imperfection of the surface structure. Such imperfection would have a significant impact on physical properties and surface chemistry of nanostructures and nanomaterials. It is well known that the conventional top-down technique can cause significant crystallographic damage to the processed patterns. There are many examples of this method such as etching , laser ablation , lithography and milling [29,32].

Bottom –up approach refers to the build-up of a material from the bottom: atom-by-atom, molecule-by-molecule or cluster-by-cluster. This route is more often used for preparing most of the nano-scale materials with the ability to generate a uniform size, shape and distribution. It effectively covers chemical synthesis and precisely controlled the reaction to inhibit further particle growth. Although the bottom-up approach is nothing new, it plays an important role in the fabrication and processing of nanostructures and nanomaterials. Synthesis of nanoparticles to have a better control over particles size distribution, morphology, purity, quantity and quality, by employing environment friendly economical processes has always been a challenge for the researchers [32]. The sol gel is an example of this method. Fig. (1-3) show the two methods for prepared nanomaterials..

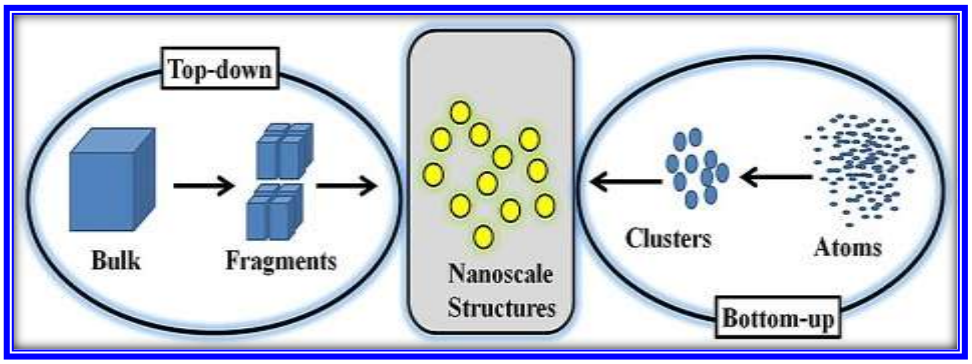

Fig.(1-3): Top-down and bottom-up synthesis schemes[33].

1.6 Literature Survey

This section highlights the previous research on the growth and the preparation of Cuprous Oxide and Tin Sulfide thin film and its implementation as a solar cell.

In (2010), Mc-Shane ***et al.,*** [34] made-up Cu_2O-based p-n homojunction solar cell using consecutive electrochemical deposition method, where p-Cu_2O layer deposited onto n-Cu_2O layer, surface morphology was adjusted to study how it affected the solar cell's performance, and the p-n interface was determined. Their results indicated that even though the resistivity of both the n- and p-layers stayed comparable, cell efficiency and junction quality differed considerably based on the faces of the crystals displayed at the p-n junction. The best value of performance obtained for the fabricated p-n homojunction solar cells was open circuit voltage (V_{oc}) = 0.423 V, fill factor (F.F) = 27%, short circuit current density (J_{SC}) = 2.5 mA/cm^2, and efficiency (η) = 0.29%. They revealed that the higher resistivity of the two n and p-layers was the basic limiting factor for the cell's efficiency.

In (2014), Dimopoulos ***et al.,*** [35] manufactured heterojunction solar cell via electrochemical deposition, where they coated p-type Cu_2O absorbers onto sputtered n-type ZnO layers. Under AM1.5G illumination and for the deposited cells, they obtained the solar cell parameters, which were V_{oc} = 0.37 V, F.F = 35.7%, J_{SC} = 3.71 mA/cm^2, and η = 0.49%. From thermal annealing that occurred in a vacuum and at temperatures reaching 300°C, the compositional purity of the cuprous oxide absorber has been obtained. After annealing samples at temperatures around 300 °C, the parameter values of

the solar cell significantly increased to V_{OC} = 0.505 V, F.F = 47.1%, J_{SC} = 4.67 mA/cm^2, and η = 1.12%.

In (2015), Kawano ***et al.,*** [36] employed thermal evaporation to form SnS films on glass substrates at varying growth temperatures between (100 and 250) °C. The SnS thin film formed at 100 °C was observed to have small crystal grains. In contrast, when the preparation temperature of the SnS films was raised to 225 °C, denser and larger crystal grains were formed while maintaining the same compositions when the temperature exceed 225 °C, the SnS started to re-evaporate from the films. At temperature around 200 ^oC the films gained the highest value of Hall mobility. The optimal temperature for the formation of SnS via evaporation is 200 °C and this temperature results in large and compact crystal grains as well as the maximum Hall mobility, which contributes to the 2.53% efficiency of SnS thin-film solar cells.

In (2015) El-Shaer ***et al.,***[37] prepared of p-Cu_2O and n-Cu_2O thin films using electrochemical deposition technique by utilizing various conditions for every type and with varying film thickness. By successively depositing n-Cu_2O layer on top of p-Cu_2O layer, homojunction Cu_2O solar cells were effectively constructed. After that, the gold evaporates onto the n-Cu_2O layer by thermal evaporation. The best value of parameters of p/n Cu_2O cell were Voc= 31.5 mV, J_{SC} =12.7 mA/cm^2, F.F= 35% , and η = 0.14%under typical testing conditions for thicknesses of 2μm for n- Cu_2O and 0.7μm for p- Cu_2O.

In (2017) Samani ***et al.,*** [38] used thermal evaporation technique in order to fabricate SnS thin films onto a substrates of glass and there after annealed the samples at various temperatures ranging from 100 °C, 200

°C, 300 °C and 400 °C with an incremental of 100 °C for 1 hour. X-ray diffraction (XRD) examines indicate that the structural features of SnS film have enhanced with rising annealing temperature, and the grain size has increased, the energy band gap of a film as-prepared, which increases noticeably with rising annealing temperature, has been measured to be in the range of 1.60 eV to 2.06 eV and both the index of refraction and extinction coefficient fall significantly.

In (2018), Hamood ***et al.,*** [39] prepared SnS:Ag thin films under pressure reaching 1×10^{-6} mbar onto glass slides using thermal evaporation process, then annealed them at various temperatures 423 K, 473 K, 573 K and 623 K for 2 hours. X-ray diffraction analysis shows the principal peak (111), which occurs at an annealing temperature of 623 K, as well as the secondary peaks (101) and (002) with a crystal size of (3–7) nm. The energy band gap was 2.1 eV for the deposited film and it grew to be 3.3 eV after it was annealed at 623 K.

In (2018), Hegde ***et al.,*** [40] used thermal evaporation to deposit Tin Sulfide onto glass substrates at 300 °C followed by an annealing process at a range of temperatures from (100 to 300) °C for 2 hours. The average particle size decreased from 265 nm for as-prepared films to 132.8 nm for films annealed at 300 °C, according to optical properties measurements the band gap value decreases marginally with annealing temperature and remained within the range of (1.33–1.2) eV. After annealing SnS films at 300 °C, their electrical characteristics improved, where the value mobility reached 36.9 cm^2 V/s, the electrical resistivity was 7.8 Ω.cm, and the carrier concentration of the p-type was about 2.17 10^{16} cm^{-3}.

In (2019), Tafti ***et al.,*** [41] deposited thin films of SnS/CdS on a glass substrate via thermal evaporation followed by annealing at various temperatures in order to optimize the optical characteristics of the material, for application in devices of photovoltaic solar cell. The effect of annealing on the optical characteristics of a SnS/CdS film was investigated at temperatures ranging from (100 to 400) °C in 100 °C increments. Optical constants such like extinction coefficient, refractive index and band gap were computed at various annealing temperatures and in the (250-750) nm wavelength range. For a film as-deposited, the energy band gap ranges between 2.20 eV and 3.18 eV, which rises with increasing annealing temperature while both the index of refraction and the coefficient of extinction decrease significantly.

In (2020), Cho ***et al.,*** [42] used the vapor transport deposition method to manufacture SnS/CdS devices. The decrease in interface imperfections of the heterojunction, which may take place through the deposition process of transparent electrodes or due to direct annealing that occurs at 300 °C for the SnS/CdS heterojunction, leads to the enhancement of the efficiency of the SnS/CdS solar cell. The SnS/CdS device has an F.F of 0.588, a J_{SC} of 20.76 mA cm^{-2}, a V_{OC} of 0.346 V, and an efficiency of more than 4%, according to the results. The significant loss in a large short-circuit current, as observed by optical analyses and quantum efficiency, is primarily due to recombination.

In (2020), Tuama ***et al.,*** [43] prepared Cu_2O:(Ag NPs)/Si films with thickness of about 60 nm by technique of thermal evaporation. The XRD analysis indicated that the manufactured films had an amorphous nature, and

the grain size was measured to be between (9.2 and 18.4) nm, which is equivalent to that obtained from the FESEM measurement. It was established that the samples had an optical bandgap that ranged from (2.79 to 3.42) eV and that was the main factor in altering and enhancing the Cu_2O optical characteristics by doping and selecting the optimal ones to manufacture high efficiency and low cost solar cell. The conversion efficiency of (3.5) obtained by doping 0.04% Ag to Cu_2O, which is thought to be very efficient relative to the total efficiency of Cu_2O solar cells.

In (2020), Jayathilaka ***et al.,*** [44] deposited Cu_2O homojunction thin film onto a Ti substrate by an electrochemical deposition technique, and by using controlled bath conditions, a p-Cu_2O layer was coated onto a n-Cu_2O layer. The crystallinity and morphology of the samples by high-energy X-ray diffraction (HEXRD), X-ray diffraction (XRD), and scanning electron microscope (SEM) were investigated. Current density–voltage analysis (J-V) demonstrated that the photocurrent was improved tenfold compared with an unannealed and untreated homojunction solar cell. Transient measurements revealed that the sulfur-treated p-type Cu_2O substantially decreased recombination, hence increasing the efficiency of the solar cell. The best open-circuit voltage, short-circuit current density, and conversion efficiency of 490 mV, 12.8 mA/cm^2, and 2.64%, respectively, under AM1.5 illumination, were achieved by an annealed sulfur-treated solar cell of Ti/n-Cu_2O/p-Cu_2O/Au.

In (2021), Nguyen ***et al.,*** [45] used a radio frequency sputtering technique to deposit a SnS/Ag/SnS trilayer film. They studied the influence of Ag films on the physical characteristics of the SnS films. The Ag/SnS film-

based solar cell showed improved photovoltaic performance compared to the SnS film-based solar cell. The density of short circuit current and efficiency gained by the solar cell of SnS/Ag/SnS trilayer films are around 17.13 mA/cm^2 and 5.24%, respectively, which are higher than the values gotten by the SnS films solar cell, which were Jsc = 14.21 mA/cm^2 and η =3.23%.The enhanced photo-current density, chiefly caused by the improvement of the efficiency separating photo-generated electron-hole pairs and the reduction in entrapment charge carriers in impurity centers, in addition to the decrease in the current of leakage in the active area can be observed.

In (2021), Kawanishi ***et al.,*** [46] prepared a p-n homojunction SnS solar cell by depositing thin films of polycrystalline p-type SnS onto single crystals of n-type SnS. The J_{SC} of the SnS homojunction solar cell is approximately 7.5 mA /cm^2, the F.F. is approximately 53%, and the V_{OC} is approximately 360 mV. The built-in potential of a p-type SnS or n-type SnS cell was around 0.92 eV, where this value is near enough to the band gap energy of tin sulfide, which is 1.1 eV, and it is larger than the value that belongs to the heterojunctions, which is 0.7 eV. They illustrate that the efficiency obtained of the homojunction solar cell was 1.4%, which is lower than the record for heterojunctions, which was (4–5) %, basically owing to the low I_{SC} of 7.5 mA/cm^2.

In (2021), Zaki ***et al.,*** [47] studied tin sulfide materials as a p-type layer in heterojunction solar cells that have a structure of SnS/Si and study the influence of annealing as well as the influence of substrate type on SnS films. SnS films changed to the Sn_2S_3 phase when deposited onto a Si substrate after thermal treatment, while they kept the same preferred orientation when

deposited onto a glass substrate. The intensity of observed reflections in XRD charts decreased with increasing temperature of annealing (Ta) and the treated SnS film at Ta = 673 K showed an absence of ordered structure. After annealing, the band gap energy increased from (1.29 to 1.50) eV, and the behavior of thermally induced electrical for SnS samples revealed the presence of deep imperfection levels. The obtained parameters of prepared Al/n-Si/p-SnS/In solar cells are Rsh, Rs, Jsc, Voc, and η are each 209.2 Ωcm^2, 91.15 Ω cm^2, 2.52 mA, 0.27 V, and 0.21% respectively.

In (2021), Alagarasan ***et al.,*** [48] deposited SnS thin films using vacuum thermal evaporation onto glass substrates at 10^{-5} Torr with various range of substrate temperatures ranging 50 °C to 200 °C with steps of 50 °C. Standard characterization methods were used to examine the optical and structural, characteristics of substrate temperature-effected SnS films. Crystal structure analysis by (XRD) exposed that the fabricated films had a polycrystalline orthorhombic structure. The optical characteristics, such as absorption coefficient, refractive index, optical band gap, and extinction coefficient, of the thin films are expected from the optical measurements. The values of the optical band gap were measured to be between 1.843 eV and 2.075 eV make it an attractive material for use in visible light photodetectors.

In (2021), BalaKarthikeyan ***et al.,*** [49] made up SnS thin films at room temperature by using the thermal evaporation method, and after that, the films were annealed at altering temperatures from 200 °C to 350 °C for application in photodetector devices. According to XRD measurements, the produced films exhibit the orthorhombic phase of pristine SnS without the presence of any impurity phases. The thin films of SnS that annealed at 300°C exhibit the

largest crystallite size among of all the samples that were manufactured. Morphological consequences demonstrate that the SnS samples display a homogeneous of 2D petal-like shape with varied size. The UV-Vis studies show that the values of bandgap decrease as the annealing temperature of the samples increase would be better suited for photodetector applications.

In (2023), Abass ***et al.,*** [50] coated SnS: Ag thin films onto glass and silicon substrates for fabricating SnS: Ag solar cells by employing the method of thermal evaporation. The crystallization of the films resulted in their polycrystalline and orthorhombic form, according to an XRD analysis. The size of the crystallite increase from (3.7096 to 10.4716) nm and SnS: Ag film (6 wt.%) exhibits larger grains, according to AFM images. The Hall effect analysis confirmed that the conductivity of the film is p-type. The optical bandgap values were determined to be in the range of (2.6–1.7) eV. Owing to highly absorbing and polycrystalline, thin films of SnS could be employed to make heterojunction solar cells. The fill factor of the produced solar cells reached 0.46 and an efficiency of 5.4% for SnS: Ag (6 wt.%) /Si solar cell.

In (2023), Abdurrahman, ***et al.,*** [51] fabricated a photoactive substance comprising of Bi/Cu_2O/Bi solar cell by using an easy, dependable, and cost-effective thermal oxidation process and method of the powder vaporization. The maximum power points of (P_{max}) were also documented as well as the current-voltage characteristic curves. A a short circuit current of (I_{sc} =14.45) mA, open circuit voltage around (V_{OC} = 7.24) V, and the point of maximum power of (P_{max}= 0.476) W have been acquired correspondingly. I-V characteristic showed typical rectification behavior of a p-n junction for the fabricated structure, indicating that Bi/Cu_2O/Bi solar cell was formed as a

semiconducting material and post transition metal has positive impingement on the sample which yields to the stability of the sample. The fabricated cell produced a power conversion efficiency of 1.14%.

1.7 Aims of the Work

The aims of this study are focused on the following points:

1- The aim of this work is to deposite Cu_2O, SnS, Cu_2O/SnS, and Cu_2O:SnS thin films on different substrates by thermal evaporation technique.

2- Study structural, morphology, and optical properties of deposited and annealed thin films.

3- The purpose of this work is fabrication and characterization Cu_2O/Si, SnS/Si, Cu_2O/SnS/Si, and Cu_2O:SnS/Si as solar cells.

4- Study I-V and C-V curves properties for the synthesis solar cells and evaluate the values of fill factor, short-circuit current and open circuit voltage, and efficiency of the fabricated solar cells.

Chapter Two

Theoretical Part

2.1 Introduction

This chapter concentrates on the description of thin films and the thermal evaporation technique for fabricating thin films and then discusses which diagnostic tools to examine these parameters. This leads to a natural demarcation of the analytical tools, including structural, and optical for deposited thin films, as well as photovoltaic measurements for fabricated heterojunctions solar cell. Finally, this chapter gives a general description of all the equations, relations, employed in the thesis.

2.2 Thin Films

The term of "Thin Films" is used to describe a layer or several layers of atoms for a certain substance whose thickness less than (1μm) [52]. The characteristics of a thin film can be quite different from the bulk material properties, since thin films have a large surface area to bulk volume ratio. The morphology, structure, physical and chemical characteristics of the thin film can also be quite different from those of the bulk materials [53]. The structure and properties of many films are known to depend considerably on the state of the surface on which they are deposited to know exactly what kind of surface is being used for deposition of films, whether it is crystallographically oriented or not [54].

Thin films are used to enhance the properties of bulk materials by depositing a layer with the desired physical and chemical characteristics to improve their functionality. Thin films have a wide range of properties that can be used in a variety of applications. Types of thin films can be categorized as follows [55].

Optical thin films: Used to create reflective coatings, anti-reflective coatings, solar cells, Monitors, waveguides and optical detector arrays.

Electrical or electronic thin films: Used to make insulators, conductors, semiconductor devices, integrated circuits and piezoelectric devices.

Magnetic thin films: Usually used to make memory disks.

Chemical thin films: They are used to create resistance to alloying, diffusion, corrosion and oxidation, as well as to make gas and liquid sensors.

Mechanical thin films: Tribological coatings to protect against abrasion, increase hardness and adhesion and use of micro-mechanical properties.

Thermal thin films: They are used to create insulation layers and heat sinks

2.3 Thermal Evaporation

Vacuum evaporation is based on a thermal principle grounded on two elementary processes. First, a heating that allows the material to reach its melting point, then, in a second time, its vaporization point. Then, this first process is followed by the solid-state condensation of the material evaporated on the substrate to be covered. The vaporization of the source material can be generated by Joule effect, by induction or by using an intense and energetic electron beam. As well as the depositions are carried out under high vacuum in order to impart high purity to the layers [56,57]. Thermal evaporation is a particularly popular method but the main weaknesses of this technique are, the need to use sufficient power to vaporize the most refractory compounds, and the deposition of alloys may be disturbed if the different compounds have very different melting temperatures and / or saturation vapor pressures. The thermal evaporation technique is the simplest method of depositing substances onto a substrate at a pressure of 10^{-7} mbar, with exceptional film purity. Fig.(2-1) depicts the structure of a fundamental coating system [58,59].

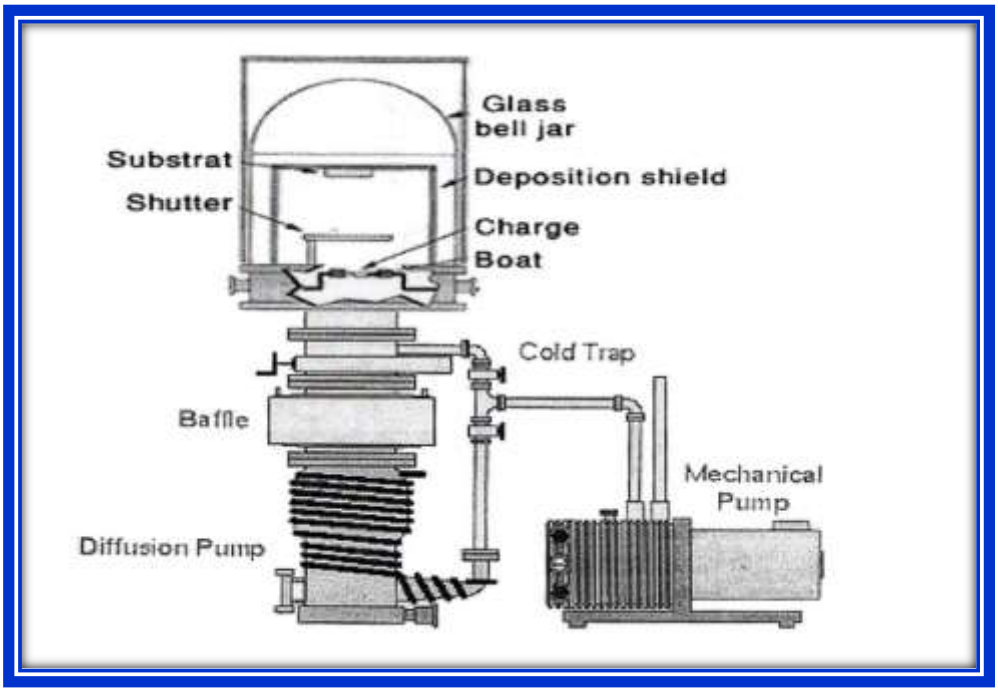

Fig. (2-1):Design of a fundamental coating system [59].

2.4 Basic Theory of Characterization Techniques of Thin Film

In recent years, scientific progress has mainly taken place through the discovery of new materials. The comprehensive characterization of any material includes phase analysis, structural, surface characterization, and compositional, all of which have a significant impact on the characteristics of the material. The various analytical approaches that were used in the characterization of the thin films are discussed in this chapter.

2.4.1 Structural and Morphological Characterization

A series of structural, morphological, and optical characterization was carried out by various characterization methods in order to extract quantitative or qualitative information about thin films. X- ray diffraction (XRD) was used to examine the films' structural features. Field emission

scanning electron microscope (FESEM) and atomic force microscope (AFM) were used to study the surface morphology of thin films.

2.4.1.1 Basic Theory of X-ray Diffraction (XRD)

X-ray diffraction is a comprehensive method used to investigate a variety of structural characteristics in crystalline materials. The information obtainable ranges from microscopic characteristics, such as the arrangement of crystal components, to macroscopic characteristics, such as the crystal size and the mean shape. X-ray diffraction is generally utilized for phase identification of crystalline substances, where Bragg reflections that are associated with a crystal structure can provide a unique fingerprint of unit cell dimensions. A crystal structure could be considered to be a collection of planes or layers, all of which behave as a semi-transparent mirror. Bragg's diffraction law is the fundamental work principle of this technology [60,61]. When X-ray radiation (which has a wavelength equal to the spacing between atoms in crystals) hits a crystalline substance, the radiation is scattered by that of the electrons surrounding each atom. Collective constructive scattering can occur depending on the angle between the incoming radiation and the atomic planes as shown in Fig. (2-2) [62]:

$$2d_{(hkl)}sin\theta = m\lambda \qquad (2-1)$$

Where, $d_{(hkl)}$ is the inter planes distance between consecutive crystal planes, θ is Braggs angle which represent the angle between the incident X-ray beam and the plane of scattering , m is integer representing the diffraction peaks order and λ denoted to the wavelength of incident X-ray incident.

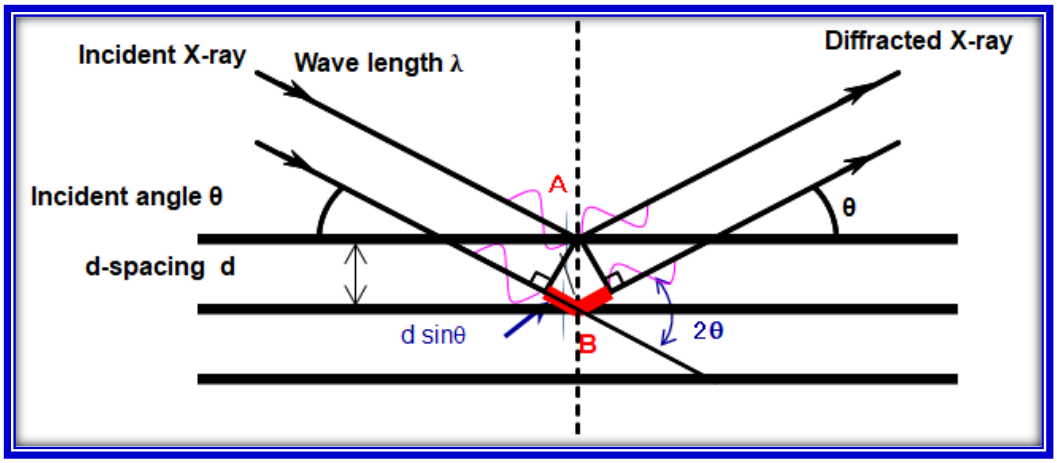

Fig. (2-2): Schematic of Braggs law [62].

The crystallite size could be calculated using Debye Scherrer's formula [63,64].

$$D = \frac{0.9\,\lambda}{\beta\ COS\theta} \qquad (2-2)$$

Where λ denoted to X-ray's wavelength used, β signified to (FWHM) which is abbreviation to (full-width at half-maximum) of the diffraction peak and θ° denoted to Bragg's angle.

The dislocation density (δ), was evaluated using the formula of Williamson and Smallman's and is represented as the number of dislocation lines per unit volume [65].

$$\delta = \frac{1}{D^2} \qquad (2-3)$$

Micro-strain in films occurs during thin film growth and is produced by stretching or compression in the lattice, causing a variation in the orthorhombic structure's c-lattice constant. This micro strain can be calculated from the relation [66].

$$\varepsilon = \frac{\beta\cos\theta}{4} \qquad (2-4)$$

The known crystal phases for SnS have had an orthorhombic structure.

By obtaining the lattice constants from the X-ray pattern and employing the following formula, the orthorhombic phase (a≠ b ≠c) is described as [67]:

$$\frac{1}{d^2} = \frac{h^2}{a^2} + \frac{k^2}{b^2} + \frac{l^2}{c^2} \qquad (2-5)$$

While Cu_2O have a cubic crystal structure (a = b = c) [67].

$$\frac{1}{d^2} = \frac{h^2+k^2+l^2}{a^2} \qquad (2-6)$$

Where a, b and c represents lattice parameters.

2.4.1.2 Basic Theory of Field Emission Scanning Electron Microscope (FESEM)

Scanning electron microscopy (FESEM) is an ultra-high resolution type of electron microscopy that is capable of producing images of greater than 300,000 times magnification. This gives it an effective resolution approaching 1 nanometer, making it possible to capture images of features close to the electron tunneling limit. Such an incredible resolution is made possible because electrons have wavelengths much shorter than the optical diffraction limit of approximately 250 nm [68].

Thus, FESEM is a popular imaging technology for probing features smaller than those accessible by optical microscopy. Furthermore, as electrons have unique quantum interactions with different chemical elements, most SEMs also include additional detectors that allow for characterization beyond simple imaging. The FESEM operates by raster scanning an electron beam across a sample and detecting the signal produced by the interaction between the beam and the specimen.

Just like optical microscopy, FESEM also makes use of lenses to focus and control the beam that composes the image, an FESEM uses lenses formed by concentrated electromagnetic fields [69].

2.4.1.3 Atomic Force Microscope (AFM)

Atomic Force Microscope (AFM) is a non-optical imaging technique with high resolution. It is equipped with a very accurate measuring instrument for surface examination. AFM permits precise, nondestructive measurements of the chemical, electrical, mechanical and topographical, etc. characteristics of a specimen surface in liquids, ultrahigh vacuum, or in air with quite high resolution. AFM equipment includes a control unit with a sharp tip, scanner, laser, and photodetector. Employing this tool the forces which is formed between the cantilever tip and the specimen surface are evaluated in the nanoscale. The forces can be Van der Waals, magnetic or electrostatic force. The movement of the surface scan is dependent on the interaction relation existing between the tip and the substance surface. After the movement on the surface, the laser beam is projected onto the photodetector in the way shown in the Fig. (2-3).

In the last step of the process, AFM images are derived from the voltage produced by the photodetector. The atomic force microscope is used in several modes of operation. Conventional techniques (contact mode, non-contact, tapping) make it possible to obtain a surface topography, to make it possible to obtain various information on the physicochemical properties of the sample [70,71].

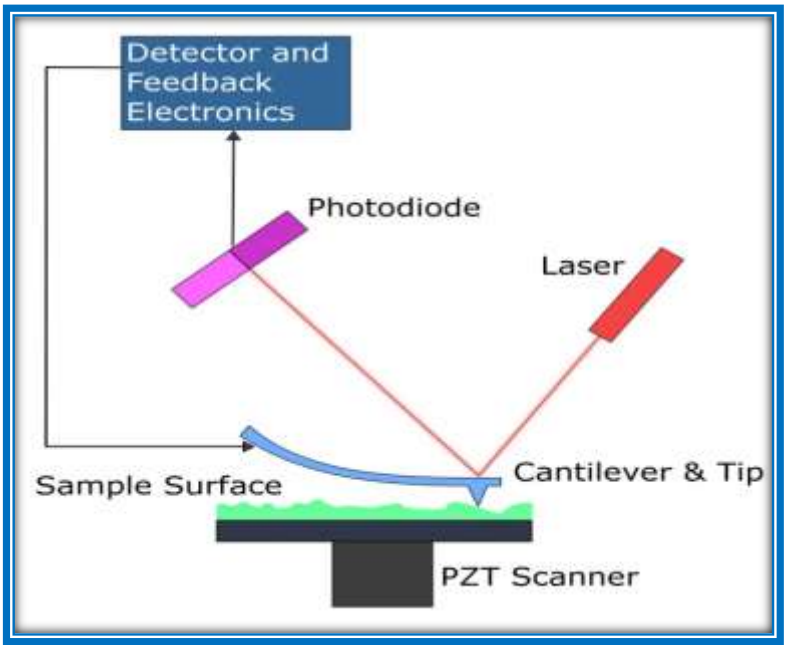

Fig. (2-3): Schematic representation of the atomic force microscope[70].

2.4.2 Optical Characteristics

The optical characteristics of a semiconductor are associated to the intrinsic effect. The generation process of electron-hole pair occurs directly or indirectly depend in on intrinsic position of the top point of valence band (V.B) and bottom of the conduction band (C.B) in the band structure.

2.4.3.1 Basic theory of UV– Vis absorption spectrophotometer

There are several molecules that are capable of absorbing ultraviolet or visible light. Fundamental absorption is the most essential absorption process, and it includes the electron transition from the valence band to the conduction band. This movement is accompanied by a sharp increase in absorption, which may be used to calculate the energy gap of the semiconductor [72].

The photons from the incident beam are absorbed by the semiconductor, and the amount of photons that are absorbed is dependent on the energy of the photons (hυ), and the frequency of the incident photons(υ). The absorption is associated with the electronic transition process between the valance band (V.B) and the conduction band (C.B) in the substance, and it begins at the fundamental absorption edge is the point that corresponds to the smallest difference in energy level between the top point of the valance band and the bottom point of the conduction band. If the photon energy is equal to or greater than the energy gap (E_g), the photon could indeed interact with a valence electron, elevating it into the conduction band and creating an electron–hole pair [73].The incident photon that generate the electron-hole pair has a maximum wavelength (λc) which can be evaluated by the following relation [74]:

$$\lambda_c\,(\text{nm}) = \frac{hc}{E_g} = \frac{1.24}{E_{g(eV)}} \qquad (2-7)$$

According to Beer's Lambert law, intensity of photon reduces exponentially with increasing thickness through the semiconductor [75].

$$I = I_o e^{-\alpha t} \qquad (2-8)$$

Where I_o and I are the intensity of the incident and the transmitted photon, respectively and α represent the absorption coefficients which is represent the fraction of the power absorbed in a unit length of the medium and given by [75]:

$$\alpha = 2.303\frac{A}{t} \qquad (2-9)$$

Where (A) is the absorbance and the thickness is denoted by (t).

2.4.3.2 The Electronic Transitions.

The electronic transitions can be classified basically into two types .

(a) Direct Transitions.

This transition happens in semiconductors when the bottom of (C.B.) is exactly over the top of (V.B.). This means that they have the same value of wave vector i.e. ($\Delta K=0$) in this state the absorption appears when ($h\upsilon=E_g^{opt.}$). This transition type required to the Law's of conservation in energy and momentum. These direct transitions have two types Direct allowed transition happens from the top points in the (V.B.) and the bottom point in the (C.B.), as shown in figure (2-4(a)).The direct forbidden transitions happens from near top points of (V.B.) and the bottom points of (C.B.) [76] as shown in figure (2-4(b)).

The absorption coefficient for this transitions type is given by [76]:

$$(\alpha h\nu) = B(h\nu - E_g)^{\gamma} \qquad (2-10)$$

Where: E_g: energy gap between direct transition

B: constant depended on type of material.

r: exponential constant, its value depended on type of transition,

γ =1/2 for the allowed direct transition.

γ =3/2 for the forbidden direct transition

(b) Indirect Transitions.

In these transitions type, the bottom of (C.B.) is not over the top of (V.B.), in curve (E-K). The electron transits from (V.B.) to (C.B.) is not perpendicularly where the value of the wave vector of electron before and after transition is not equal ($\Delta K \neq 0$). This transition type happens with helpful of particle called "Phonon", for conservation of the energy and momentum law. There are two types of indirect transitions [74] they are allowed indirect transitions happen between the top of (V.B.) and the bottom

of (C.B.) which is found in the difference region of (K-space) as in Fig. (2-4(c)).

The forbidden indirect transitions happen between near points in the top of (V.B.) and near points in the bottom of (C.B.) as shown in figure (2-4(d)). The absorption coefficient for transition with a phonon absorption is given by [77].

$$(\alpha h\nu) = B(h\nu - E_g \pm E_{ph.})^{\gamma} \qquad (2-11)$$

Where: $E_{ph.}$: energy of phonon, is (-) when phonon absorption, and (+) when phonon emission.

($\gamma = 2$) for the allowed indirect transition and ($\gamma = 3$) for the forbidden indirect transition.

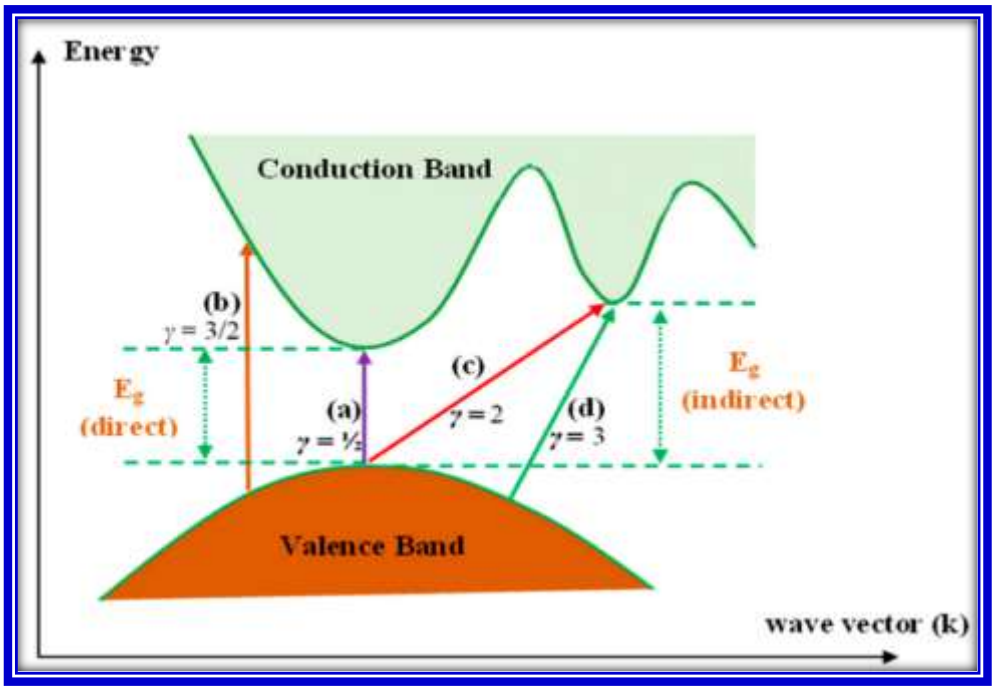

Fig. (2-4): Shows the transition types : (a) Allowed direct transition (b) forbidden direct transition (c) allowed indirect transition.(d) forbidden indirect transition [77].

2.4.3.3 Transmittance, Reflectance and Absorbance

The ratio of the intensity of the transmitted light to the intensity of incident light is known as transmittance (T) [78].

$$T = \frac{I_T}{I_\circ} \qquad (2-12)$$

The absorbance (A) is defined as the ratio of the absorbed intensity (I_A) to the incident intensity I_o [78].

$$A = \frac{I_A}{I_o} \qquad (2-13)$$

We can also find a transmittance as a function of wavelength through the exponential relationship for both absorbance and transmittance

$$A = \mathrm{Log}(\frac{1}{T}) \qquad (2-14)$$

Absorption and transmission can be acquired from relationships [79].

$$R + T + A = 1 \qquad (2-15)$$

Where R is reflectance which defined as the ratio of the incoming intensity to the reflected intensity.

2.4.3.4 Extinction Coefficient

The extinction coefficient represents the amount of attenuation of the light beam as a result of the interaction of light with the material of the thin film. It is the imaginary portion of the complex refractive index ($\tilde{n}$) [80].

$$\tilde{n} = n - ik_0 \qquad (2-16)$$

Where n is the real part of refractive index, equal to (c/v).

c is velocity of light in space and v is velocity of light in material.

The extinction coefficient (k_o) is defined by the following equation [81]:

$$k_0 = \frac{\alpha \lambda}{4 \pi} \qquad (2-17)$$

Where α: represents the absorption coefficient and λ: is the wavelength of incident rays.

2.5 Electrical Properties

The electrical characteristics of semiconductors include the current-voltage (I-V) characteristics (under illumines) the Hall effect and (C-V) characteristics.

2.5.1 Some Parameters of Solar Cell

A solar cell is essential a p-n junction with a large surface area. When light reaches the p-n junction, the light photons can easily enter in the junction, through very thin p-type layer. The light energy, in the form of photons, supplies sufficient energy to the junction to create a number of electron-hole pairs. The incident light breaks the thermal equilibrium condition of the junction. The free electrons in the depletion region can quickly cometo the n-type side of the junction. Similarly, the holes in the depletion can quickly come to the p-type side of the junction. Once, the newly created free electrons come to the n-type side, cannot further cross the junction because of barrier potential of the junction. Similarly, the newly created holes once come to the p-type side cannot further cross the junction became of same barrier potential of the junction. As the concentration of electrons becomes higher in one side, i.e. n-type side of the junction and concentration of holes becomes more in another side, i.e. the p-type side of the junction, the p-n junction will behave like a small battery cell. A voltage is set up which is known as photo voltage. If we connect a small load across the junction, there will be a tiny current flowing through it. There are several parameters that significantly affect the efficiency of a solar cell [82,83].

2.5.1.1 Short Circuit Current (I_{sc})

It is the current that is gained while the solar cell is short circuited, which is another way of saying that there is no voltage connected to the cell when it is be in measured i.e., the short circuit current matches the light-generated current [84].

$$J_{sc} = \frac{I_{sc}}{\boldsymbol{A}} \qquad (2-17)$$

Where J_{sc} is short-circuit current density, **A** is the effective area of the solar cell, and Isc denoted to short-circuit current.

2.5. 1.2 Open Circuit Voltage (V_{OC})

The voltage that is measured in an open circuit is the voltage measured when there is no current flowing through the circuit. In other words, it refers to the voltage that is produced at the terminals of the solar cell when an infinite load is connected to it. Open circuit voltage, V_{oc} (mV), can be calculated using the formula [85].

$$Voc = \frac{k_B T}{q} ln \frac{I_{gen}}{I_{sat}} + 1 \qquad (2-18)$$

Where I_{gen} is light generated current, I_{sat} is reverse saturation current, k_B is Boltzmann constant and T temperature .

2.5. 1.3 Fill Factor (F.F)

The fill factor is the parameters that describes the nonlinear electrical behavior of the solar cell Fill factor is defined as the ratio of the maximum power from the solar cell to the product of open circuit voltage and short-circuit current [86].

$$P_{max} = I_{max} V_{max} \qquad (2-19)$$

Where V_{max} and I_{max} are the maximum voltage and current that can be achieved and the corresponding power (P_{max}).

$$F.F = \frac{I_{max} V_{max}}{\text{Isc Voc}} \qquad (2-20)$$

Where (F.F) is a fill factor.

2.5. 1.4 Efficiency (η)

The ratio of the photovoltaically produced output to the incident power falling on a solar cell is known as its efficiency. It is a measurement of the amount of light energy that was effectively transformed into electrical energy. Efficiency, η (%) is given by the relation [87]:

$$\eta = \frac{P_{out}}{P_{in}} \qquad (2-21)$$

$$\eta = \frac{F.F\, V_{oc} I_{sc}}{P_{in}} \times 100\% \qquad (2-22)$$

When the total incident intensity on the cell P_{in} is (100 mW/m^2), the efficiency reduces to

$$\eta = F.F\, V_{oc} I_{sc} \qquad (2-23)$$

The (I-V) curves and the optimal point for the photovoltaic characteristics of a solar cell in both darkness and light are shown in Fig. (2-3).

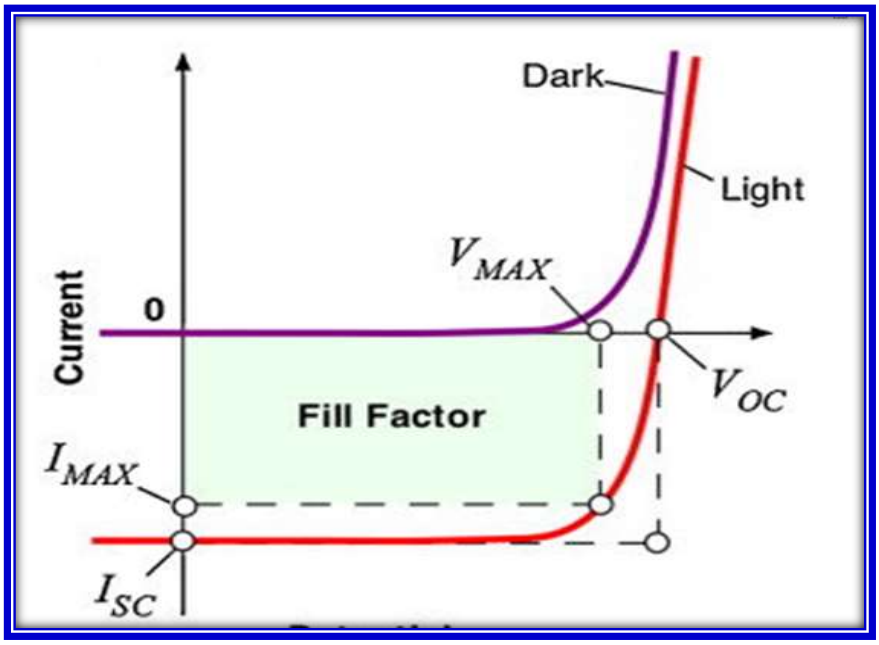

Fig. (2-5) : Dark and light I-V curves [88].

2.5.2 Hall Effect

One of the most significant effects in determining the characteristics of semiconductor materials from an electrical standpoint is the Hall effect. In common practice, the Hall effect was utilized to measure the mobility, the carrier concentration, and the type of semiconductors (**p** or **n**). It is an essential analytical tool since a simple conductance measurement can just provide the result of mobility and concentration. A mutually perpendicular electric field (E_H) is generated when a magnetic field (B) is applied at right angles to a current that flows(I), as shown in Fig. (2-4). This electric field is directly proportional to the product of the current density (J) and the magnetic induction, and it occurs when a magnetic field is applied at right angles to a current flow [89].

$$E_H = |R_H| J B \qquad (2-24)$$

Where (R_H) represent the Hall coefficient, (J=I/**a**)where (**a**) is the cross section area and B is denoted to the magnetic field.

Hall field is referred to the generated electric field (E_H) which is related to the Hall voltage (V_H) by the following relation [90].

$$V_H = E_H W \qquad (2-25)$$

Where (W) is the distance between the two electrodes.

By plotting Hall voltage as a function of current, the Hall coefficient can be calculated using the following formula [90]:

$$R_H = \frac{V_H}{I} . \frac{t}{B} \qquad (2-26)$$

Carrier's concentration **($\boldsymbol{n}$)** and **(p)** can be evaluated by using the relation [86]:

$$\boldsymbol{n} = \frac{-1}{q\, R_H} \qquad for\ electrons \qquad (2-27)$$

or

$$\boldsymbol{p} = \frac{+1}{q\, R_H} \qquad for\ holes \qquad (2-28)$$

Where (q) represent the charge of an electron.

The Hall mobility can be derived from Hall measurements using the formula [91]:

$$\mu_H = |R_H|\, \sigma_{R.\boldsymbol{T}} \qquad (2-29)$$

Where ($\sigma_{R.T}$) is the conductivity at room temperature.

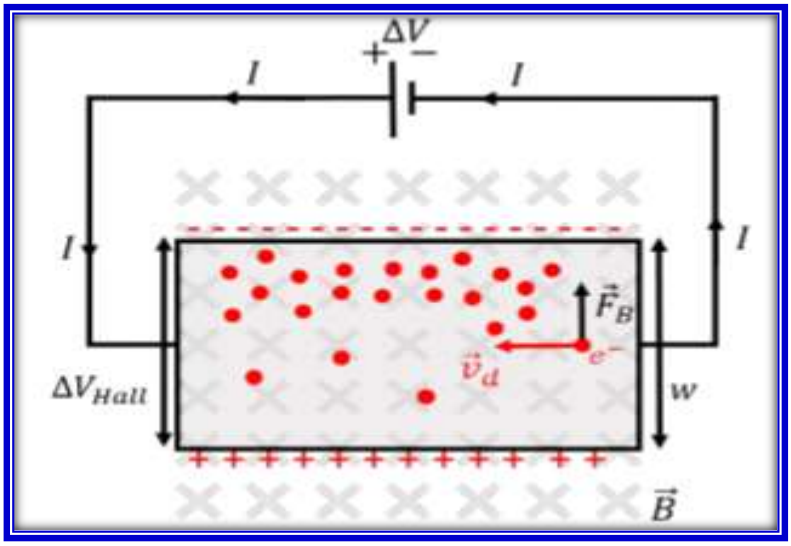

Fig. (2-6): Hall effect measurement circuit [92].

2.5.3 Resistivity (ρ)

The conductivity of semiconducting material, in addition to being dependent on electron and/or hole concentration, is also a function of the charge carriers motilities. The resistivity of any conductor (film) can be calculated from the relation [90]:

$$\boldsymbol{\rho} = \frac{R_e\, a}{L} \qquad (2-30)$$

Where (**a**) is the cross section area (film sheet) and (L) is the conductor length (inter electrode spacing). The resistivity of the films related to the electric field and the current passing through the film is [90].

$$\boldsymbol{\rho} = \frac{E}{J} \qquad (2-31)$$

Where (E) is the electric field equals to (V/d). It depends on the resistivity (or conductivity), that is on the carrier concentration (electrons or holes). It is affected by so many parameters or conditions mainly the doping, temperature and deposition technique [90].

2.5.4 Mobility (μ)

Mobility is an important parameter for carrier transport because it refers to how strongly the motion of a drift velocity electron is influenced by an applied electric field and given by [91].

$$\nu_n = -\mu_n E \qquad (2-32)$$

Where (ν_n) is the electron drift velocity.

Analogous expressions can be written for electrons in the conduction band and holes in the valence band respectively [91].

$$\nu_p = \mu_p E \qquad (2-33)$$

Where (μ_n) and (μ_p) are the electrons and holes mobility respectively and (ν_p) is the hole drift speed. The negative sign is removed in eq. (2-33) because the holes drift in the same direction as the electric field [91].

2.5.5 Capacitance – Voltage (C-V) Characteristics

Capacity-voltage (C-V) characteristics are considered so important to decide on some characteristics of the manufactured junction; for it is possible to calculate the built–in potential (V_{bi}), the depletion width layer, charge-carrier density and device type.

The junction capacitance of anisotype heterjunctions forms when two semiconductors having opposite type of conductivities bring into contact, where the charge will transfer from one to the other until the fermi levels equalize. The expression of the capacitance per unit area under reverse bias voltage can be written as [93]:

$$C = \frac{dq}{dV} = \frac{\varepsilon_s A_j}{W} \qquad (2-34)$$

Where, *(V)* is the applied voltage, and (ε_s) is semiconductor permittivity calculated from the equation:

$$\varepsilon_s = (\varepsilon_1 \varepsilon_2)/(\varepsilon_1 + \varepsilon_2) \qquad (2-35)$$

Where (ε_1) and (ε_2) are the semiconductor permittivity for the two semiconductor materials. The cross point ($1/C^2=0$) of the ($1/C^2$-V) curve represents the built-in potential of the heterojunction, and the slope of this line gives the charge-carrier density of the substrate. The linear variation of the experimental curve (C^{-2}) versus (V) is indicative of the presence of the abrupt heterojunction. [94,95].

Chapter Three

Experimental Work

3.1 Introduction

This section contains a description of all the equipment and instruments used in the experimental part of this study. It starts with the vacuum evaporation process for depositing Cu_2O, SnS, SnS/Cu_2O, and SnS:Cu_2O thin film onto glass and Silicon substrates. The structural, optical, and electrical measurements will be measured or calculated. The techniques used for manufacturing and analyzing the structure of thin films involve the investigation of their structural characteristics by X-ray diffraction (XRD) and morphological: using field emission scanning electron microscope (FESEM) and atomic force microscope (AFM) as well as the optical measurements of thin films such as absorbance (A), transmittance (T), and optical energy gap (E_g). To fabricated solar cell pure aluminum was deposited onto the Cu_2O/Si, SnS/Si, SnS/Cu_2O/Si and SnS:Cu_2O/Si films allowing for the production of the front and back contacts of the solar cell. Some important parameters of the solar cell will be evaluated, these include open circuit voltage (V_{oc}), short circuit current (I_{sc}), fill factor (F.F), and efficiency (η).

3.2 Material and Preparation of Substrates

Tin Sulfide (SnS) was observed as a powder from Zhengzhou dongyao nano materials Co. LTD/ China company with nano grain size 50 nm and cuprous oxide with density 6.140 g/ cm^3, color black, and high purity (99.99%). The structure and characteristics of thin films are significantly influenced by the substrates. Glass slides are the type of substrate that was used for this work (microscope glass)/Citotes manufacturing labware Co. LTD/ China company with dimensions (2.5×7.62) cm^2. The glass substrate Fwas cleaned using an ultrasonic bath solution of diluted sulfuric acid (H_2SO_4:H_2O;1:5, v/v), acetone, and distilled water for 15 minutes.

The Si-wafer was n-type cut with a special diamond cutter into small samples with appropriate sizes of about (0.75 × 0.75) cm^2. Silicon wafers were washed ultrasonically in distilled water and were immersed in ethanol in order to remove dirt and oil, while Native oxides are removed by using 1:10 HF: H_2O solution. The properties chemical materials used in this work are listed in Table (3-1). Cu_2O thin film was deposited by used 0.01 g of cuprous oxide powder and 0.01 g of tin sulfide powder for SnS thin film. SnS thin layer was coated then another thin layer of Cu_2O in order to fabricate SnS/Cu_2O thin film. Thin film of SnS:Cu_2O was prepared by mixing an equal ratio (1:1) on glass substrate with 0.01 g for each compound. At the same way these thin films are deposited onto silicon in order to fabricate Cu_2O/Si, SnS/Si, Cu_2O/ SnS/ Si and Cu_2O :SnS /Si solar cells.

Table (3-1): The properties of materials used.

Properties	**Tin Sulfide**	**Cuprous Oxide**
Chemical formula	SnS	Cu_2O
Purity	99.99 %	99.99 %
Molar mass	150.775 g/mol	143.09 g/mol
Appearance	dark brown	black
Density	5.22 g/cm^3	6.140 g/cm^3
Melting point	882 °C	1230 °C
Boiling point	1230 °C	1800 °C

The schematic diagram that demonstrates the experimental work, displayed in Fig. (3-1).

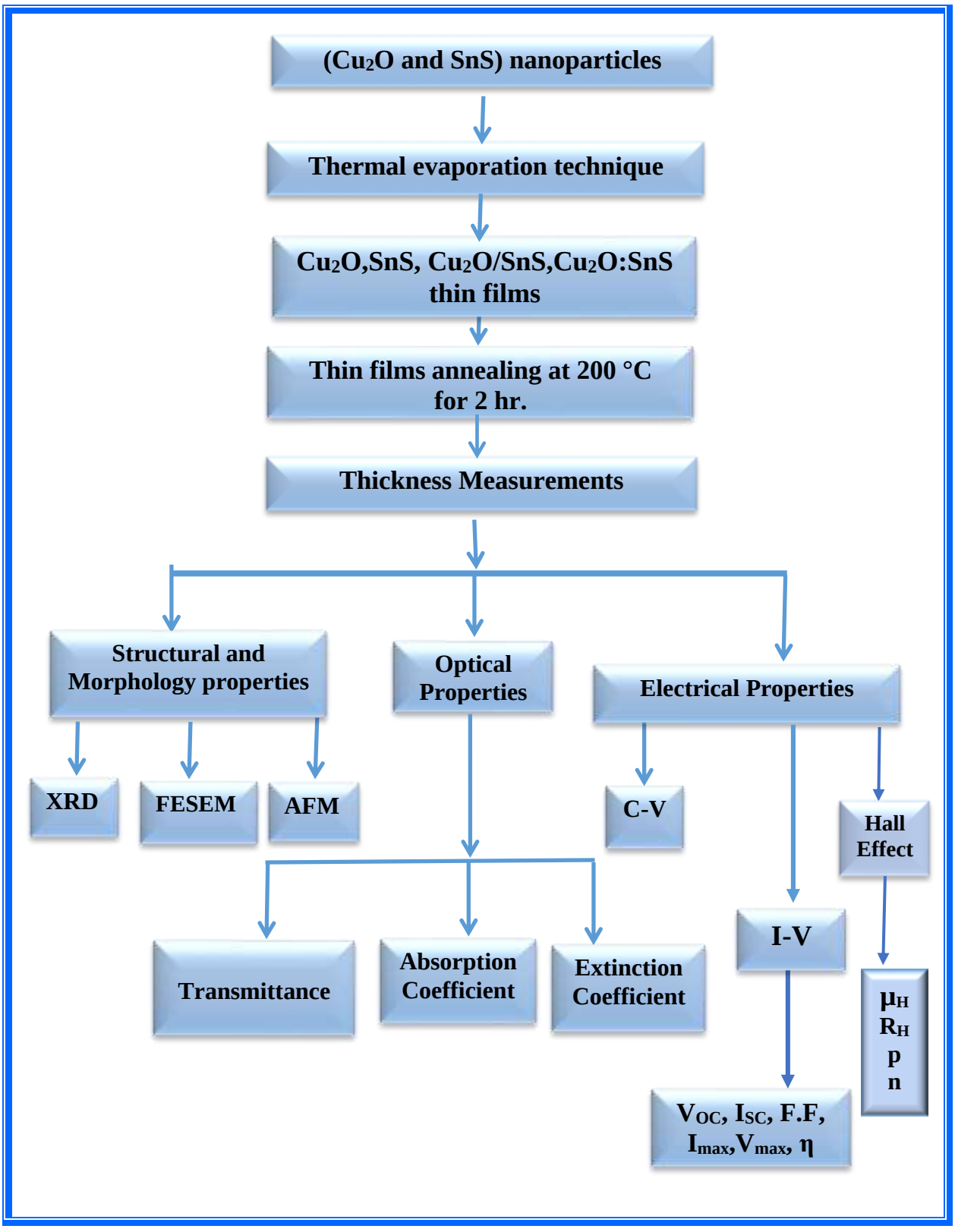

Fig. (3-1): Main steps of the experimental work.

3.3 The Coating Unit

In this work, the Edwards-c(306) model of vacuum unit system has been employed to carry out the deposition of thin films. The main construction of this unit is displayed in Fig. (3-2). high purity materials (99.99%) was placed in a boat of molybdenum in order to prepare Cu_2O, SnS, Cu_2O/ SnS and Cu_2O:SnS thin films by thermal evaporation. In this method, a solid material of cuprous and tin sulfide were heated to its point of evaporation inside a high-vacuum chamber. The substrates are held inverted at the highest point of the chamber, and the material is placed at the bottom, quite on the inside of the boat. After the molecules have evaporated, they make their way from the boat to the substrate, where they nucleate to create a thin coating.

A gradual electric current was applied to the boat in order to prevent it from breaking, while the system was pumped down to a vacuum of 10^{-7} mbar. The deposition process begins at a constant rate of 0.3 nm/s when the boat's temperature reaches the requisite temperature and then fill the chamber with air, and the films were removed from the coating unit and stored until the measurements were performed.

All the samples are made under constant conditions (deposition rate, substrate temperature, and pressure). The evaporation operations in this study were performed at room temperature, with a 15 cm separation distance between the source and substrate. This system is found at the Department of Physics /College of Education for Pure Sciences/ University of Babylon.

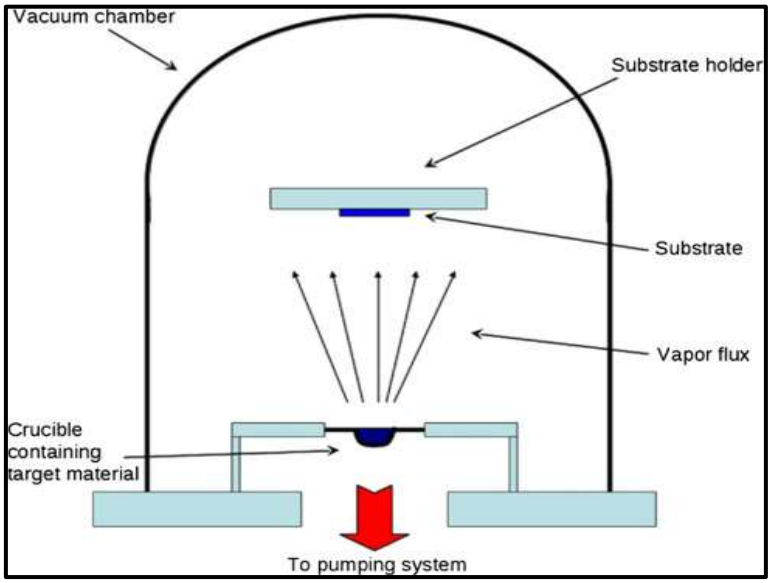

Fig. (3-2): Thermal evaporation system.

3.4 Evaporation Boat

Metals having a high melting point, such as molybdenum ((Mo) (M.P. = 2622 °C)) and tungsten ((W) (M.P. = 3370 °C)), are the most widely used materials for evaporation boats. In this study, two categories of sources were employed for evaporation. For the evaporation of aluminum to make electrodes, a spiral boat source of tungsten material was used, and a molybdenum boat was employed in the deposition of thin films as illustrated in Fig. (3-3).

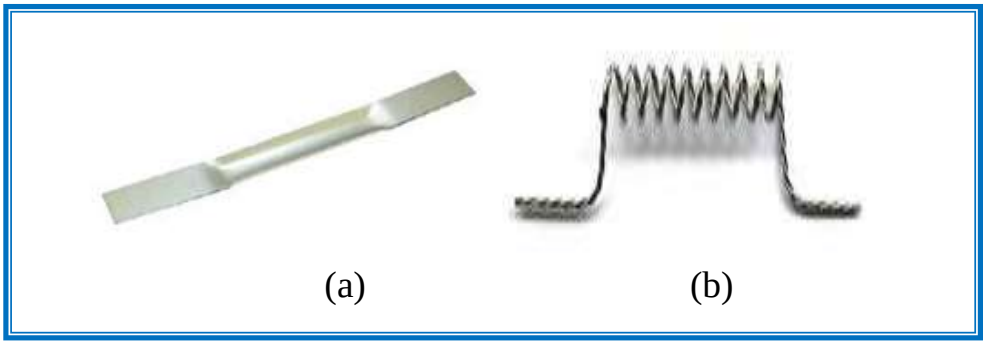

Fig. (3-3): Boat of evaporation. (a) Molybdenum boat, (b) Tungsten spiral boat.

3.5 Annealing

The annealing process of thin films was accomplished by the electrical furnace (CARBOLITE (CWF 1200). The temperature of the oven is controlled by heat scale of the Furnace. The samples are placed in the furnace crucible which contain test samples inside the tube of the electrical furnace to be annealed. The annealing process was carried out at 200 ºC for 2h. This system is found at Department of Ecology and Pollution /Faculty of Science/ University of Kufa.

3.6 Masking Techniques

Typically, the mask is designed from metal (Al foil). These masks are positioned as near as conceivable to the substrate onto which the film will be deposited. For electrical measurements, the shape of the film must be specified, and to achieve the desired shape, a suitable mask is used for this purpose. There are different shapes of masks, as presented in Fig. (3-4). Ohmic front contacts were fabricated by used different mask dependent on application.

3.6.1 Hall Mask

Fabricate Ohmic contacts by evaporating (99.9%) purity aluminum wires for front contact as Hall mask on Cu_2O, SnS, SnS/Cu_2O and SnS:Cu_2O thin film deposited on glass substrate as show in Fig.(3-4(a)).

3.6.2 Solar Cell Mask

Ohmic contacts were fabricated by evaporating (99.9%) purity aluminum wires for the front contact solar cell mask using Edwards coating

system. The solar cell mask of sample displayed in Fig.(3-4). In addition, a spiral boat of tungsten is used as source to evaporate pure aluminum wire for the production of the front and back contacts of the solar cell.

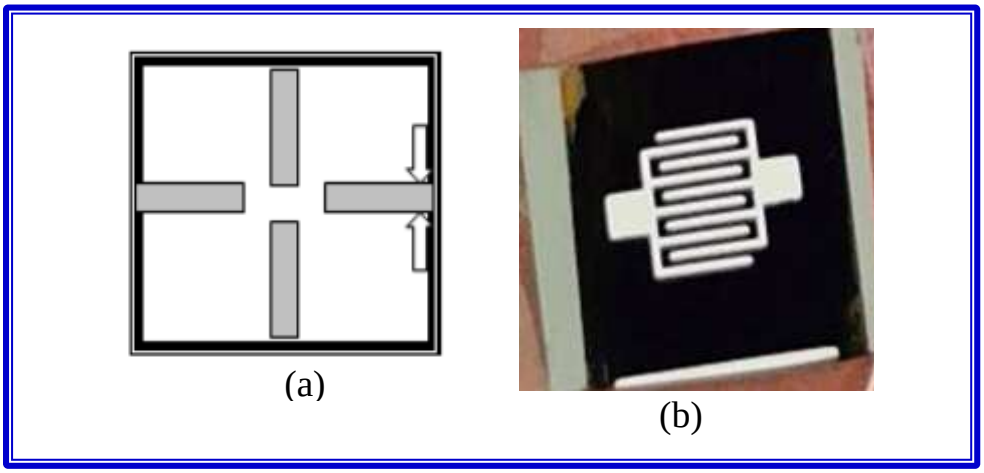

Fig. (3-4): The masks used for (a) Hall effect and (b) Solar cell device.

3.7 Thickness Measurement

One of the most significant thin film parameters is thickness since it greatly influences the characteristics of the film. Monitoring the rate of deposition during the coating process is typically used to determine the thickness of the films. Two methods have been recognized for measuring the thickness of thin films: first, the weighted method, which involves estimating the quantity of material that must be evaporated to achieve the desired film thickness, and second, the optical method. In most cases, vacuum-deposited films employed for structural, electrical, optical, or other reasons must be deposited to a specified thickness. In this study, the weighting method was employed. Using the following equation, this method finds out the necessary quantity of evaporated material used to achieve the desired thickness [96]:

$$t = \boldsymbol{m}/2\rho\pi L^2 \qquad (3-1)$$

Where: t is the film thickness in (nm).

m is the mass of the materials to be evaporated in (g).

ρ is the density of materials to be evaporated.

L is the distance between the substrate and the boat (cm).

This method provides a reliable estimation of the thickness of the deposited films and with this method.

3.8 Structural and Surface Morphological Properties

The structural characteristics of films were inspected using X-ray diffraction (XRD). In this investigation, the FESEM and AFM were employed to inspect the surface structure of thin films.

3.8.1 X–ray Diffractometer

The structural description of formed thin films can be done by analyzing the patterns of X-ray diffraction obtained by (XRD- 6000 Shimadzu). The source of X-ray radiation is Cu kα radiation the scanning angle varied in the range (10^o - 80^o) with wavelength (1.5406 Å), speed 5 deg/min, current (30 mA), and voltage (40 KV). X-ray measurement carried out at nanotechnology and advanced material research unit/ University of Kufa. The diagram of (XRD) shown in Fig. (3-5).

Fig.(3-5): Setup of X-ray diffractometer for XRD analysis [97].

3.8.2 Field Emission Scanning Electron Microscope (FESEM)

Field emission scanning electron microscope with energy-dispersive X-ray spectroscope (FESEM/EDX) that employed in this study are illustrated in Fig (3-6). The FESEM instrument is made by (ARYA Electron Optic) company. Samples were examined at Kashan University/ Islamic Republic Iran.

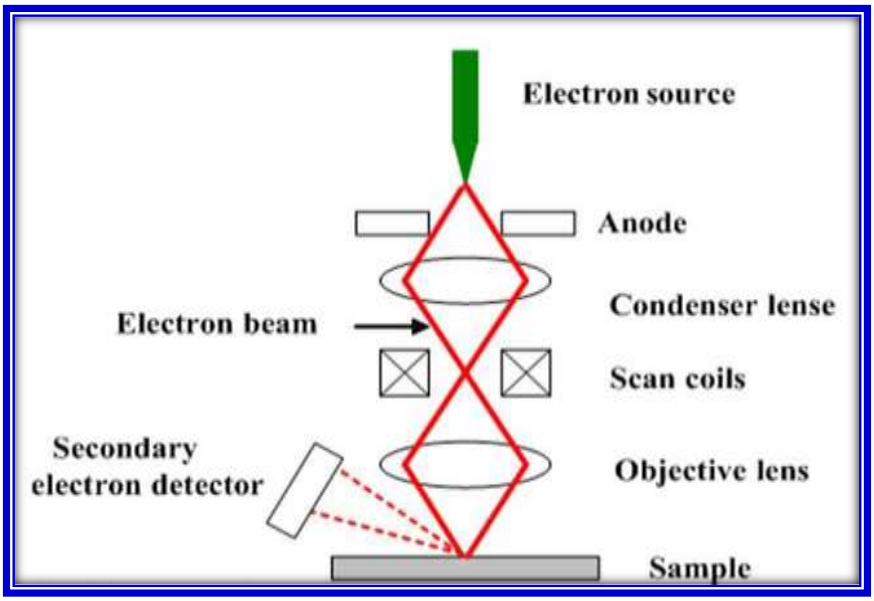

Fig. (3-6): Field emission scanning electron microscope diagram [98].

3.8.3 Atomic Force Microscope (AFM)

Atomic Force Microscope micrographs are obtained with digital instruments (Aa3000 SPM) to examine the surface texture and topography of deposited thin films. AFM height images have yielded typical data, including root mean square (RMS), roughness and average diameter. These measurements were carried out in the laboratories of Department of Physics/ College of Education for Pure Sciences /University of Babylon.

3.9 Optical Measurements

The absorption of Cu_2O, SnS, Cu_2O/SnS, and Cu_2O: SnS thin films in the (300-1100) nm wavelength range was tested by a double-beam (UV-1650 PC UV- VIS Shimadzu) spectrophotometer. As illustrated in Fig. (3-7) the data of transmittance and absorbance can be employed to compute the films' absorption coefficients at various wavelengths, which can be used to calculate the energy gap (E_g). This examination was achieved at Department of Physics/ Faculty of Science/ University of Kufa.

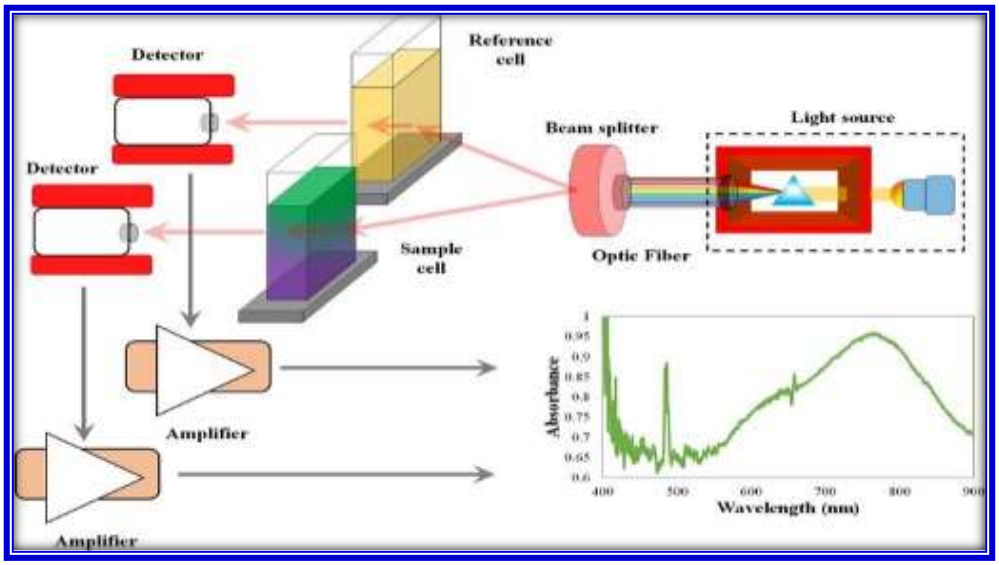

Fig. (3-7): Chart for UV spectrophotometer [99].

3.10 Electrical Measurements

Electrical measurements on manufactured thin films, which include Hall effect and I-V characteristics, were performed.

3.10.1 Measurements of the Hall Effect

Hall measurement is commonly utilized in semiconductor initial characterization. Identifying whether a substance is n-type or p-type is crucial. It permits the charge carrier density, carrier mobility, and Hall coefficient (R_H) to be measured, as illustrated in Fig. (3-8). This test is carried out in the Polymer laboratory in Department of Physics/ College of the Science/ University of Babylon.

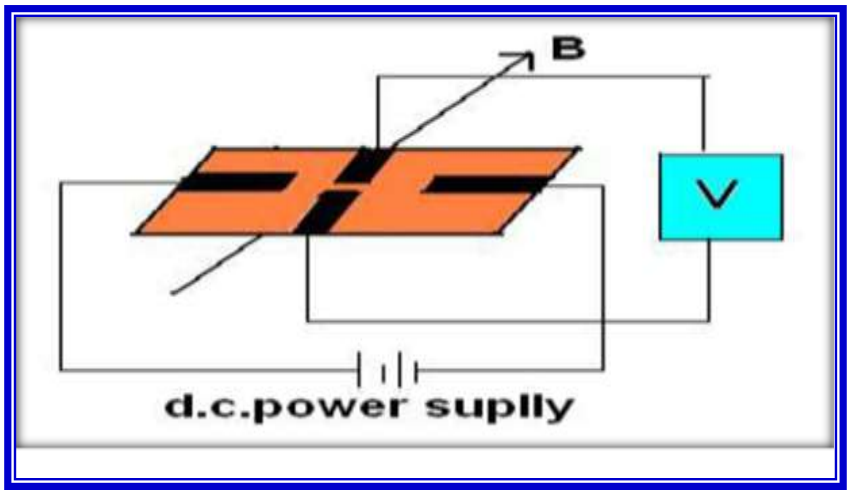

Fig. (3-8): Diagram for Hall effect [100].

3.10.2 Capacitance –Voltage Measurements

Capacitance measurements as a function of reverse voltage (C-V) for Al/Cu_2O/n-Si/Al, Al/SnS/n-Si/Al , Al/Cu_2O/SnS/n-Si/Al and the thin film with mixing ratio Al/Cu_2O: SnS/n-Si/Al heterojunction were carried out using LCR meter at a frequency of (5 kHz) as shown in Fig. (3-9).

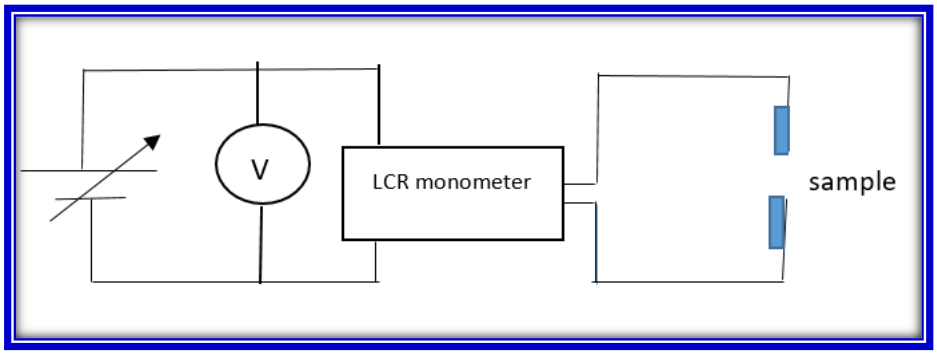

Fig. (3-9): Equivalent circuit of (C-V) measurements.

3.10.3 Current-Voltage Measurements for the Heterojunction under Illumination

The study of electrical and photovoltaic properties of solar cells has been done by using electrical circuit, as in Fig.(3-10), which consists of Micrometer type (Keithley 177 Micrometer Dmm.), Voltmeter made in china type (DT890G) and Halogen light with power ($100\,W$) gives radiation intensity from shunt voltage, since power density, which is given by each volt measured by using power meter.

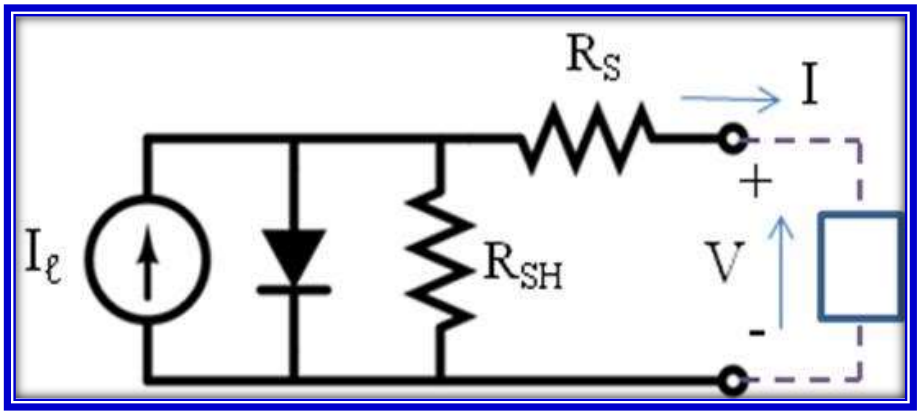

Fig. (3-10): Equivalent circuit of a solar cell [101].

Chapter Four

Results and Discussion

4.1 Introduction

This chapter present the results and discussion of the structural, morphological, optical, and electrical properties of Cu_2O, SnS, Cu_2O/SnS and Cu_2O:SnS thin films that are prepared by thermal evaporation onto glass substrates, and annealed at 200 °C for 2 h. Some essential parameters of Cu_2O/Si, SnS/Si, Cu_2O/SnS/Si and Cu_2O:SnS/Si solar cells have been investigated such as open circuit voltage, short circuit current, and efficiency.

4.2 Structural and Morphological Properties of Samples

The structural properties of all the samples studied using the techniques of X-ray diffraction (XRD), field emission scanning electron microscope (FESEM), Energy Dispersive X-Ray Spectroscope (EDX) and Atomic Force Microscope (AFM).

4.2.1 Structural Analysis

X-ray diffraction analysis was used to determine the crystallite structure of Cu_2O, SnS, Cu_2O/SnS and Cu_2O:SnS thin films deposited on glass substrates and annealed at 200 °C as well as their nature of growth.

The X-ray diffraction pattern of Cu_2O thin film deposited on glass substrate and annealed is shown in Fig.(4-1(a) and (b)). From Fig.(4-1(a)) it was observed that the main peaks appeared with the preferred orientation was (110) at $2\Theta = 29.634°$ in addition to $2\Theta = 62.738°$ and 70.214°, which belong to (220) and (310) planes, respectively. The existence of conspicuous diffraction peaks indicates that the films are polycrystalline in nature. The obtained diffraction patterns are consistent with the conventional crystallographic data for the Cu_2O JCPDS card (JCPDS Card No. 01-075-1531) which demonstrates that the Cu_2O thin film does indeed have cubic phase.

Fig.(4-1(b)) shows the X-ray diffraction pattern of Cu_2O thin film deposited on glass substrate and annealed at 200 ºC for 2h. Three prominent peaks were observed and belong to the (110), (111), and (211) planes at 2Θ = 29.238°, 36.974° and 52.871° respectively, in addition to peaks having less intense were (220) and (221) at 2Θ = 62.648 º and 65.559 º. These values are matched with the cards (JCPDS Card No.01-075-1531) for Cu_2O with simple differences. The average crystallite size of a is evaluated by the full width at half maximum (FWHM) of diffraction peaks.

The average crystallite size for the preferred orientation was calculated using equation (2-2) where it increased from 12 nm to 16 nm as recorded in Table (4-1) and the annealing process caused a sharper and so more intense peak of preferential orientation as seen in the Fig. (4-1 (b)). This might be owing to the enhancement of the crystallinity Cu_2O film structure by the annealing process and decrease its crystallite imperfections by offering the atoms enough energy to rearrange themselves in the lattice, thereby minimizing the random distribution of atoms inside the substance of the thin film [102].

X-ray patterns of the SnS thin film that was synthesized on glass substrate are seen in Fig. (4-2(a)). The main sharp peaks (003) and (102), planes at 2Θ = 22.306° and 27.55°was observed as well as peaks with less intensity at 2Θ = 59.06° and 63.843° that belong to (025) and (008) respectively. These values are compared with the cards (JCPDS Card No. 01-079-2193) and (JCPDS Card No. 00-001-0984) for SnS, and they are well matched with simple difference. From the Fig.(4-2-(b)) there is a shifting in the direction of the prominent peaks, which may be caused by the release of intrinsic strain during annealing process [103].

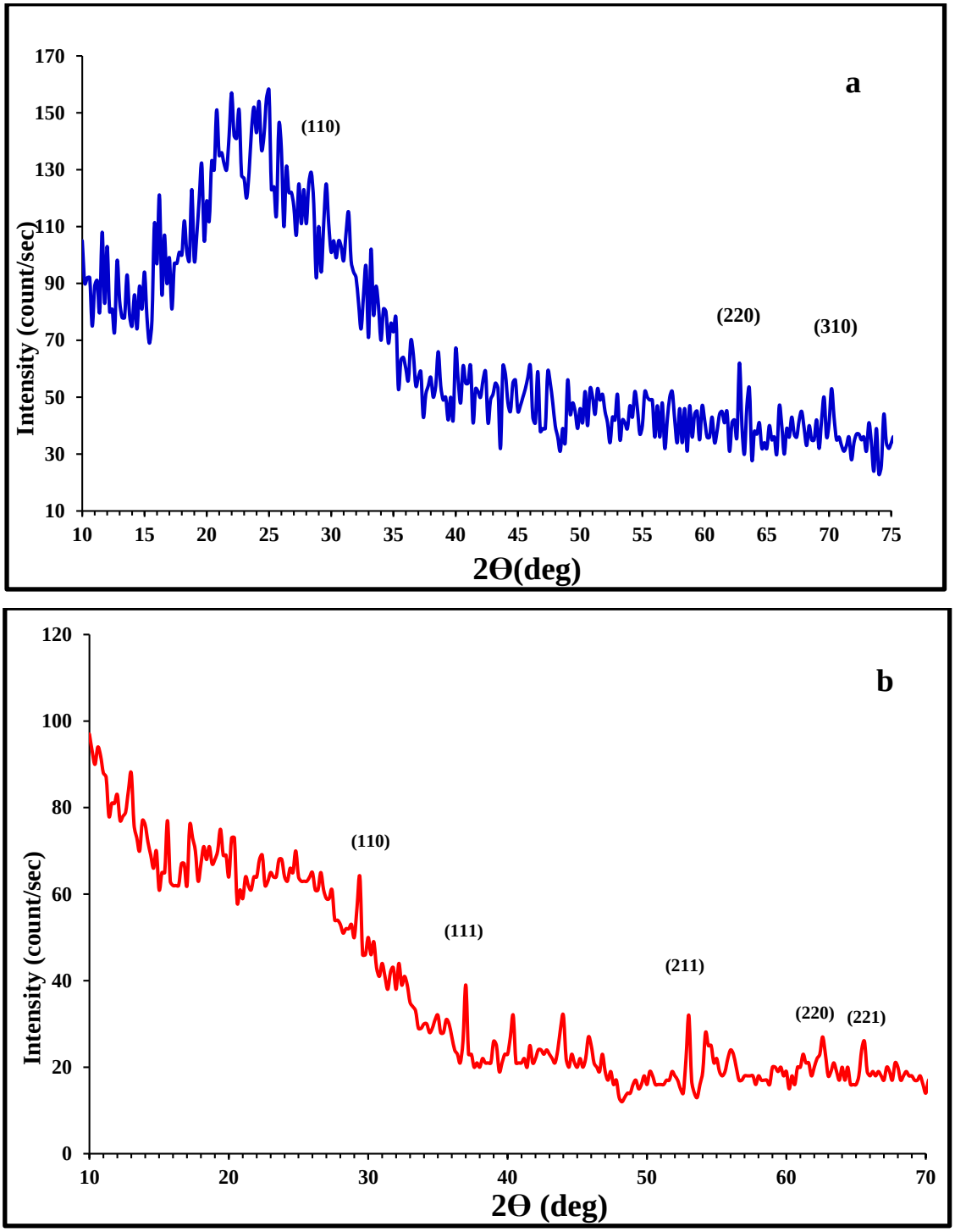

Fig. (4-1): X-ray pattern of Cu_2O thin film :(a) as deposited and (b) annealed at 200 °C.

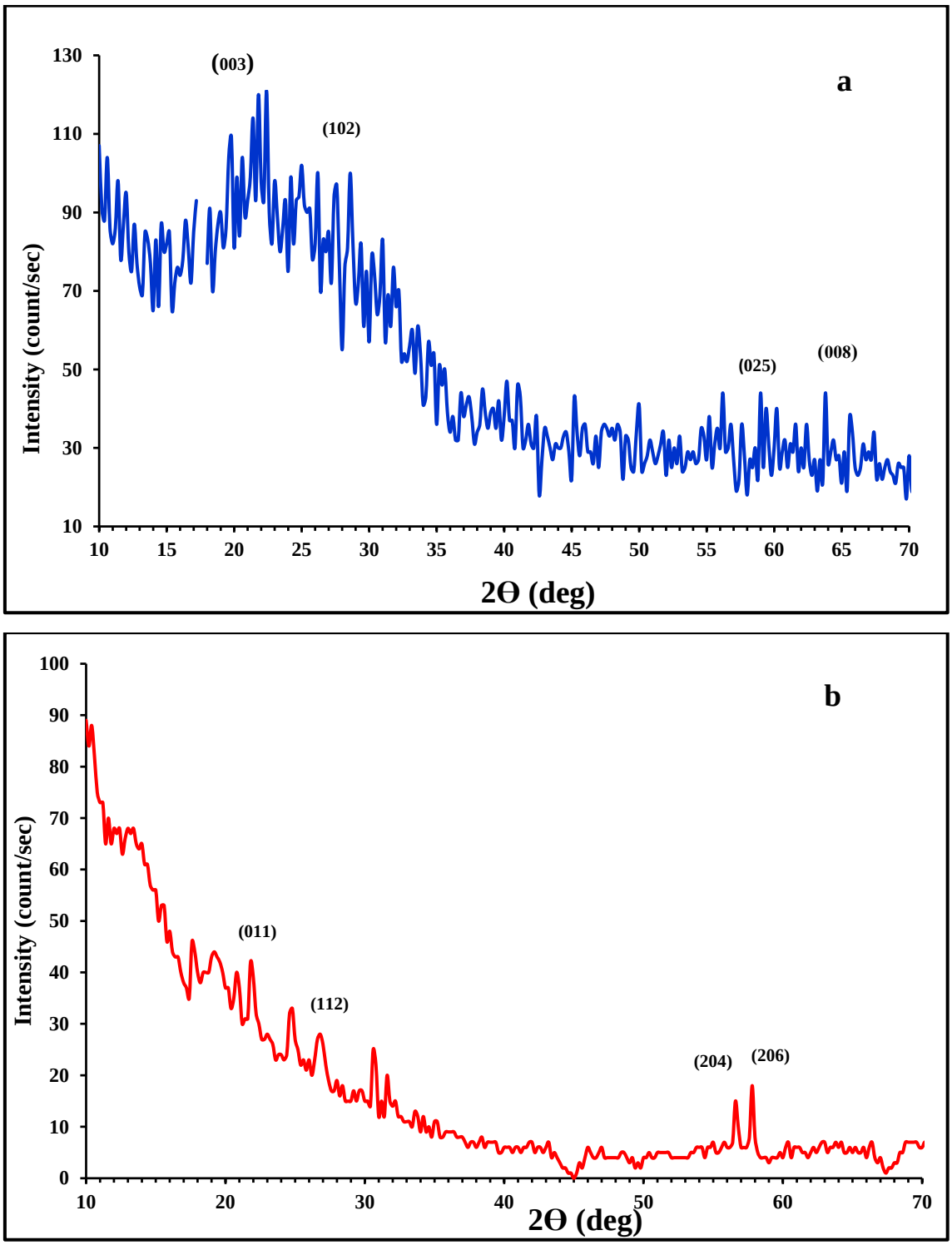

Fig. (4-2): X-ray pattern of SnS thin film: (a) as deposited and (b) annealed at 200 °C.

The average crystallite size where it is reduced from (14 to 11) nm and that decrement in average grain size after the annealing process might be attributable to the fracturing of clusters of crystallites as revealed by (Devika) *et al.* [104] as can be noticed in Table (4-1).

Table (4-1): Obtained X-ray results of Cu_2O and SnS samples as growth and as annealed.

Samples	2Θ (deg)	FWHM	(hkl)	Average Crystallite Size (nm)	$\delta=1/D^2$ lines/m^2	Average micro-strain
Deposited Cu_2O thin film	29.634	0.585	(110)			
	62.738	0.516	(220)			
	70.214	0.754	(310)			
Annealed Cu_2O thin film	29.238	0.383	(110)	16	0.003906	0.126596
	36.974	0.397	(111)			
	52.871	0.559	(211)			
	62.648	0.652	(220)			
	65.559	0.641	(221)			
Deposited SnS thin film	22.306	0.567	(003)	14	0.005102	0.144307
	27.551	0.567	(102)			
	59.06	0.603	(025)			
	63.843	0.473	(008)			
Annealed SnS thin film	21.927	0.403	(011)	11	0.008264	0.148300
	26.811	0.986	(112)			
	56.645	0.737	(204)			
	57.764	0.329	(206)			

X-ray diffraction (XRD) patterns of a fabricated and post- annealed Cu_2O/SnS films are illustrated in Fig. (4-3). Cu_2O/SnS thin films have distinctive peaks that match up well with recognized crystallite data (JCPDS Card No. 01-079-2193). All the observed samples have polycrystalline lite line in nature with orthorhombic phase. However, the most of crystallites were oriented in another different directions after annealing process as presented in Fig. (4-3b).

Fig.(4-4) displays X-ray diffraction pattern of Cu_2O:SnS film as deposited on a glass substrate. One peak can be noticed refer to (020) plane at angles of $2\Theta = 31.172^{o}$ as a preferred orientation as compared to values of card (JCPDS Card No. 01-079-2193).

After annealing process, it can be seen three main peaks at angles of $2\Theta = 19.636^{o}$, 31.677^{o}, and 35.639°. The average crystallite size decreased from 16 nm to 12 nm. The lowering in the peak intensity of Cu_2O :SnS exhibits similar behavior to that obtained by (Devika *et al.*) [104].

From Table (4-2) average crystallite size of Cu_2O/SnS and Cu_2O: SnS films are decreased after annealing process at 200 °C. The average crystallite size have been decreased might attributed to the quantum confinement [105].

From Table (4-2) it can be seen in that the values of dislocation density and micro-strain of the samples were increased after annealed at 200 ºC, and this might be due to the reduction in crystallite size, which then increases the grain boundary of the lattice [106].

Table (4-2): Obtained X-ray results of Cu_2O/SnS and Cu_2O: SnS samples as growth and as annealed.

Samples	2Ɵ (deg)	FWHM	(hkl)	Average Crystallite Size (nm)	$\delta=1/D^2$ lines/m^2	Average micro-strain
Deposited Cu_2O /SnS thin film	30.932	0.666	(020)	14	0.005102	0.113998
	47.09	0.383	(222)			
	50.164	0.437	(025)			
	53.756	0.526	(312)			
Annealed Cu_2O /SnS thin film	16.62	0.542	(002)	12	0.006944	0.202020
	23.711	1.203	(111)			
Deposited Cu_2O: SnS thin film	31.172	0.516	(020)	16	0.003906	0.124256
Annealed Cu_2O: SnS thin film	31.677	0.86	(013)	12	0.006944	0.190389
	35.639	0.754	(202)			

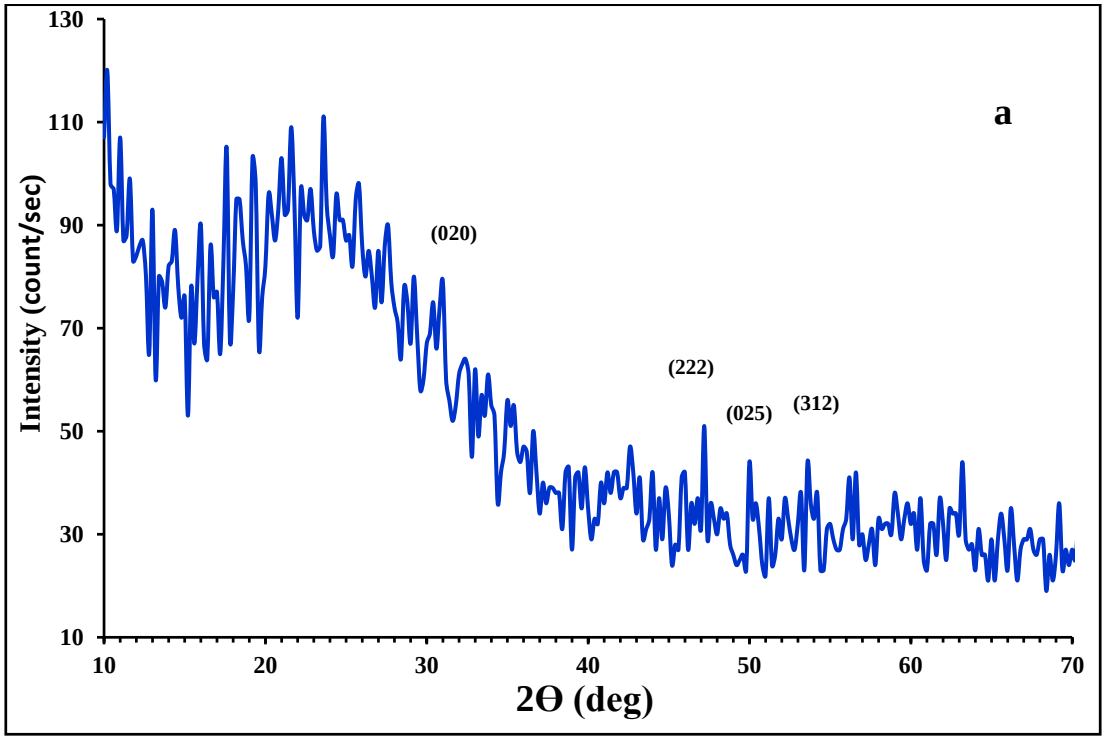

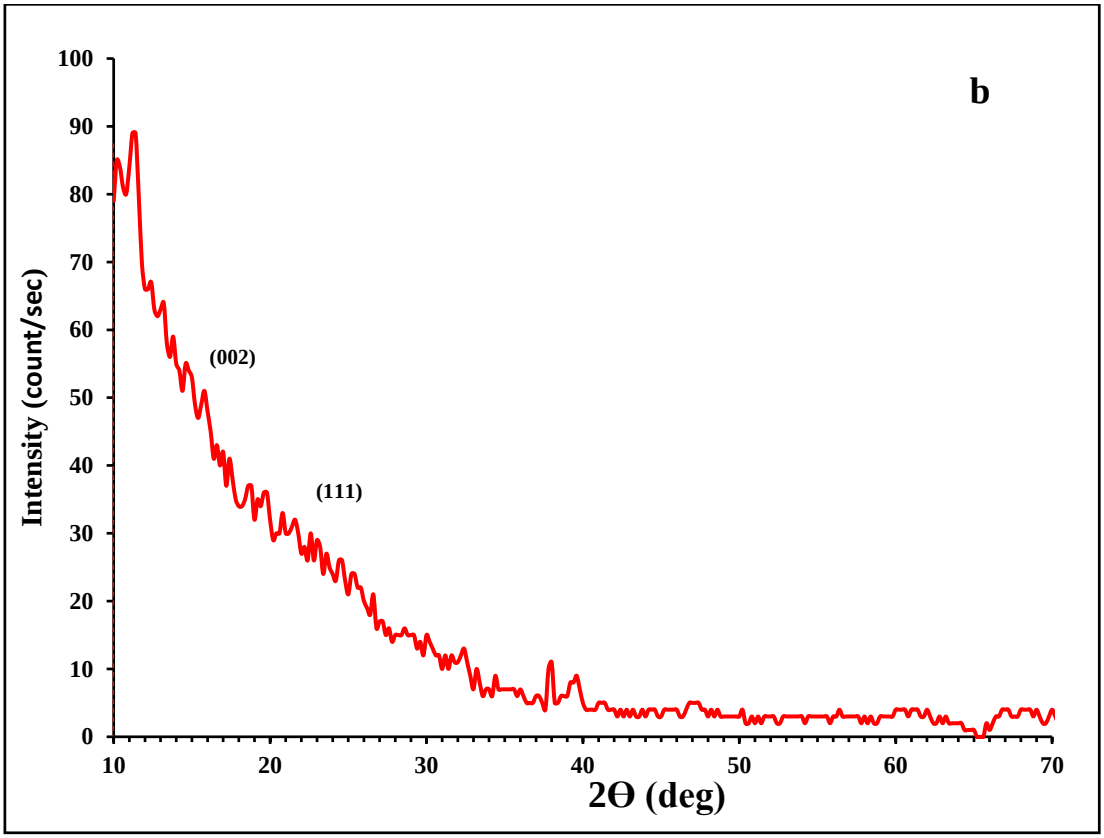

Fig. (4-3): X-ray diffraction pattern of Cu_2O/ SnS thin film: (a) as deposited and (b) annealed at 200 °C.

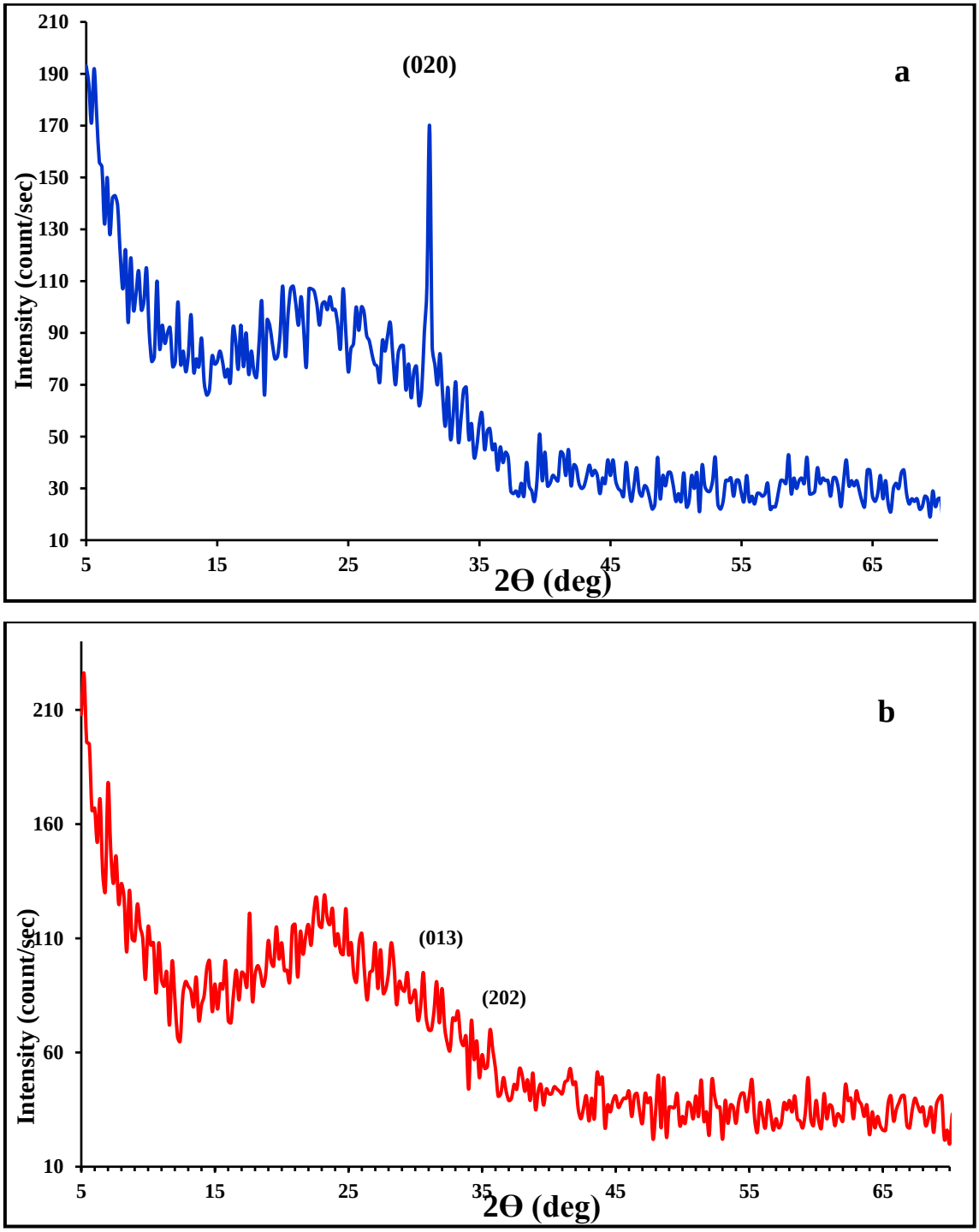

Fig. (4-4): X-ray pattern of Cu_2O: SnS thin film: (a) as deposited and (b) annealed at 200 °C.

4.2.2 Surface Morphological Analysis

The surface morphology of the films is investigated by field emission scanning electron microscope (FESEM) measurements and EDX analysis. These techniques provide vital information about surface topography, the growth process, shape and size of the grain's stoichiometry, and elements analysis of materials.

Fig. (4-5(a)) shows FESEM images of Cu_2O film as deposited. From the figure, it can see that the circular assemblies of grains including large and small particles, with irregular distribution onto the surface of the film, whereas the particles seem elongated on the surface with an average size of approximately 25.15 nm. Fig.(4-5(b)) illustrated FESEM images of Cu_2O film after annealed at 200 ^oC for 2h. FESEM images reveal a homogenous and uniform surface with no discernible micro-cracks, and the morphology of the produced films suggests that the particle size increased after annealing process with average grain size around 35.36 nm and this behaviors have good agreement with that obtained by (XRD) measurements.

From FESEM images of SnS thin films, the cross-section and surface morphology have been analyzed, as illustrated in Fig.(4–6(a)).

The images of deposited SnS films show randomly shaped grains with the presence of grain boundaries and an average grain size of about (30.02) nm. The Fig. (4-6(b)) demonstrate that SnS film became more uniform and homogeneous, without pinholes or micro-cracks, and that the particles seemed smaller and had a spherical shape after the annealing process. This reduction in size corresponds with that obtained by XRD investigation.

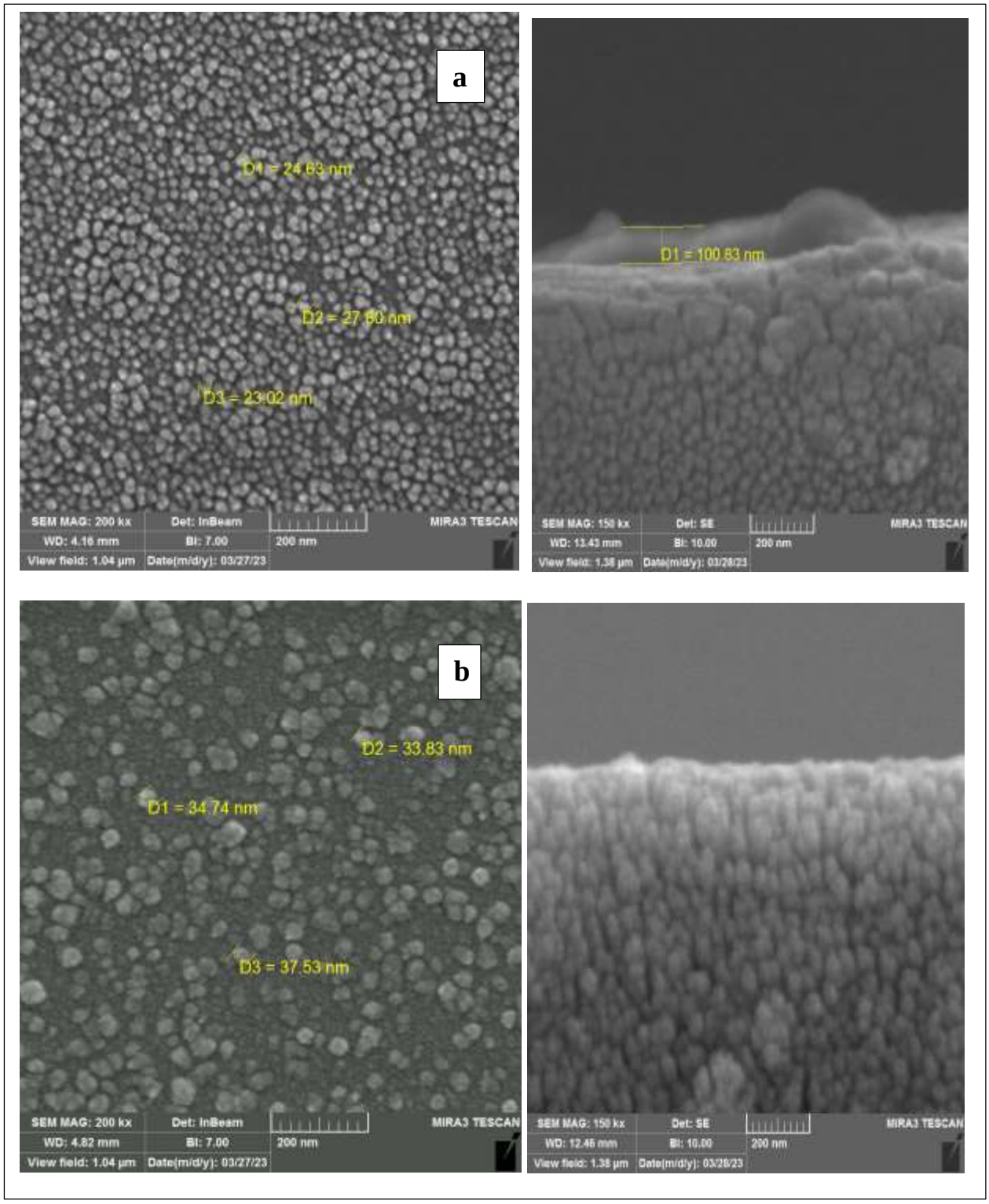

Fig.(4-5): FESEM images and cross-section of Cu_2O thin films: (a) as deposited and (b) annealed at 200 ºC.

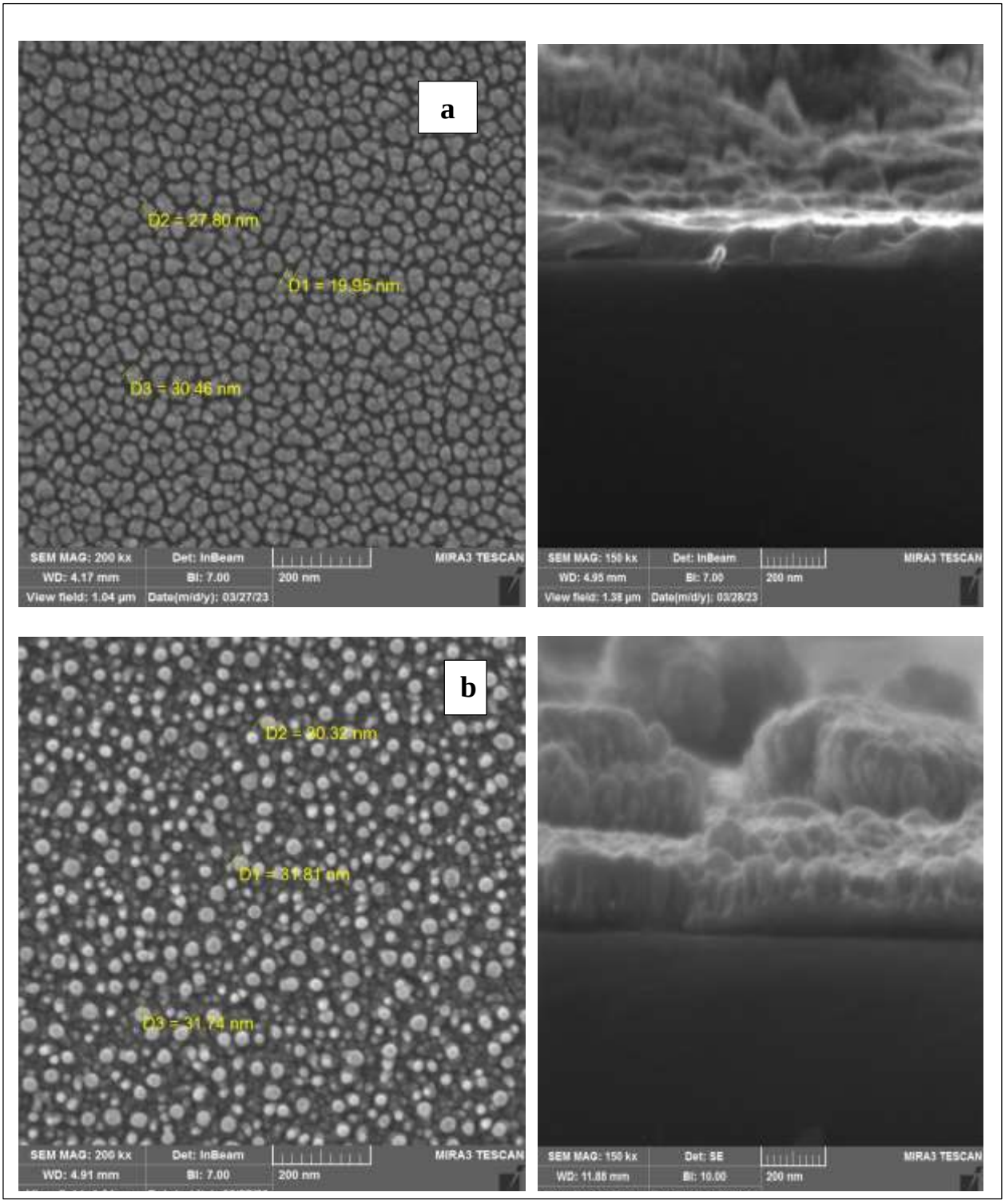

Fig. (4-6): FESEM images and cross-section of SnS thin film: (a) as deposited and (b) annealed at 200 °C.

The surface morphology and cross-section of Cu_2O/SnS thin films can be seen in Fig. (4-7(a)). For deposited Cu_2O/SnS thin film, the FESEM images display small and large grains with an irregular shape that seems stone- like shaped; however, following the annealing process, the FESEM images depict a homogenous and smooth distribution of the grains in the surface of the film with no detectable micro-cracks and pinholes, as shown in Fig.(4-7 (b)).

From the Fig., it can be noticed that the grain size is decreased after annealing process and this consequence corresponds to that obtained from XRD analysis as tabulated in Table (4-2).

Fig. (4-8) FESEM images of Cu_2O:SnS film, illustrate that grains are densely packed in tube-like shapes vertically on the thin film surface, with some large grains. There were no visible defects or pores after the annealing process, where the grain size was about 25.37 nm compared with that of the fabricated sample, which was 73.54 nm, and this reduction corresponded with that obtained by XRD investigation.

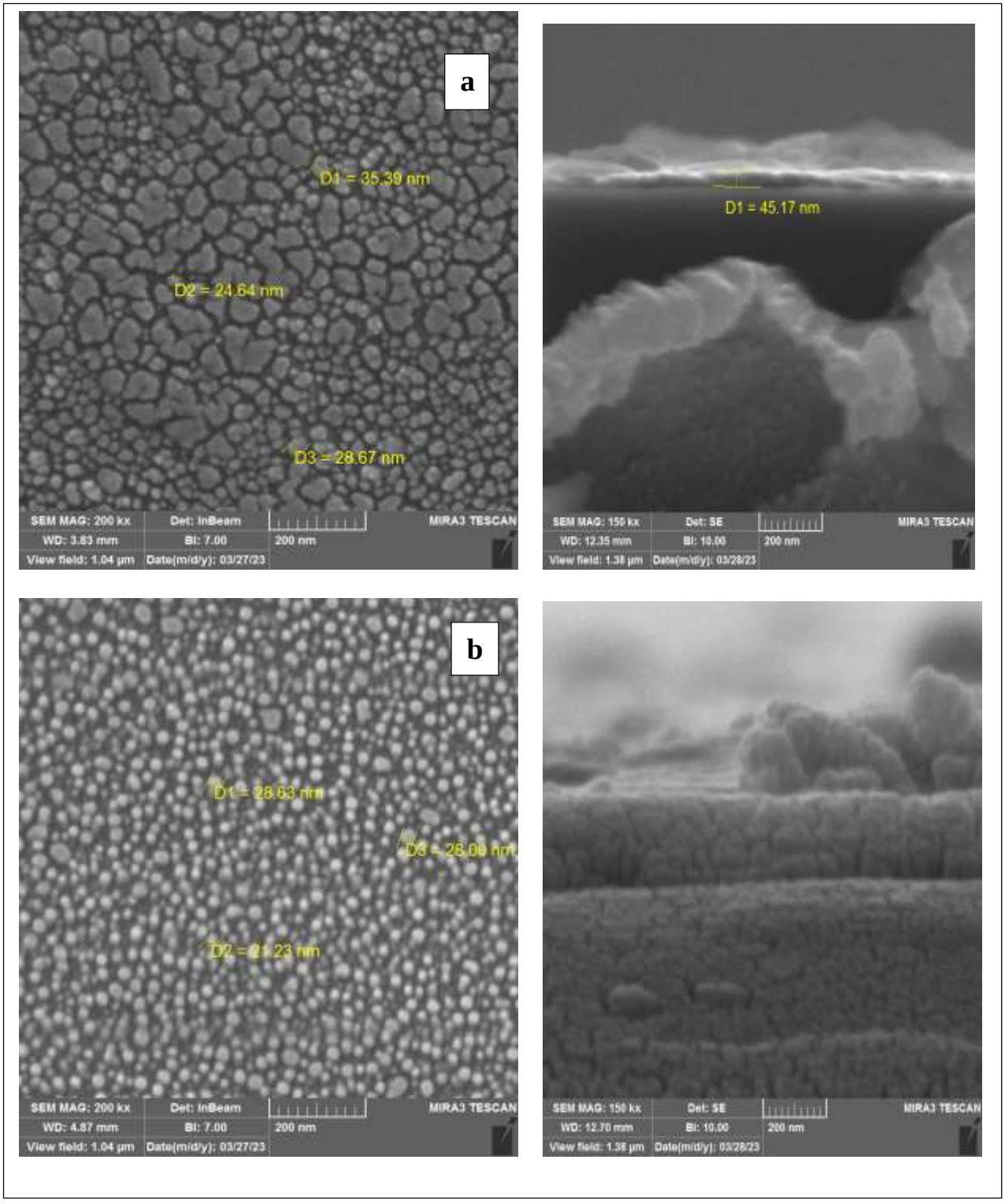

Fig. (4-7): FESEM images and cross-section of Cu_2O/SnS: (a) as deposited and (b) annealed at 200 ºC.

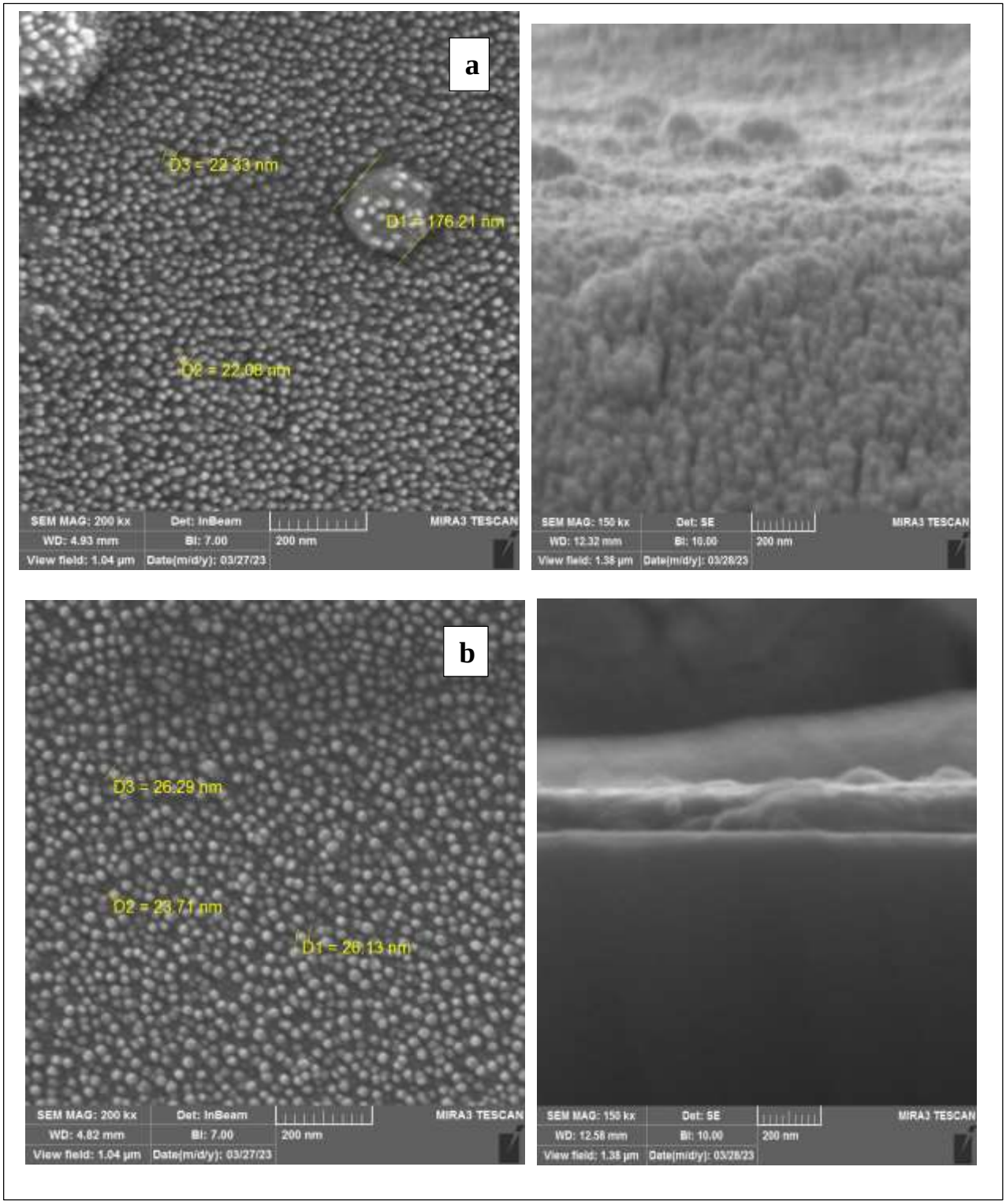

Fig. (4-8): FESEM images and cross-section of Cu_2O:SnS thin film: (a) as deposited and (b) annealed at 200 ºC.

4.2.3 Energy Dispersive Spectroscope Measurements (EDX)

Based on X-rays emitted by the sample's atoms, X-ray spectroscope is an effective technique for analyzing the chemical composition of a sample. The EDX of a Cu_2O thin film that formed onto a glass substrate can prove the presence of the elements (copper, and oxygen) that comprise the structure of the thin film. The EDX spectrum for Cu_2O thin film are clearly observable CuLα, CuKα, CuKβ and the peak for OKα lines is also clearly seen in Fig.(4-9). The atomic percentage increased from (94.87 to 97.36) for O while Cu decreased from (5.13 to 2.64) in Cu_2O thin films after annealing process as shown in Table (4-3).

In addition, the EDX analysis can provide information concerning the relative abundance of each element in the thin film and can be utilized to determine the stoichiometry of SnS compound. Elemental weights (wt.%) of Sn and S elements in the SnS thin films where the atomic percentage decreased from (70.77 to 69.23)% for S, while Sn increased from (29.23 to 30.77)% after annealing process as can be observed in Table (4-3) and chart in Fig.(4-10).

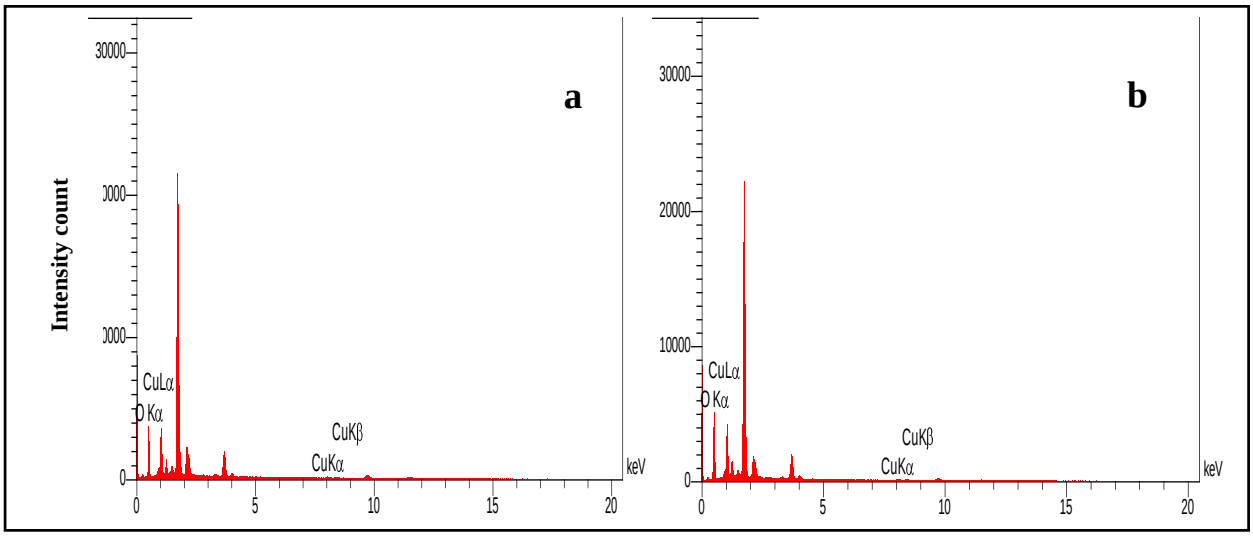

Fig. (4-9): EDX spectra of Cu_2O thin film: (a) as deposited and (b) annealed at 200 °C.

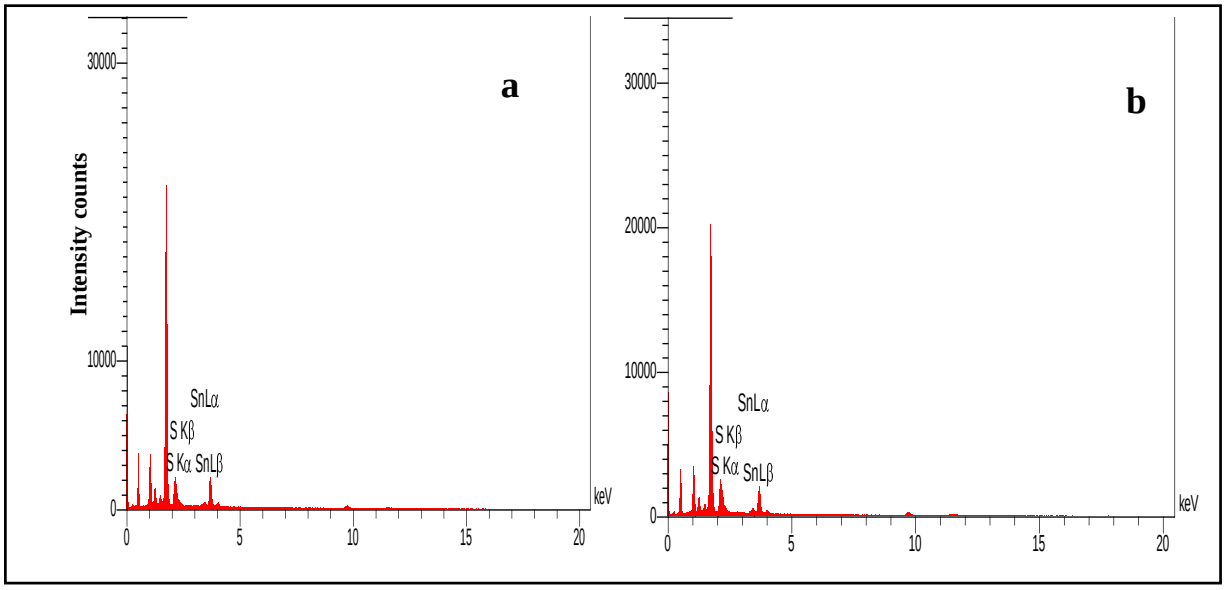

Fig. (4-10): EDX spectra of SnS thin films: (a) as deposited and (b) annealed at 200 ºC.

In Fig. (4-11) EDX analysis reveals the atomic ratio of (tin, sulphide, cupric, and oxygen) in Cu_2O/SnS thin film and in Fig. (4-12) Cu_2O:SnS thin film during growth and after the annealing process, where it was confirmed the elemental concentration of the composition of the Cu_2O/SnS and Cu_2O:SnS thin films. The atomic ratio of each element can be observed in Tables (4-3) and (4-4) as well as the EDX spectra of (CuLα,CuKα, OKα, CuKβ and SKβ,SKα ,Sn Lα,SnLβ,) lines are clearly seen for each element in the charts (4-11) and (4-12).

Table (4-3): EDX spectra of Cu_2O and SnS thin films before and after annealing process.

Samples	Element	Line	Intensity	Error	K	Kr	W%	a %
Deposited Cu_2O thin film	**O**	K series	414.6	68.3988	0.9563	0.8663	94.87	98.66
	Cu	K series	12.7	1.4091	0.0437	0.0396	5.13	1.34
					1.0000	**0.9059**	**100**	**100**
Annealed Cu_2O thin film	**O**	K series	553.6	69.4275	0.9787	0.9293	97.36	99.32
	Cu	K series	8.1	0.6586	0.0213	0.0203	2.64	0.68
					1.0000	**0.9495**	**100**	**100**
Deposited SnS thin film	**S**	K series	328.2	468.3264	0.7688	0.6709	70.77	89.96
	Sn	L series	92.6	348.7337	0.2312	0.2018	29.23	10.04
					1.0000	**0.8727**	**100**	**100**
Annealed SnS thin film	**S**	K series	433.3	361.6019	0.7537	0.6547	69.23	89.28
	Sn	L series	132.8	267.4061	0.2463	0.2140	30.77	10.72
					1.0000	**0.8687**	**100**	**100**

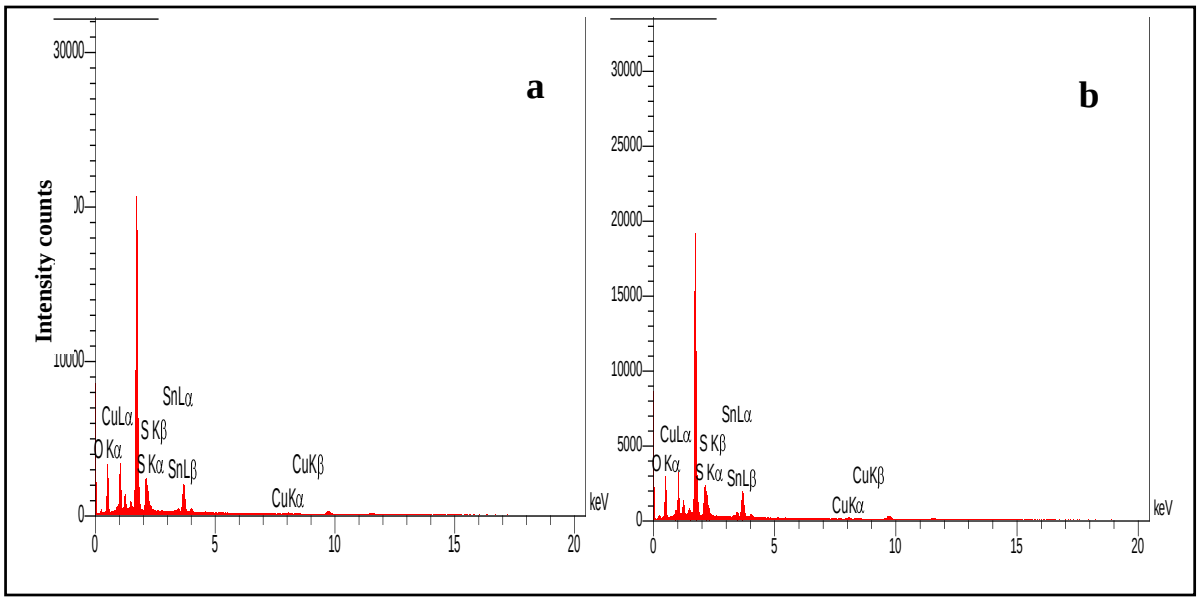

Fig. (4-11): EDX spectra of Cu_2O/SnS thin film: (a) as deposited and (b) annealed at 200 ºC.

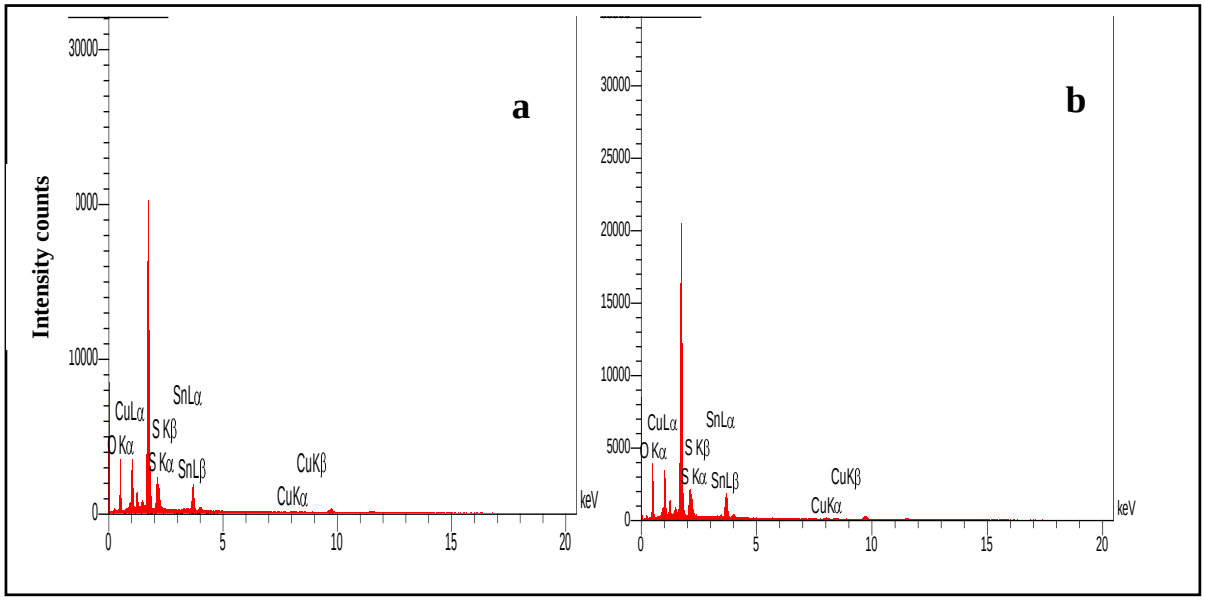

Fig.(4-12): EDX spectra of Cu_2O:SnS thin films: (a) as deposited and (b) annealed at 200 ºC.

Table (4-4): EDX spectra of Cu_2O/SnS and Cu_2O:SnS thin films before and after annealing process.

Samples	Element	Line	Intensity	Error	K	Kr	W%	a %
Deposited Cu_2O/SnS thin film	O	K series	371.5	399.912	0.3973	0.1906	64.81	81.86
	S	K series	385.9	328.150	0.4605	0.2210	25.99	16.38
	Cu	K series	13.4	1.386	0.0214	0.0103	1.29	0.41
	Sn	L series	94.9	348.827	0.1208	0.0579	7.92	1.35
					1.0000	**0.4798**	**100**	**100**
Annealed Cu_2O/SnS thin film	O	K series	325.7	405.457	0.3485	0.1692	61.45	80.05
	S	K series	402.0	336.663	0.4800	0.2331	27.32	17.76
	Cu	K series	15.1	1.764	0.0241	0.0117	1.45	0.48
	Sn	L series	115.8	403.500	0.1474	0.0716	9.77	1.72
					1.0000	**0.4855**	**100**	**100**
Deposited Cu_2O: SnS thin film	O	K series	372.3	442.216	0.4019	0.1931	65.25	81.55
	S	K series	400.9	290.636	0.4830	0.2321	27.26	17.00
	Cu	K series	13.7	0.902	0.0220	0.0106	1.33	0.42
	Sn	L series	72.5	212.054	0.0931	0.0447	6.16	1.04
					1.0000	**0.4806**	**100**	**100**
Annealed Cu_2O: SnS thin film	O	K series	421.7	447.562	0.4477	0.2147	67.79	83.33
	S	K series	368.1	277.649	0.4361	0.2092	24.74	15.18
	Cu	K series	19.0	1.427	0.0300	0.0144	1.81	0.56
	Sn	L series	68.3	273.542	0.0862	0.0414	5.66	0.94
					1.0000	**0.4796**	**100**	**100**

4.2.4 Atomic Force Microscope (AFM)

The atomic force microscope (AFM) images of the as deposited and annealed thin films in addition to the graph of the particles of investigated samples are shown in Fig.(4-13) to Fig.(4-16).

Fig.(4-13) display the AFM images of Cu_2O thin film onto a glass substrate which have been post-annealed at 200 $^{\circ}$C. The deposited sample has a small number of sharp peaks that coalesce as islands vertically to the surface of the film, where its average diameter increased from 150.5 nm to 236.3 nm after the annealing process. The values of roughness and root mean square (RMS) attained from AFM measurements have increased from (0.166 to 1.180) nm and from (0.213 to 1.490) nm respectively as well as increased the average diameter after the annealing process as listed in Table (4-5).

The AFM images of the SnS thin films on the glass substrate as fabricated and post-annealing at 200 °C are depicted in Fig. (4-14). The grain peaks of fabricated SnS thin film were round and the surface of the film appeared to be nearly flat, which diminished the clarity of the grain boundaries. After the annealing process, these peaks are pointed, sharp and the boundaries of the grains were clear. In addition, the surface is consistent and has good uniformity. Furthermore, the computed values of average roughness increased from (0.519 to 0.741) nm and root mean square (RMS) values increased from (0.718 to 0.943) nm, respectively, while the average diameters of groups of grains is decreased which revealed that the surface has nanostructure as tabulated in Table (4-5).

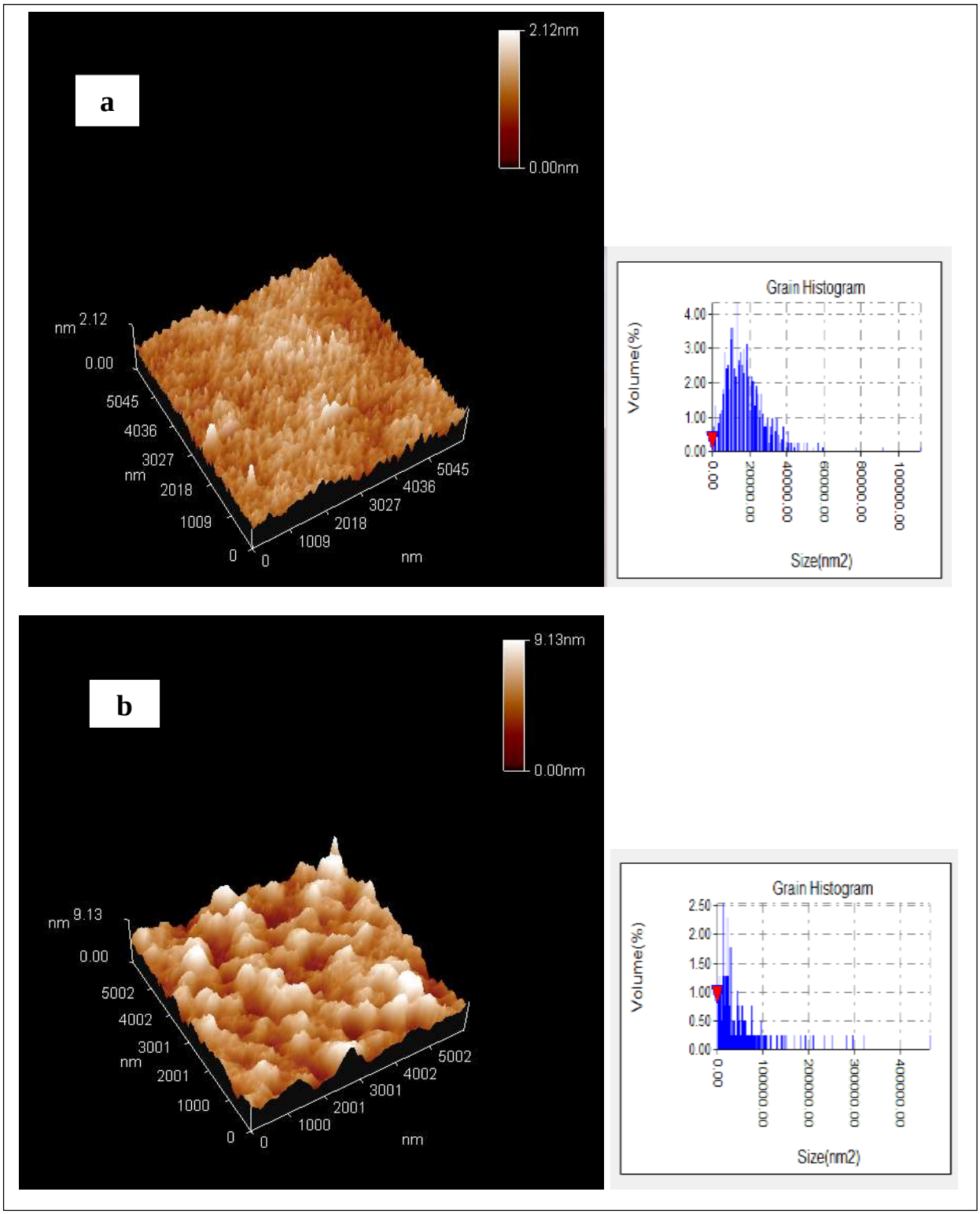

Fig.(4-13): AFM images of Cu_2O thin film: (a) as deposited and (b) annealed at 200 °C.

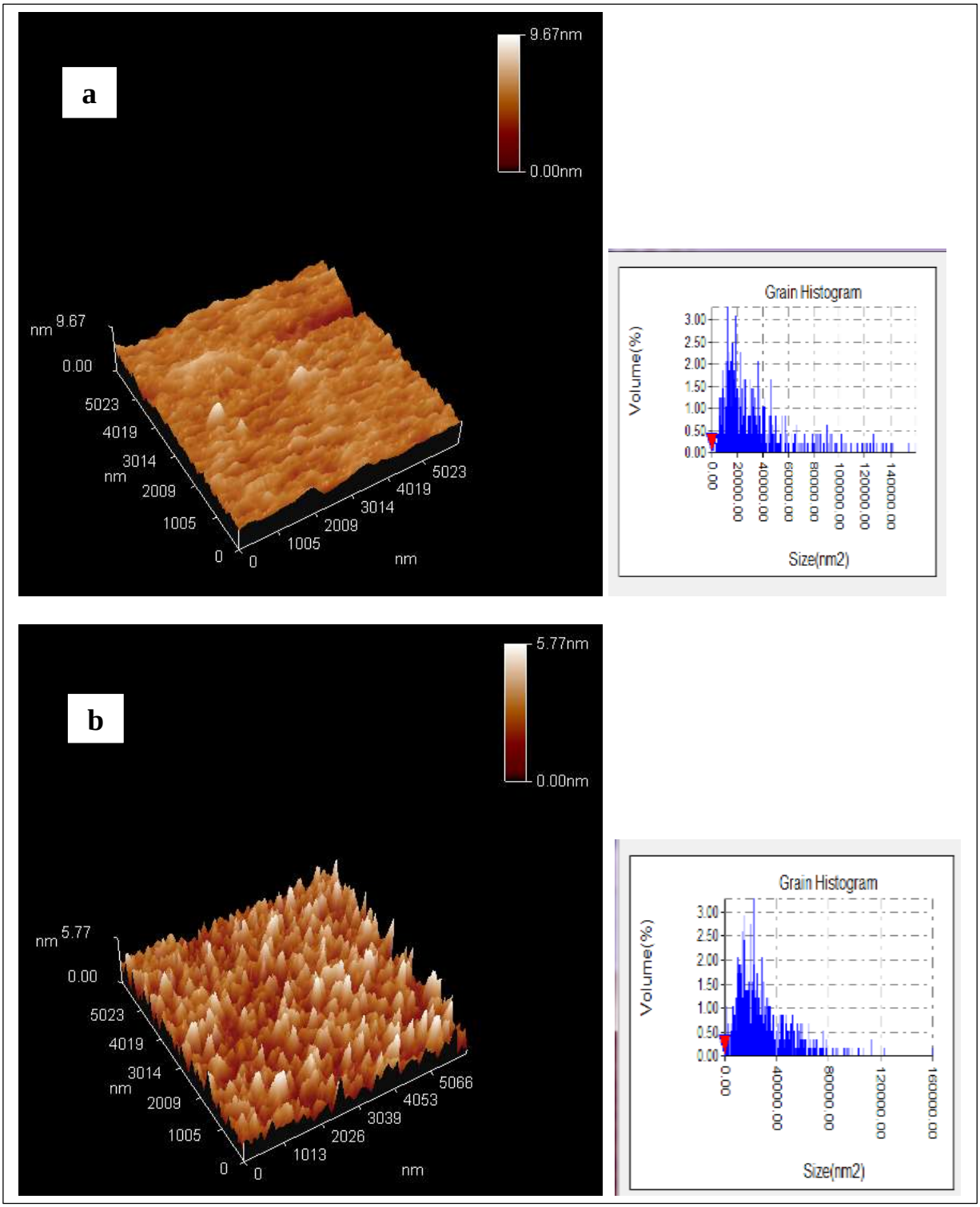

Fig. (4-14): AFM images of SnS thin film: (a) as deposited and (b)annealed at 200 °C

Fig. (4-15) shows a 3D image of Cu_2O/SnS sample, in which the regularity was observed in the film's composition and the grains have been shown to have a columnar structure on the crystallite axis than a horizontal direction and roughly equal and this might attribute to increase in RMS in addition that small values of ten-point height indicate surfaces with a fine roughness. Fig. (4-16) represents the AFM images of Cu_2O: SnS thin film, where there seems to be an irregular distribution of grains before annealing. Compared to the film grown, the film annealed at 200 °C has a substantially bigger grain height and a rougher surface. The surface roughness of films may raised because of a phase transition and the formation of large grains as a consequence of the diffusion effect when the temperature was increased by the annealing process [107]. Roughness, root mean square, and average diameter before and after the annealing process were listed in Table (4-5).

Table (4-5): AFM consequences for Cu_2O, SnS, Cu_2O/SnS, and Cu_2O: SnS thin films as prepared and as annealed

Sample	Roughness Average (nm)	Root Mean Square (nm)	Ten-point height (nm)	Average Diameter (nm)
As deposited Cu_2O	0.166	0.213	2.00	150.5
Annealed Cu_2O	1.180	1.490	8.12	236.3
As deposited SnS	0.519	0.718	5.77	211.9
Annealed SnS	0.741	0.943	7.20	194.9
As deposited Cu_2O /SnS	0.458	0.579	3.55	185.3
Annealed Cu_2O/SnS	0.678	0.879	5.25	203.8
As deposited Cu_2O:SnS	0.739	0.937	5.68	278.3
Annealed Cu_2O: SnS	4.540	5.880	28.2	393.2

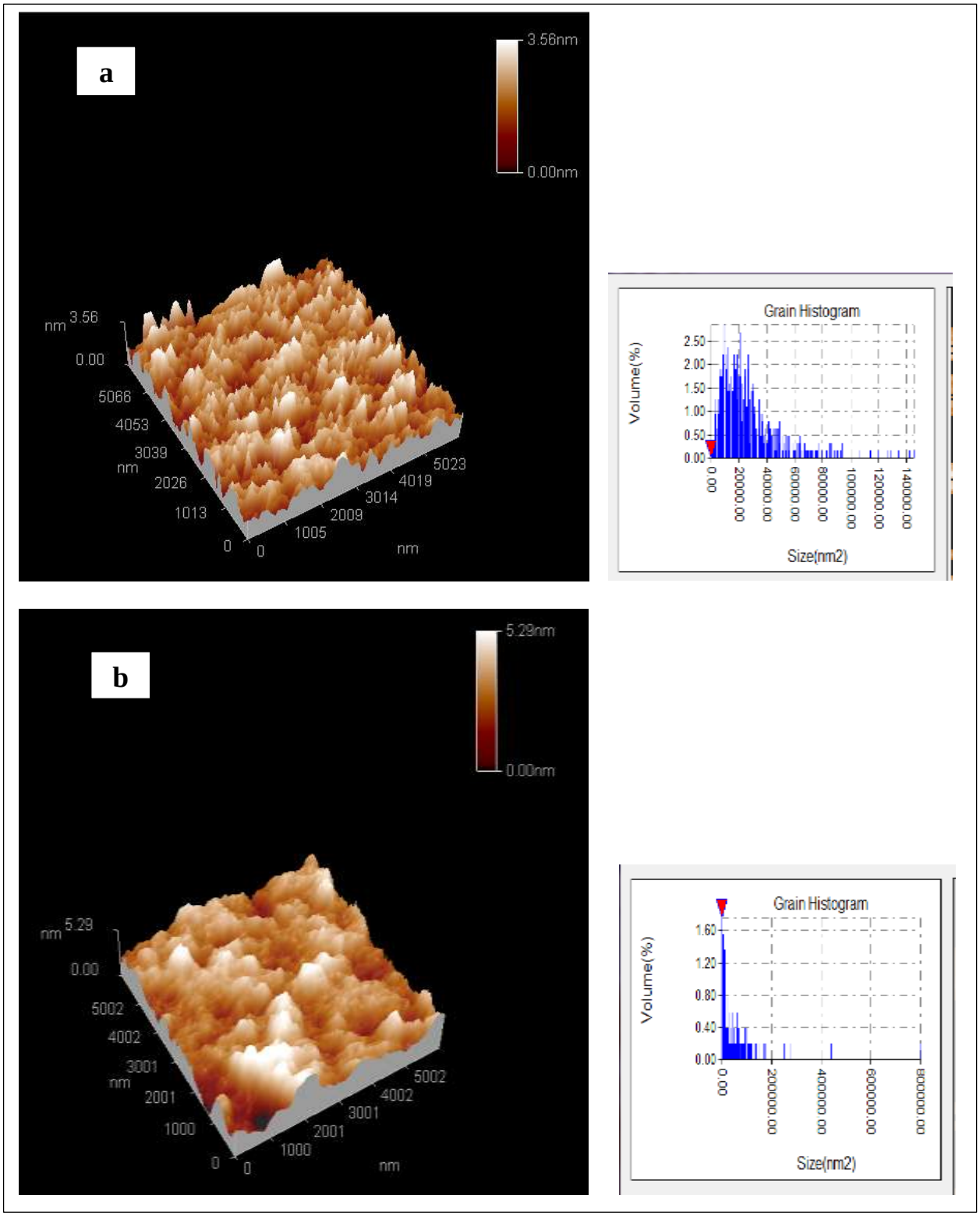

Fig.(4-15): AFM images of Cu_2O/SnS thin films: (a) as deposited and (b) annealed at 200 °C

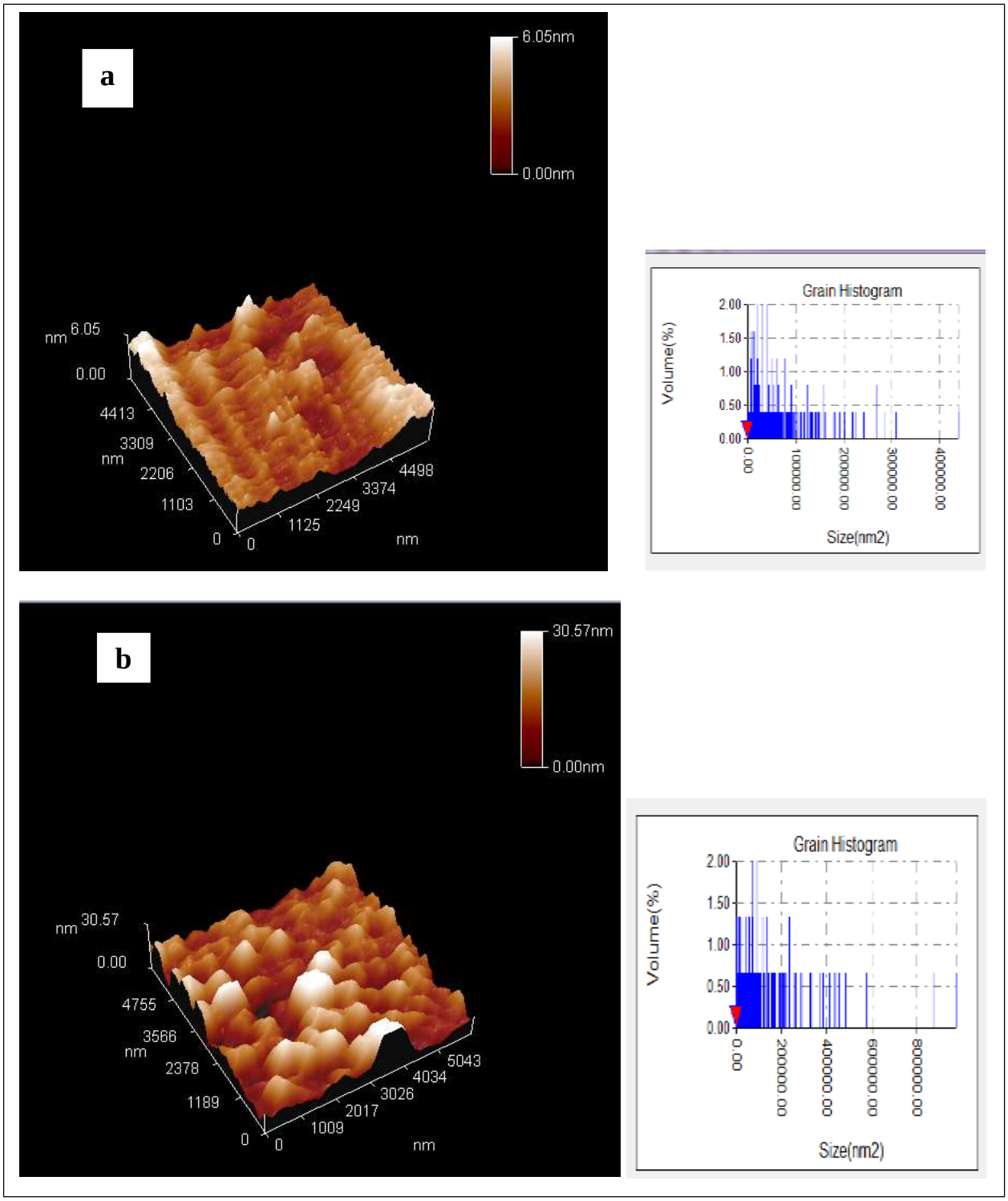

Fig. (4-16): AFM images of Cu_2O:SnS thin film: (a) as deposited and (b) annealed at 200 °C.

4.3 Optical Measurements

The optical characteristics were investigated for samples prepared by thermal evaporation. These properties include:

4.3.1 Transmittance of thin films

The chemical and crystallite structure of the film, as well as its thickness and surface morphology, all have an effect on the optical transmission spectrum.

Fig.(4-17) demonstrated the transmittance spectra of Cu_2O films as a function of photon wavelength. The value of transmittance of Cu_2O thin films is relatively high up to 98% and around 96% for fabricated and annealed samples respectively, whereas noticeable the value of transmittance of Cu_2O thin films is slightly reduced after the annealing process.

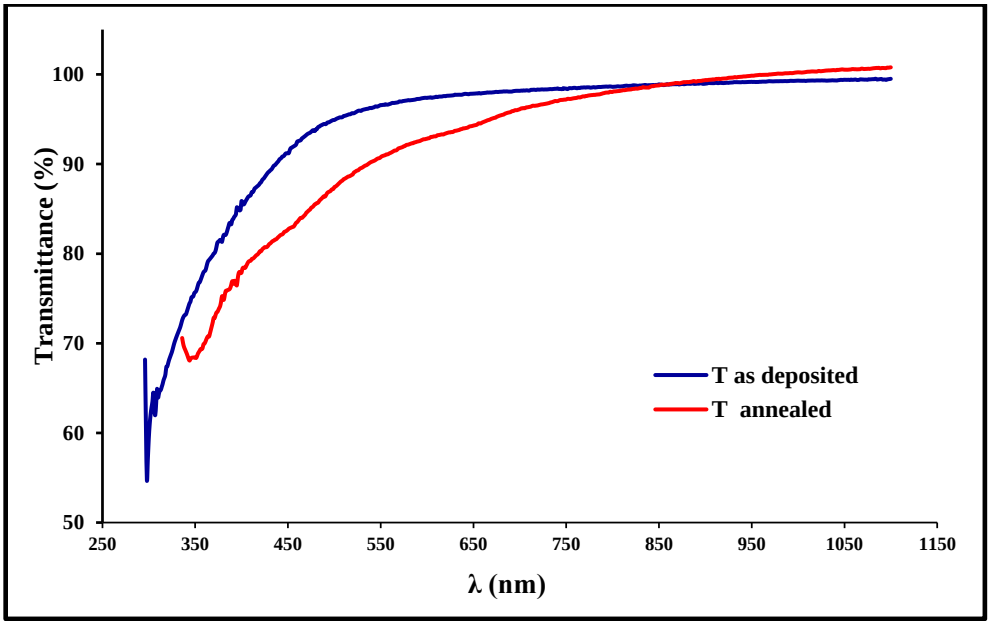

Fig. (4-17): Transmittance spectra of Cu_2O thin film before and after annealed at 200 °C.

Fig. (4-18) represents the SnS thin film spectra of optical transmission (T%) displayed in the wavelength range of (300–1100) nm. For all the films the average transmittance was observed in the visible region and increased after the annealing process.

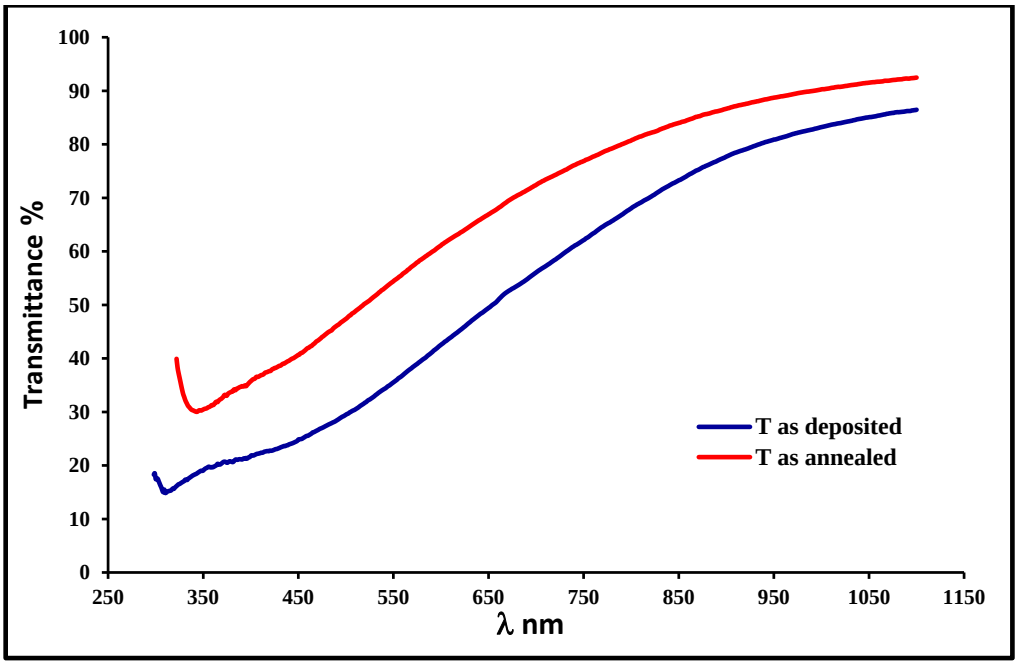

Fig. (4-18): Transmittance spectra of SnS thin film before and after annealed at 200 ° C.

Figs. (4-19) and (4-20) depicts the spectra of optical transmission (T%) of Cu_2O/SnS and Cu_2O:SnS thin films in the wavelength range of (300-1100) nm. The average transmittance in the visible region for deposited films and roughly more than 80%, for annealed samples.

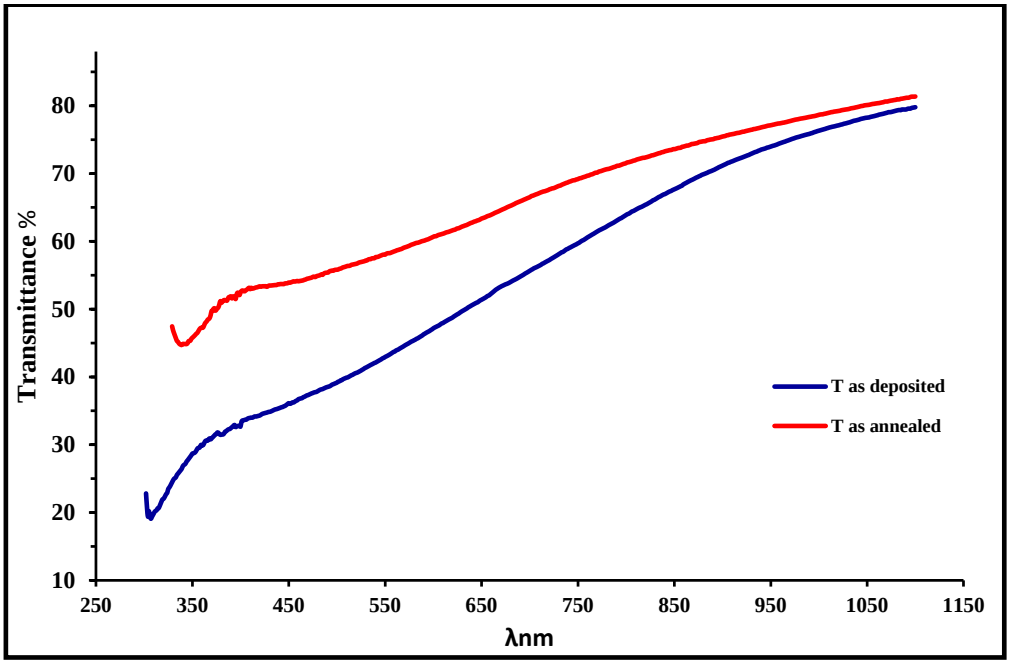

Fig.(4-19): Transmittance of Cu_2O/SnS thin film before and after annealed at 200 ˚C.

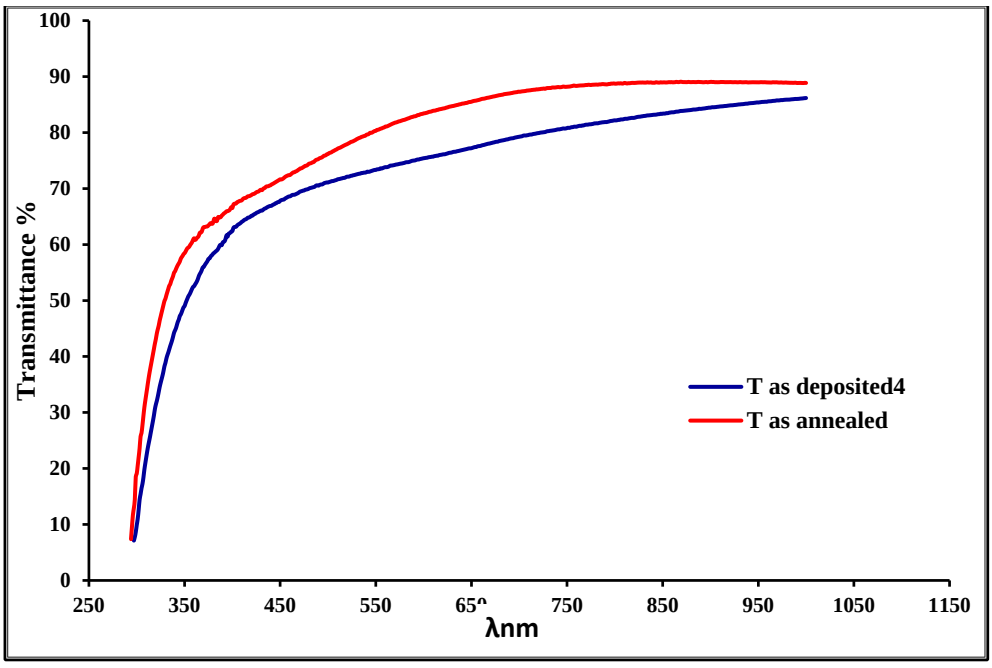

Fig. (4-20): Transmittance of Cu_2O:SnS thin film before and after annealed at 200 ˚C.

4.3.2 Absorption Coefficient

The absorption coefficient of Cu_2O is calculated using Eq. (2-9). Fig. (4-21) shows absorption coefficient as a function of photon energy. The value of absorption coefficient of Cu_2O thin films is larger than (10^4 cm^{-1}) which gives indication that the electronic transitions is direct. From the figure it can be seen the fundamental absorption edge was shifted towards the low energies (long wavelength). The values of absorption coefficient are increased significantly after annealing process, this can be attributed to the enhancement the crystallinity of the thin film as reveled by XRD and FESEM.

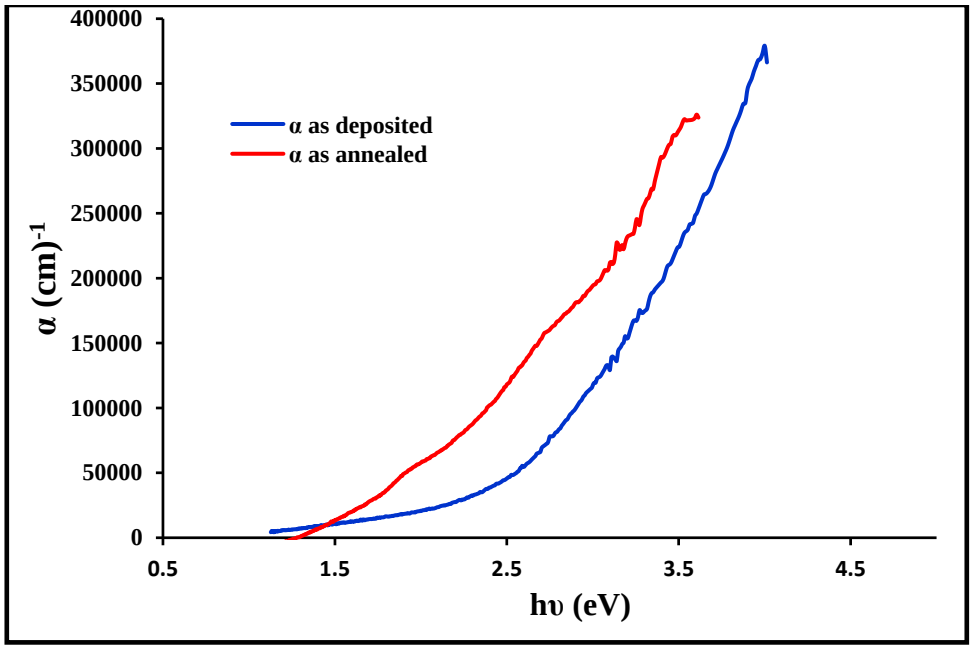

Fig. (4-21): Absorption coefficient of Cu_2O thin film as deposited and as annealed at 200 °C.

The fundamental absorption edge of SnS, Cu_2O/ SnS and Cu_2O: SnS thin film was shifted towards the higher energies (short wavelength) and reduced after annealing process as shown in Figs. (4-22),(4-23) and (4-24).

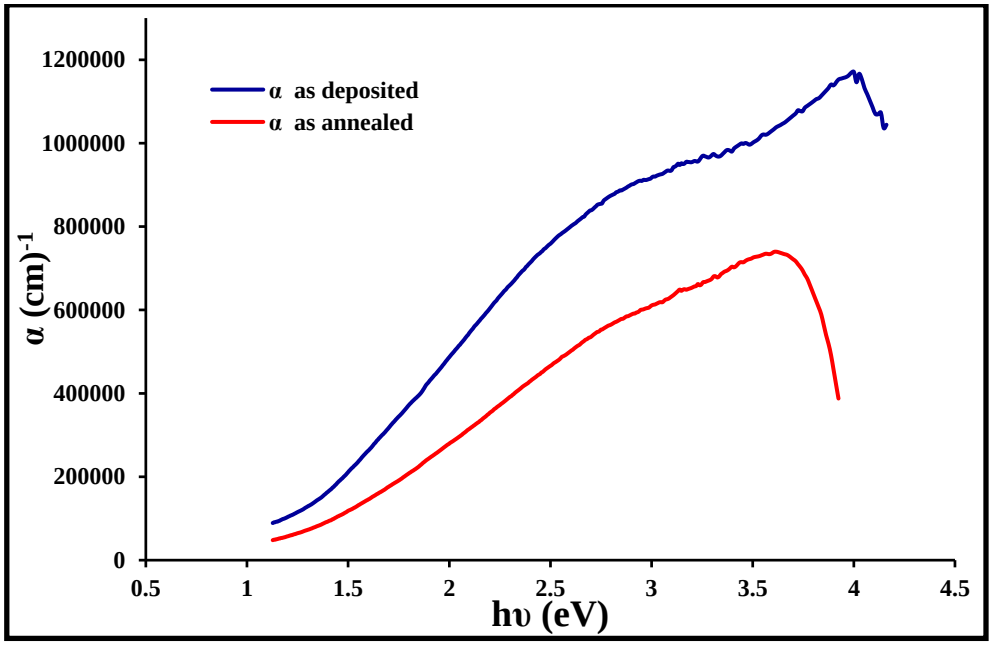

Fig. (4-22): Absorption coefficient of SnS thin film as deposited and annealed at 200 ˚C.

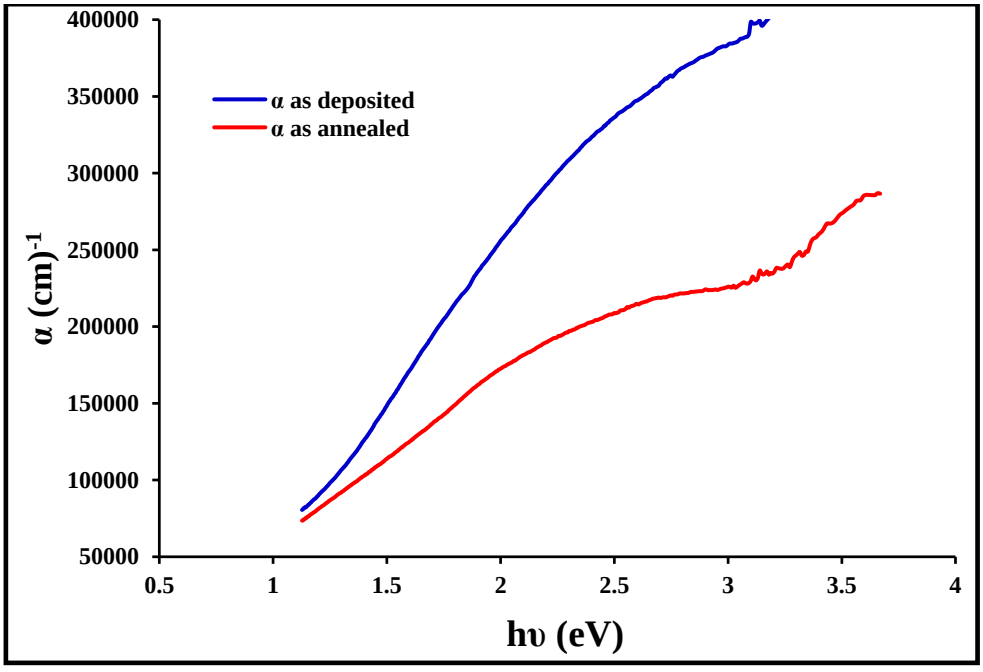

Fig. (4-23): Absorption coefficient of Cu_2O/SnS thin film as deposited and annealed at 200 ˚C.

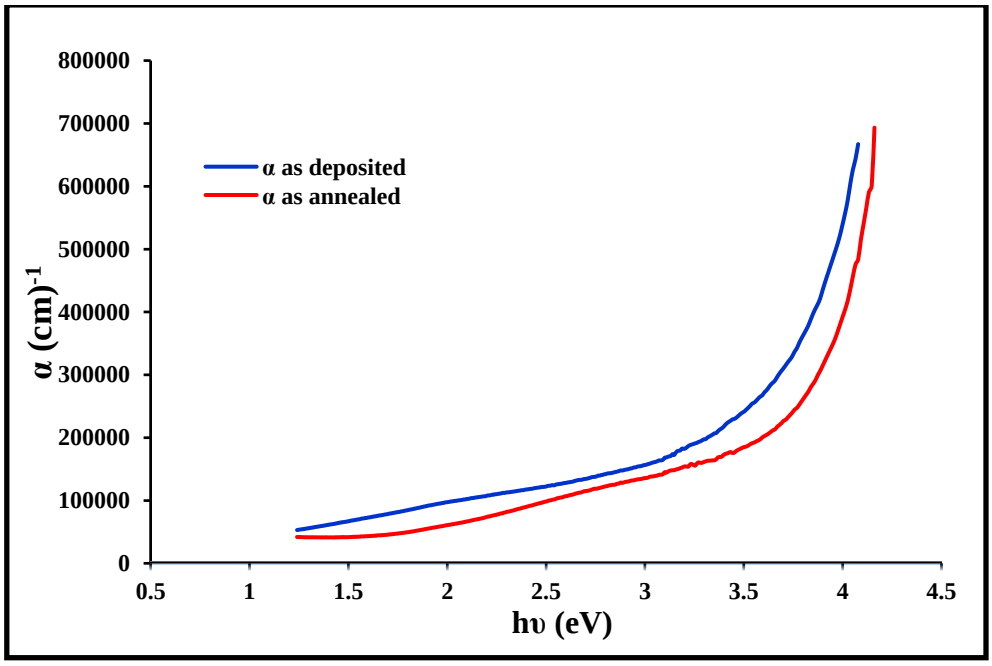

Fig. (4-24): Absorption coefficient of Cu_2O:SnS thin film as deposited and as annealed at 200 ˚C.

4.3.3 Optical energy gap

Fig.(4-25) shows the value of the optical energy band gap for allowed direct transition calculated by using Tauce relation by selecting the perfect linear part, which is determined by stretching the linear part of the curves until ($\alpha = 0$) where they intersect the axis of photon energy .

The optical energy band gap of deposited Cu_2O thin film is found to be 2.57 eV then decrease to 2.15 eV for annealed samples. The decrease in energy band gap after annealing can be attributed to improvement in the crystallinity by annealing temperature and an increase in average crystallite size as revealed by XRD and FESEM analysis. These obtained optical band gaps for Cu_2O thin films are nearly close to those reported by Akgul *et al.* [102], Oudah *et al.*, Wisz *et al.* and Bunea *et al.* [108-11].

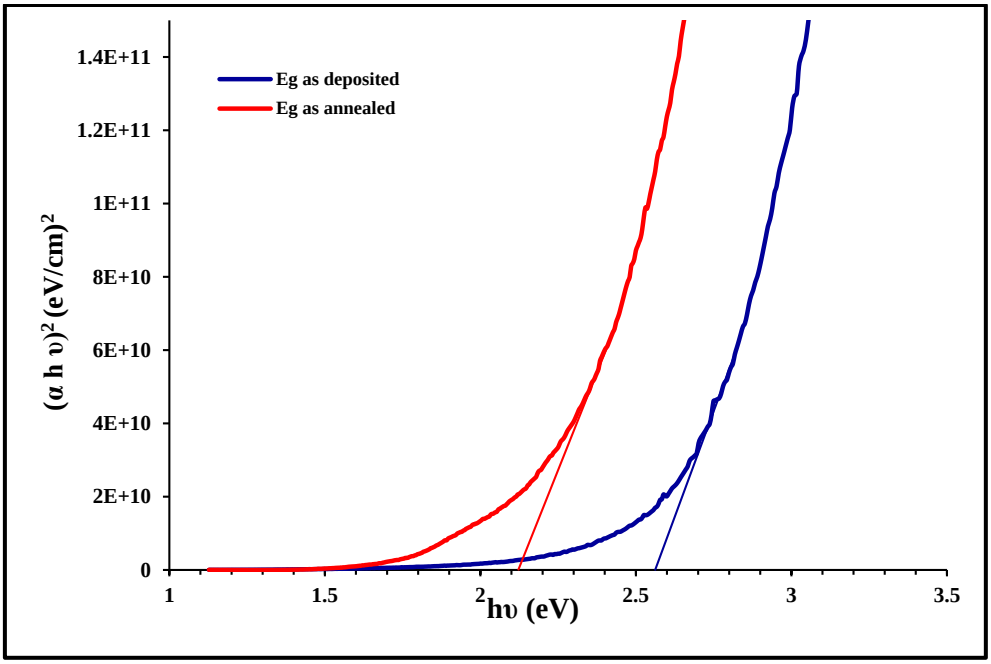

Fig. (4-25): Direct energy band gap of Cu_2O thin films as deposited and annealed at 200 °C.

The optical band gaps of fabricated SnS, Cu_2O/SnS, and Cu_2O:SnS films are (1.53, 1.75, and 3.66) eV, and after annealing, they are found to be (1.85, 1.8, and 3.86) eV respectively, as shown in Figs. (4–26), (4–27), and (4–28). The increase in band gaps might due to quantum confinement effect, which lead to the decrease in average crystallite size after annealing process, [106,111]. The reduction in crystallite size reveled by XRD and FESEM analysis.

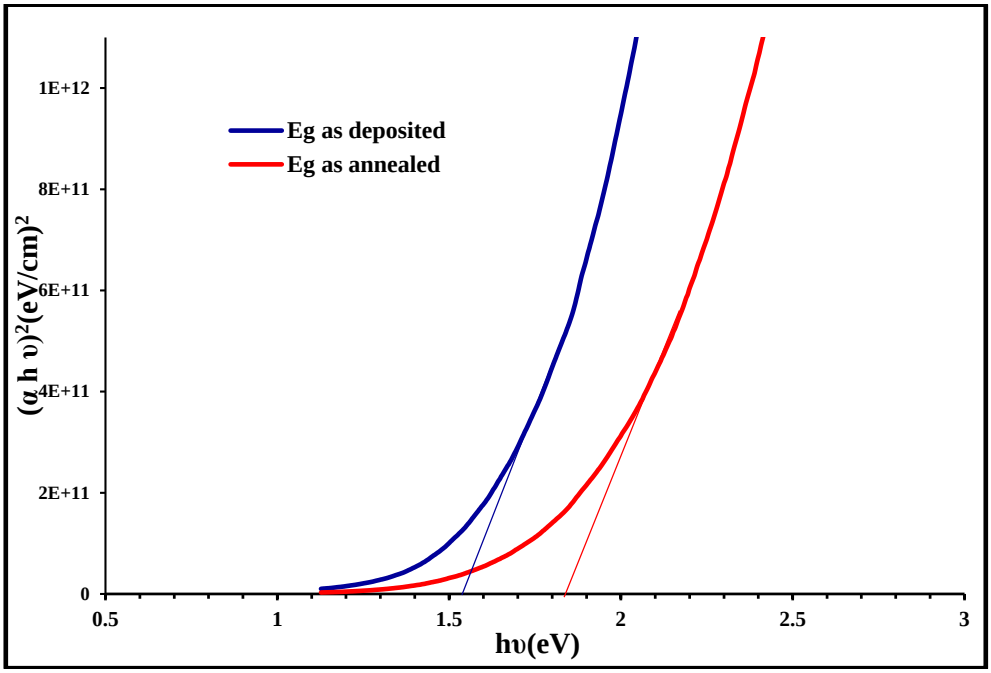

Fig. (4-26): Direct energy band gap of SnS thin films as deposited and annealed at 200 ˚C.

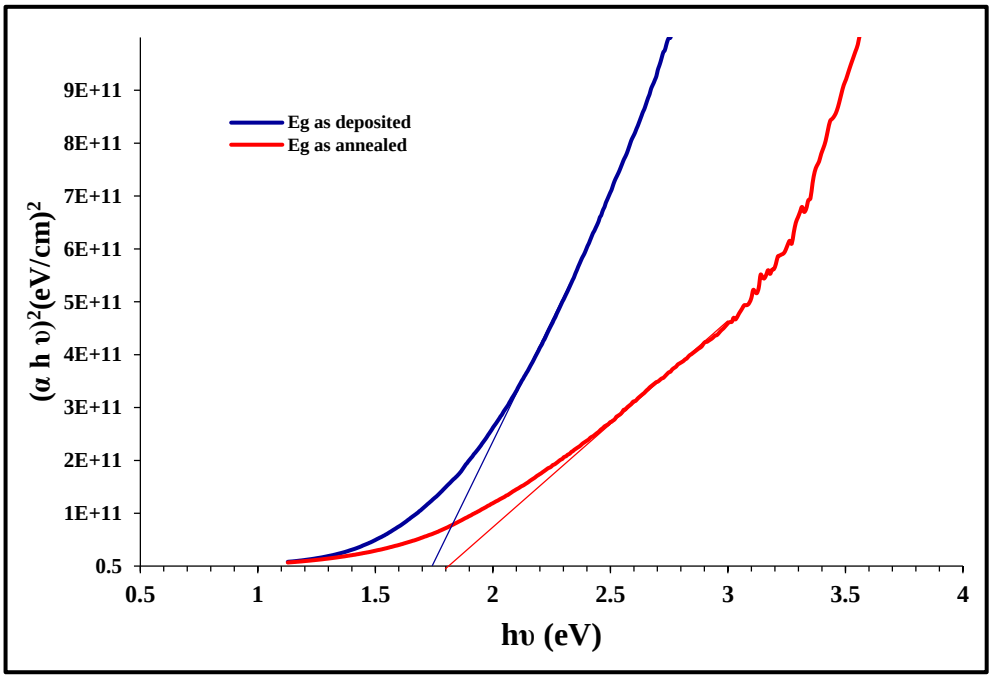

Fig.(4-27): Direct energy gap of Cu_2O /SnS thin films as deposited and annealed at 200 ˚C.

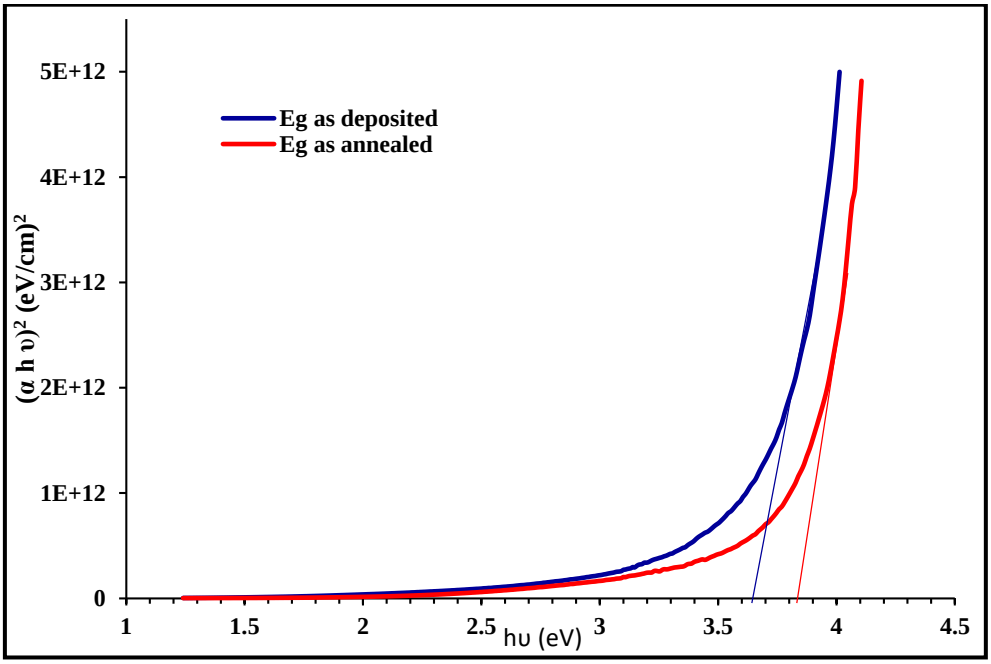

Fig. (4-28): Direct energy gap of Cu_2O:SnS thin as deposited and annealed at 200 °C.

4.3.4 Extinction Coefficient

Extinction coefficient can be defined as the amount of energy absorbed in the thin film and represent the amount of attenuation happening in the electromagnetic wave inside the material [81].

Extinction coefficient of Cu_2O thin film can be calculated using Eq.(2 -16). Fig. (4-29) shows extinction coefficient as a function of photon energy. It can be seen that k_o behaves just like the absorption coefficient (α) because they are joined by same relation. The Fig shows increase in extinction coefficient values gradually and shift toward long wavelengths as temperature increasing by annealing process.

Fig.(4-30), Fig. (4-31) and Fig.(4-32) show extinction coefficient for SnS, Cu_2O/SnS and Cu_2O:SnS thin films before and after annealed at 200 °C. The values of extinction coefficient of these samples shifted toward higher energies after the annealing process.

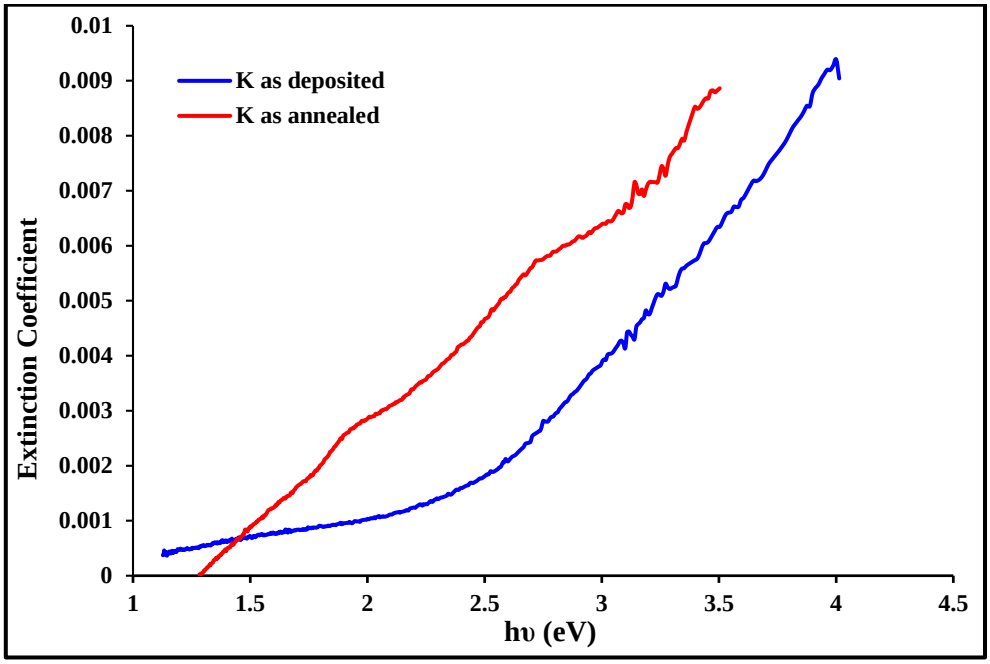

Fig. (4-29): Extinction coefficient of Cu_2O thin film as deposited and annealed at 200 ºC.

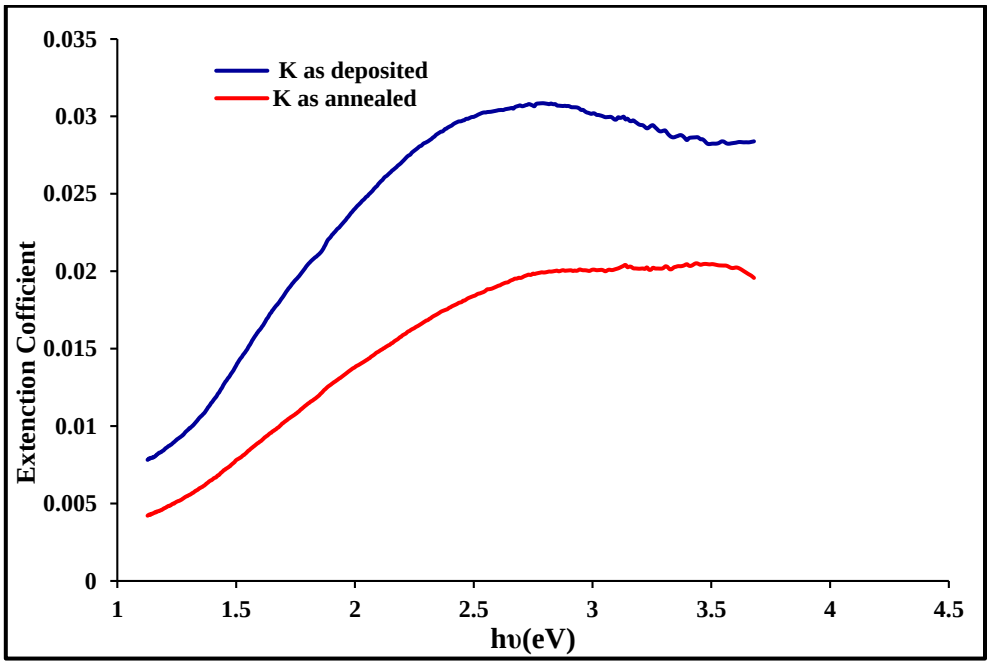

Fig. (4-30): Extinction coefficient of SnS thin film as deposited and annealed at 200 ºC.

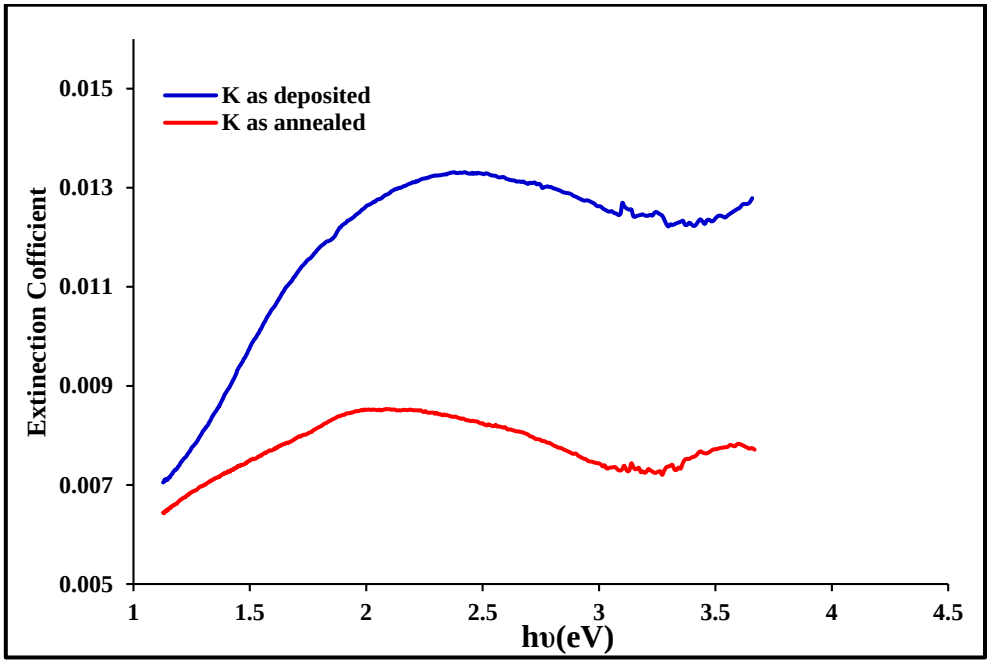

Fig. (4-31): Extinction coefficient of Cu_2O/SnS thin film as deposited and annealed at 200 °C.

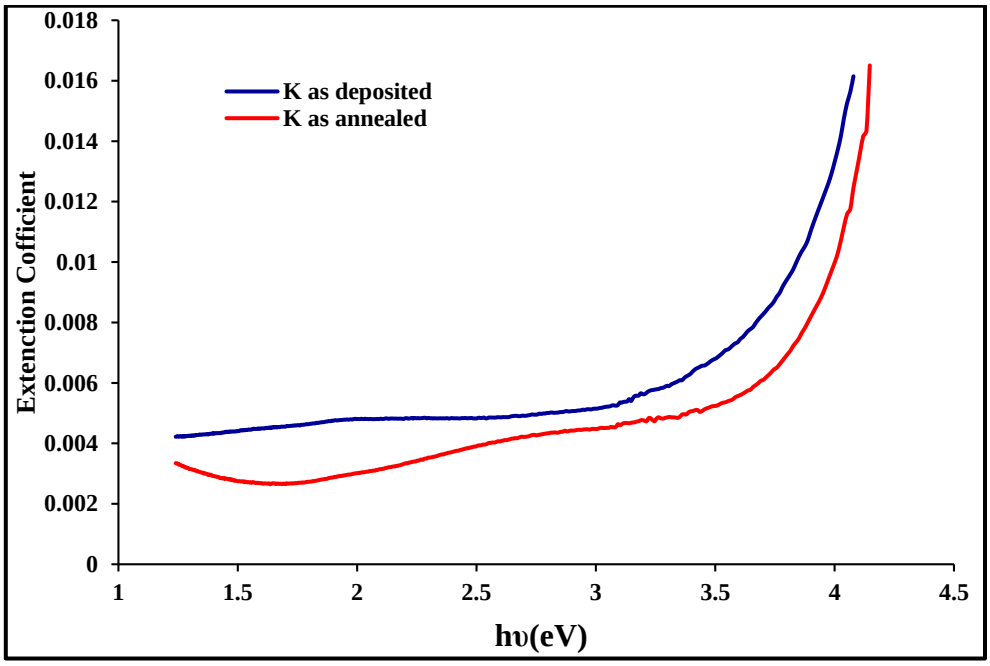

Fig. (4-32): Extinction coefficient of Cu_2O:SnS thin film as deposited and annealed at 200 °C.

4.4 Electrical Properties

The electrical properties include the charge carriers can be estimated and the Hall Effect which gives information about the type of conductivity, and concentration.

4.4.1 Hall Effect Measurements

The Hall parameters, such as, Hall coefficient (R_H) carrier concentrations (**n** and **p**) electrical conductivity (σ) and Hall mobility (μ_H) have been determined by using (Van-der Pau) method.

The measured mobility, resistivity, and carrier concentration of Cu_2O thin film are presented in Table (4-6). Increase temperature by annealing process resulted in a rise in average Hall coefficient and electrical resistivity and this behavior close to that observed by Han *et al.* [112] and Yang *et al*. [113]. The carrier concentration of the films was reduced which can be owing to the improvement of crystallite quality and the reduced crystallite defects [114].

Comparative with an as prepared SnS thin film, the semiconductor characteristics of the annealed samples enhanced. Positive Hall coefficients demonstrate that the prepared films are p-type with holes serving as the majority carriers, while the negative average Hall coefficients of annealed thin films reveal n-type conduction. The transmutation of the carrier charge type may also be attributable to an impact defect caused by crystallite growth in the material at the annealing temperature. In addition, atoms in their lattice positions oscillate thermally at annealing temperature, which might liberate one atom from its place and fill the gap left behind [103]. Table (4-6) shows that the carrier concentration and resistivity decreased after the annealing process while conductivity increased this behavior similar to that obtained by Jia *et al.*,[115]. For Cu_2O/SnS thin film resistivity and average Hall coefficient were increased from (1.699×10^4 to 5.339×10^4) Ω.cm and

(-6.397×10^{6} to 1.151×10^{7}) cm^2 /Vs respectively. Higher temperature of the annealing process urges crystal lattice vibration stronger and results in some crystal lattice defects. These defects become dispersion centers, lead to the increase of resistivity of the thin films [115]. The low mobility value of SnS single crystal and the thin film is due to the presence of a high concentration of various defects [116].

The conductivity and carrier concentration of Cu_2O:SnS thin films have been increased after annealing process as shown in Table (4-6) which lead to increase efficiency of Cu_2O:SnS /Si solar sell. All of the films exhibited n-type conductivity for both as prepared and annealed samples.

Table. (4-6): The results of Hall measurement for Cu_2O, SnS, Cu_2O/SnS and Cu_2O:SnS thin film

Sample	Carrier type	Resistivity (Ω cm)	Hall Mobility (cm^2 /Vs)	Carrier Concentration (cm^{-3})	Average Hall coefficient (cm^2 /Vs)	Conductivity $(\Omega\ cm)^{-1}$
as deposited Cu_2O	n-type	1.426E+5	1.056 E+2	-4.144E+11	-1.506E+7	7.012E-6
annealed Cu_2O	p-type	2.598E+5	7.229 E+1	3.323E+11	1.878E+7	3.849E-6
as deposited SnS	p-type	3.008E+4	5.261 E+1	3.945E+11	1.582E+7	3.325E-6
annealed SnS	n-type	2.974E+4	2.230E+ 3	-9.415 E+10	-6.630E+7	3.363E-5
as deposited Cu_2O /SnS	n-type	1.699E+4	3.765E+2	-9.758E+11	-6.397E+6	5.886E-5
Annealed Cu_2O /SnS	p-type	5.339E+4	2.156E+2	5.423E+11	1.151E+7	1.873E-5
as deposited Cu_2O :SnS	n-type	1.148E+5	2.272E+2	-2.393E+11	-2.609E+7	8.708E-6
Annealed Cu_2O: SnS	n-type	1.067E+5	6.846E+1	-8.544E+11	-7.306E+6	9.370E-6

4.4.2 C-V Characteristic Heterojunction Solar Cell

Capacitance-voltage measurement is one of the most important methods for obtaining information about the rectifying junctions, built-in potential, and junction capacitance and junction type [117]. Fig. (4-33) gives the variation of ($1/C^2$) vs (V) measurements for different samples. From this Figs., it can be seen that a straight line, of which the intercept with the voltage axis gives the value of the built-in potential for annealed Cu_2O/Si, SnS/Si, Cu_2O/ SnS/Si and Cu_2O:SnS/Si heterojunction. The linear relationship of I/C^2-V curve suggests that the junction is abrupt type [118-120].

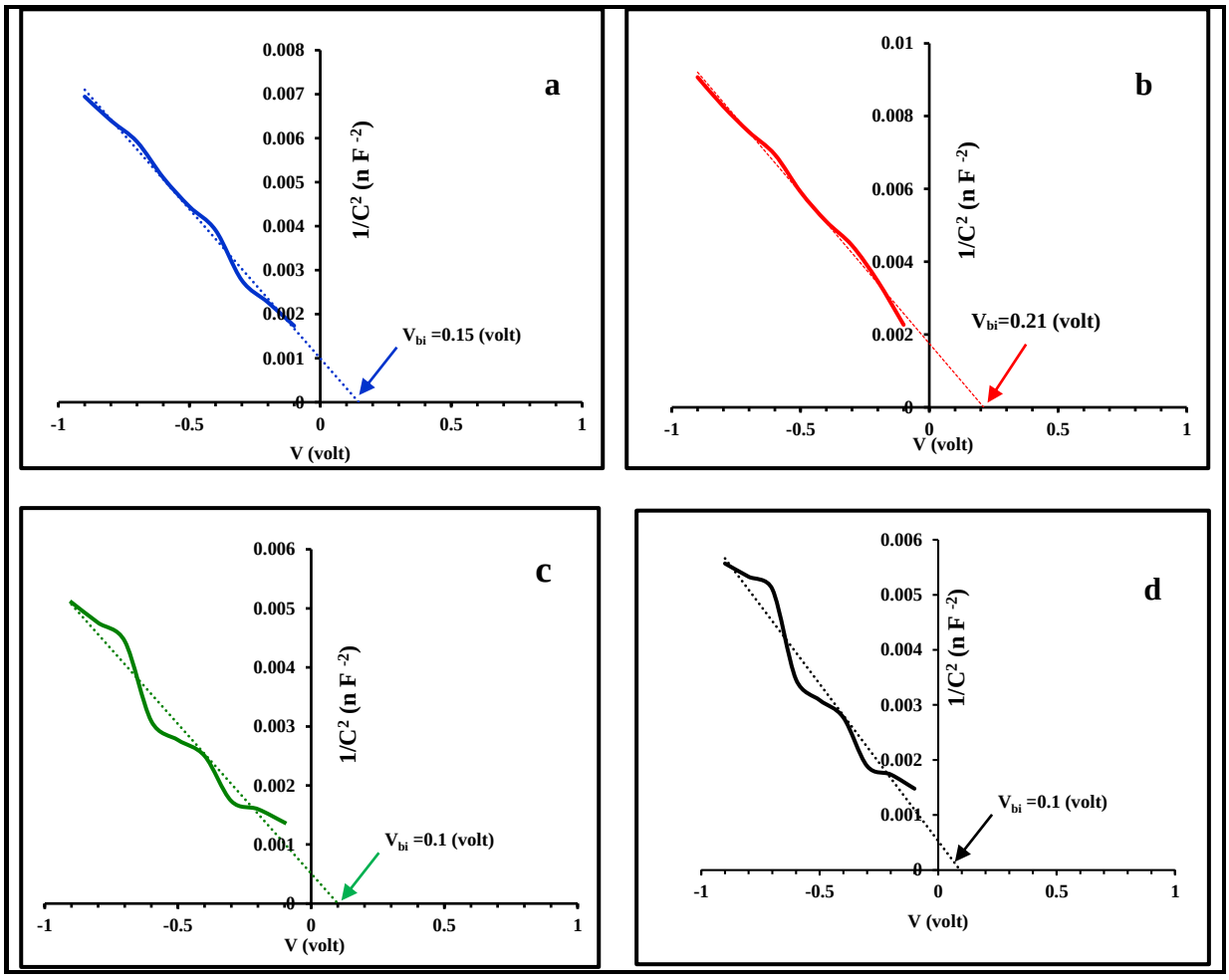

Fig. (4-33): The variation of capacitance as a function of voltage for annealed: (a) Cu_2O/Si, (b) SnS/Si, (c) Cu_2O/SnS/Si and (d) Cu_2O: SnS /Si heterojunction solar cell.

Also it can be seen that junction capacitance is inversely proportional to the bias voltage for all samples, which can be explained by the expansion of depletion layer width with the built-in potential [119], the result was listed in Table (4-7).

4.4.3 Characterizations of Solar Cell under Illumination

The current-voltage (I-V) characteristics of solar cell with active area of 0.35 cm^2 was carried on incident power densities equal to 100 mW/cm^2 and the solar cell efficiency was measured at room temperature; this is to avoid the variation of efficiency with temperature of environment. The results are demonstrated in the Figs. (4-34)- (4-37) and it was listed in Table (4–7).

The (I-V) curves can be used to determine the relation between the increasing photocurrent and bias voltage. Additionally, the photocurrent in the reverse bias was higher than that in the forward bias. This might due to the increase in the width of the depletion region as the reverse bias applied voltage increased, leading to the separation of electrons and hole pairs [42].
The efficiency of Cu_2O /n-Si and SnS/Si solar cell was 3.37% and 6.27% respectively.
The value of efficiency that obtained for Cu_2O/SnS/Si solar cell was 4.62% and this result nearly close to that obtained by Cho *et al*.,[42].

The maximum efficiency of solar cell was 7.44 % for Cu_2O:SnS/Si solar cell this might attributed to that the annealing temperature gives more roughness to the surface and raises the absorption of incident photons and this lead to increase the efficiency of solar cell. The parameters of solar cells were calculated from such as short circuit current (I_{SC}), open circuit voltage (V_{OC}), fill factor (F.F) and efficiency (η) as shown in Table (4-7) and that results close to obtained by researchers [43],[45],[50], [121] and [122].

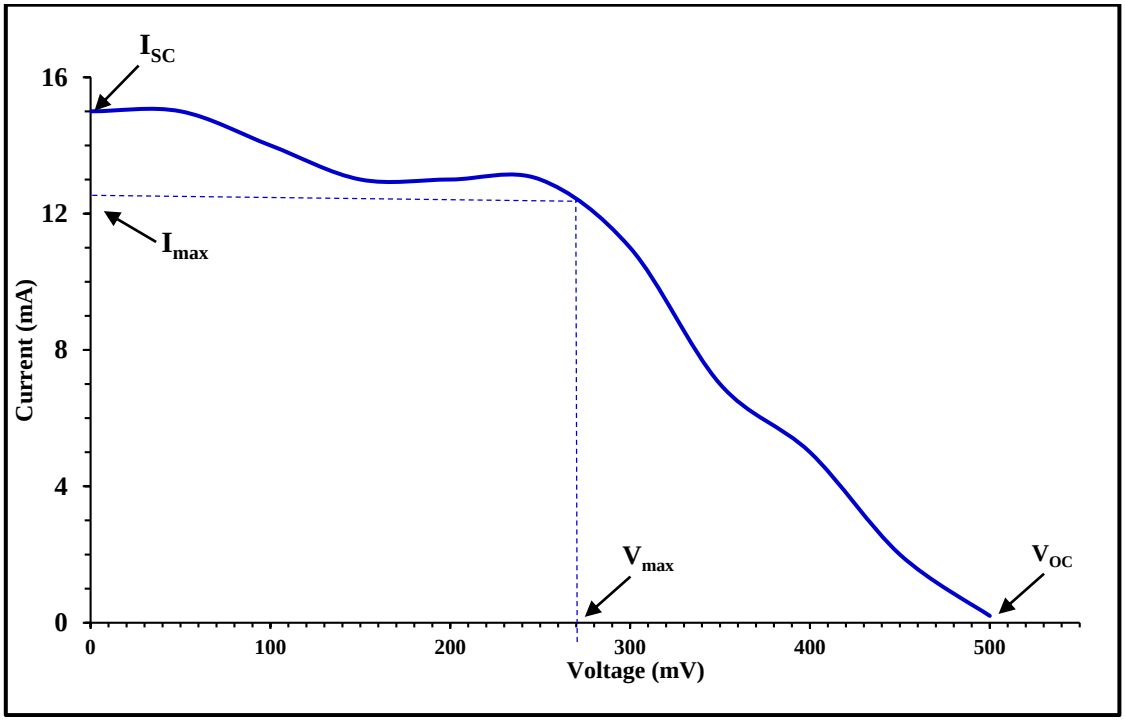

Fig. (4-34): I-V Characteristics of Cu_2O/Si solar cell (under illumination).

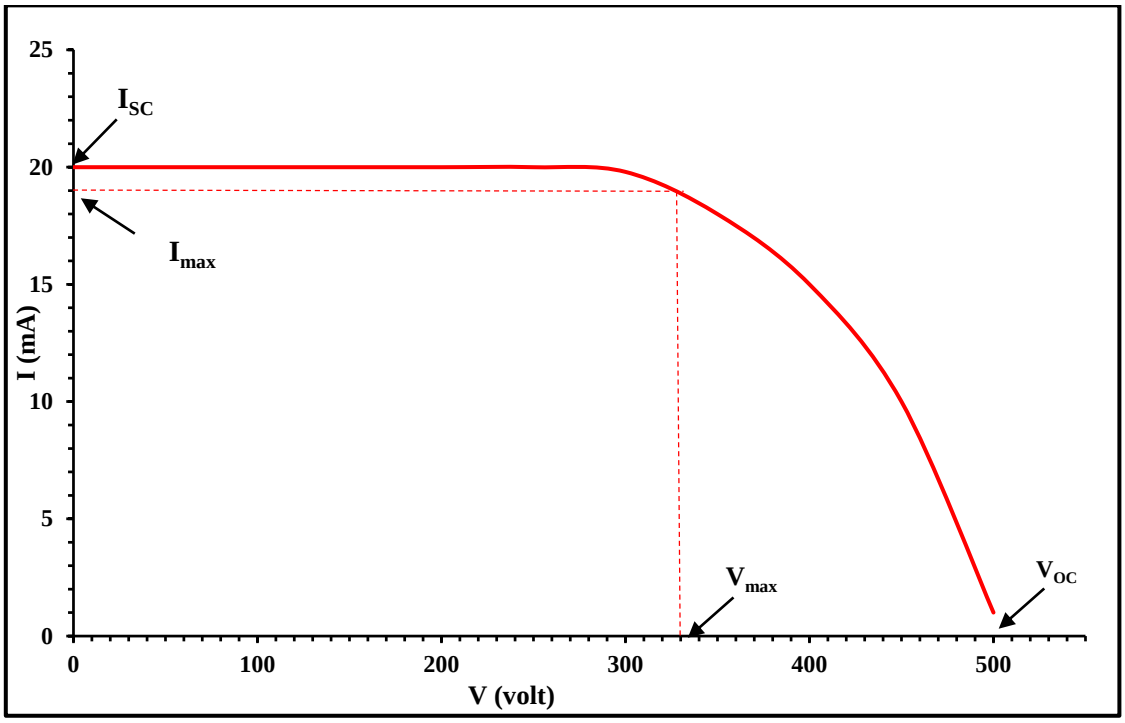

Fig. (4-35): I-V Characteristics of SnS/Si solar cell (under illumination).

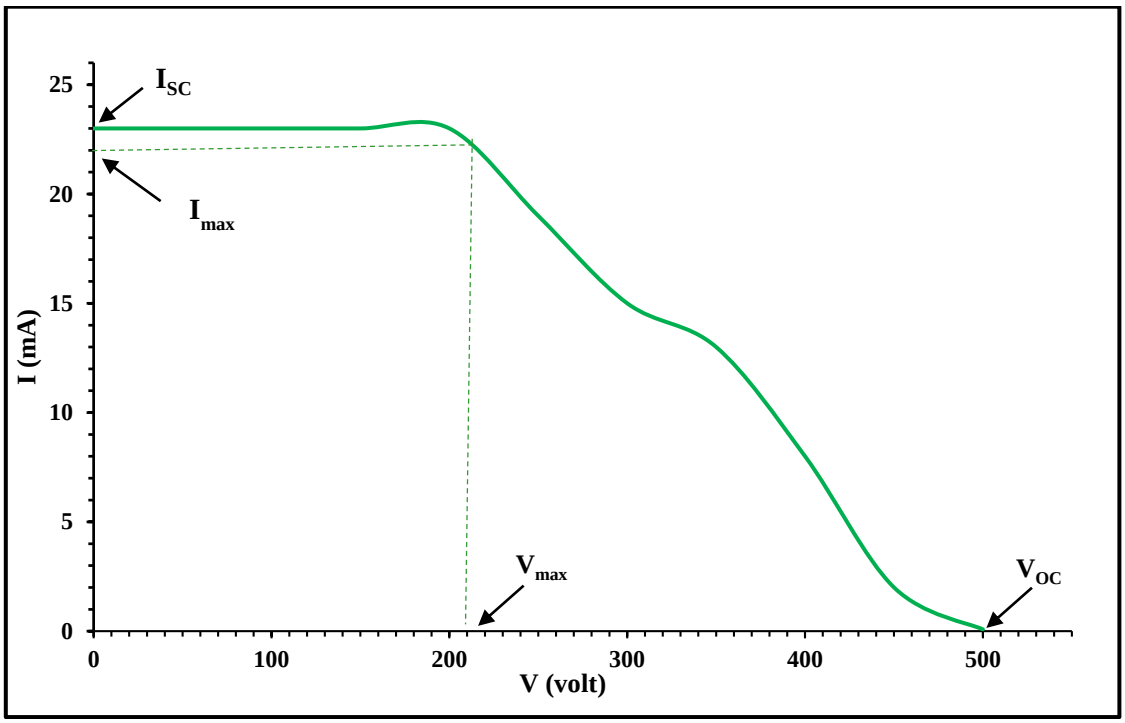

Fig. (4-36): I-V Characteristics of Cu_2O/SnS/Si solar cell (under illumination).

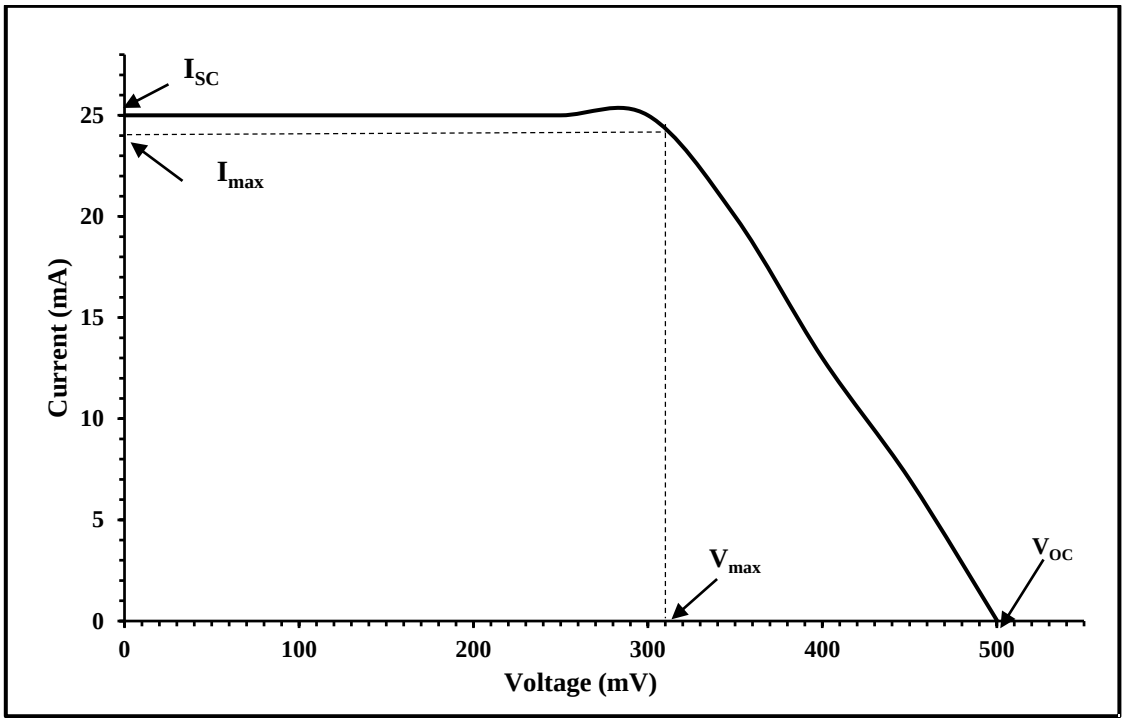

Fig. (4-37): I-V Characteristics of Cu_2O:SnS/Si solar cell (under illumination).

Table (4-7): The results of the I-V characteristics for different annealed films.

Samples	I_{max} (mA)	V_{max} (m V)	I_{SC} (mA)	V_{OC} (mV)	*F.F*	η (%)	V_{bi} (V)
Annealed Cu_2O /n-Si	12.5	270	15	500	0.45	3.37	0.21
Annealed SnS/n-Si	19	330	20	500	0.836	6.27	0.15
Annealed Cu_2O /SnS/n-Si	22	210	23	500	0.61	4.62	0.1
Annealed Cu_2O: SnS/n-Si	24	310	25	500	0.992	7.44	0.1

4.5 Conclusions

From overall the results and measurements, this thesis has concluded the following points:

1- Cuprous Oxide, Tin sulfide, Cuprous Oxide/Tin sulfide, Cuprous Oxide : Tin sulfide thin films have been successfully prepared on glass and silicon substrates using the thermal technique.

2-The XRD analysis show that the average crystallite size of Cu_2O thin film was increased and the average crystallite size of the SnS, Cu_2O/SnS and Cu_2O:SnS decreased after annealed at 200°C.

3- (FESEM) images of samples show a homogenous, uniform surface with no pinholes or cracks after the annealing process.

4- The average roughness, root mean square, average diameters and ten point hight that obtained from AFM measurements for all samples increased after the annealing process.

5- The UV-Vis optical studies showed that the value of energy gap of Cu_2O thin films it decreased after annealing process and the energy gap of the SnS, Cu_2O/SnS and Cu_2O:SnS thin films were increased after annealing .

6- The optical studies displays that the absorption edge of the fabricated SnS, Cu_2O/ SnS and Cu_2O: SnS thin films shifted towards shorter wavelength after the annealing process, while the absorption edge of Cu_2O samples toward longer wavelength.

7- The results of Hall measurements varied between an increase and a decrease in Hall parameters such as charge carrier concentration, Hall coefficient, and mobility after the annealing process.

8- The capacitance of the sample heterojunction decreases with increasing the reverse bias voltage and the maximum value that obtained of the built-in potential (V_{bi}) for SnS/n-Si of (0.21) volt.

9- The maximum values of open circuit voltage, short circuit current and fill factor obtained for Cu_2O: SnS/n-Si solar cell.

10- Best result was obtained of efficiency was for Cu_2O: SnS/n-Si solar cell at which the reached to (η = 7.44)%.

4.6 Future Work

Among future work that can be performed to elucidate the characteristics of Cu_2O, SnS, Cu_2O /SnS Cu_2O **:** SnS thin films are:

1- Preparing and characterizing Cu_2O / SnS/Si thin films by spray pyrolysis technique and annealing the samples at different temperatures such as (400, 450, 500, 550) ºC and comparing the obtained results with this work.

2 - Studying the efficiency of the prepared solar cell as function of thickness

3- Effect of doping on the structural, electrical, optical and photoluminescence properties of SnS thin film and studying the effect of doping on the physical characteristics of the Al/ SnS /Si/Al solar cell.

References

References

[1] S. P. Sukhatme and J. K. Nayak, **Solar Energy: Principles of Thermal Collection and Storage,** Mc Graw-Hill, India, (2009).

[2] N.S. Seroka , R.Taziwa and L.Khotseng, **Solar Energy Materials-Evolution and Niche Applications:A Literature Review**, Materials ,Vol. 15,No.5338, pp. 1-28, (2022).

[3] M.Arun, **Types of Solar Cells and its Applications**, International Journal of Scientific Development and Research (IJSDR), Vol.4, Issue2, (2019).

[4]S. S. Li, **Semiconductor Physical Electronics, 2nd ed.,** Springer Science and Business Media, LLC, New York, (2006).

[5]M. V. Dambhare, B.Butey and S. V. Moharil, **Solar Photovoltaic Technology: A Review of Different Types of Solar Cells and its Future Trends,** Journal of Physics: Conference Series, Vol. 1913, No.012053, pp.1-16, (2021).

[6] A. M. Bagher, M. M. A. Vahid and M. Mohsen, **Types of Solar Cells and Application**, American Journal of Optics and Photonics, Vol.3, No.5, pp.94-113, (2015).

[7] K. Ranabhat, L. Patrikeev, A. A. Revina, K. Andrianov, V. Lapshinsky and E. Sofronova**, An Introduction to Solar Cell Technology,** Review Paper, Vol. 14, No. 4, pp. 481- 491, (2016).

[8] S. Sharma, K. K. Jain, A. Sharma, **Solar Cells: In Research and Applications A Review,** Materials Sciences and Applications**,** Vol. 6,pp.1145-1155, (2015).

[9] D. Alagarasan, S. S. Hegde, S. Varadharajaperumal, R.Aadhavan ,R.Naik , M.Shkir ,H.Algarni and R.Ganesan, **Effect of SnS Thin Film Thickness on Visible Light Photo Detection**, Phys. Scr.,Vol. 97 ,No. 065814, pp. 1-13, (2022).

[10] P. Sateesh and P. Madhusudhanarao, **Structural and Electrical Properties of SnS Thin Films via Chemical Bath Deposition Technique**, International Journal of Latest Trends in Engineering and Technology, Vol.8,Issue1, pp.413-422, (2019).

[11] L.A. Burton, D.Colombara, R.D. Abellon, F. C. Grozema, L.M. Peter,T.J.Savenije,G.Dennler, and A. Walsh, **Synthesis**, **Characterization, and Electronic Structure of Single-Crystal SnS, Sn_2S_3, and SnS_2**, Chem. Mater.,Vol. 25, pp.4908−4916, (2013).

[12] T.H. Sajeesh, A.S.Cherian, C. S.Kartha and K.P. Vijayakumar, **Engineering Structural and Opto-Electronic Properties of SnS Films Deposited using Chemical Spray Pyrolysis Technique by Controlling pH of the Precursor Solution**, Energy Procedia,Vol. 15, pp. 325 – 332, (2012).

[13] K. Hartman, J.L. Johnson, M. I. Bertoni, D.Recht, M. J. Aziz, M. A. Scarpulla and T. Buonassisi, **SnS Thin-Films by RF Sputtering at Room Temperature**, Thin Solid Films, Vol. 519, pp. 7421–7424, (2011).

[14] E. Guneri, C. Ulutas, F. Kirmizigul, G. Altindemir, F. Gode and C. Gumus, **Effect of Deposition Time on Structural, Electrical, and Optical Properties of SnS Thin Films Deposited by Chemical Bath Deposition**, Applied Surface Science, Vol. 257 pp.1189–1195, (2010).

[15] P. Sinsermsuksakul, J. Heo , W. Noh , A. S. Hock ,and R. G. Gordon, **Atomic Layer Deposition of Tin Monosulfide Thin Films**, Adv. Energy Mater, Vol. 1, pp.1116–1125, (2011).

[16] H. Choi, N. Lee, H. Park, Y. Choi, K. Kim,Y. Choi, J. Kim, S. Song, H. Yuk and H. Jeon, **Development of a SnS Film Process for Energy Device Applications**, Journals Applied Sciences Vol. 9,Issue 21, pp.1-12, (2019).

[17] N. Koteeswara Reddy, M. Devikab and E. S. R. Gopal, **Review on Tin (II) Sulfide (SnS) Material: Synthesis, Properties, and Applications**, Critical Reviews in Solid State and Materials Sciences, Vol. 40, Issue 6, pp.1-40, (2015).

[18] S. A. Kissin and D. R. Owens, **New Data on Stannite and Related Tin Sulfide Minerals,** The Canadian Mineralogist, Vol.17, p.125, (1979).

[19] M. Calixto-Rodriguez, H. Martinez, A. Sanchez-Juarez, J. Campos-Alvarez, A. Tiburcio-Silver and M.E. Calixto, **Structural, Optical, and Electrical Properties of Tin Sulfide Thin Films Grown by Spray Pyrolysis**, Thin Solid Films, Vol.517, pp. 2497–2499, (2009).

[20] Z. Xu and Y. Chen , **Synthesis of SnS Thin Films from Nano-Multilayer**, Energy Procedia,Vol.10,pp.238-242, (2011).

[21] M. Umar, M.Y. Swinkels, M. De Luca, C. Fasolato, L.Moser, G. Gadea, L. Marot,T. Glatzel and I. Zardo, **Morphological and Stoichiometric Optimization of Cu_2O Thin Films by Deposition Conditions and Post-Growth Annealing**, Thin Solid Films, Vol. 732, No. 138763,pp.1-11, (2021).

[22]C. Ravichandiran, A. Sakthivelu, R. Davidprabu, S. Valanarasu , A. Kathal inm,V. Ganesh, M. Shkir, H. Algarni and S. AlFaify,**In-Depth Study on Structural, Optical, Photoluminescence and Electrical Properties of Electrodeposited Cu_2O Thin Films for Optoelectronics: An Effect of Solution pH** , Microelectronic Engineering, Vol. 210, pp. 27–34, (2019).

[23] A. Mittiga, E. Salza, F. Sarto, M. Tucci, and R. Vasanthi, **Heterojunction Solar Cell with 2% Efficiency Based on a Cu_2O Substrate**, Appl. Phys. Lett. 88, No.163502,pp.1-2, (2006).

[24] K.U. Isah, M.M. Bakeko, U. Ahmadu, U.E. Uno, M. I. Kimpa and J. A.Yabagi, **Effect of Oxidation Temperature on the Properties of Copper Oxide Thin Films Prepared from Thermally Oxidized Evaporated Copper Thin Films,** (IOSR) Journal of Applied Physics, Vol. 3, Issue 2 ,pp. 61-66, (2013).

[25] J. Liang , N. Kishi , T.Soga, T. Jimbo and M. Ahmed, **Thin Cuprous Oxide Films Prepared by Thermal Oxidation of Copper Foils with Water Vapor**, Thin Solid Films ,Vol.520,pp.2679–2682, (2012).

[26] O. S.Samuel, A. Olanrewaju and A. K. David**, Optical Properties of Cu_2O Thin Films Impregnated with Carbon Nanotube (CNT)**, Pertanika J.Sci. and Technol,Vol.30,No.1, pp. 343 – 350, (2022).

[27] P.Sawicka-Chudy, M. Sibi´nski, E. Rybak-Wilusz, M.Cholewa, G. Wisz, and R. Yavorskyi, **Review of the Development of Copper Oxides with Titanium Dioxide Thin-Film Solar Cells**, AIP Advances, Vol. 10, p.010701, (2020).

[28] B. K. Meyer , A. Polity, D. Reppin , M. Becker, P. Hering, P. J. Klar, Th. Sander, C. Reindl, J. Ben M. Eickhoff1, C. Heiliger, M. Heinemann, J. Bla¨sing, A. Krost, S. Shokovets, C. Muller and C. Ronning, **Binary Copper Oxide Semiconductors: From Materials Towards Devices**, Phys. Status Solidi B, Vol. 249, Issue 8, pp.1-23, (2012).

[29] S. L. Pal, U. Jana, P. K. Manna, G. P. Mohanta and R. Manavalan**, Nanoparticle: An Overview of Preparation and Characterization,** Journal of Applied Pharmaceutical Science, Vol. 1 No.6, pp. 228-234, (2011).

[30] V. Pokropivny, R. Lohmus, I. Hussainova, A. Pokropivny and S. Vlassov, **Introduction to Nanomaterials and Nanotechnology**, Tartu University Press, pp. 45-100, (2007).

[31] F. Findik, **Nanomaterials and their Applications, Periodicals of Engineering and Natural Sciences**, Vol. 9, No. 3, pp.62-75, (2021).

[32]S. C. Singh, H. Zeng, C. Guo, and W. Cai, **Nanomaterials Processing and Characterization with Lasers**, Wiley-VCH Verlag and Co. KGaA, Germany, (2012).

[33] M. Huston, M. DeBella, M. DiBella and A. Gupta**, Green Synthesis of Nanomaterials,** Nanomaterials, Vol. 11, No. 2130,pp.1-30,(2021).

[34] C.M. Mc-Shane, W. P. Siripala and K-S. Choi, **Effect of Junction Morphology on the Performance of Polycrystalline Cu_2O Homojunction Solar Cells**, J. Phys. Chem. Lett., Vol.1, pp. 2666–2670, (2010).

[35] T. Dimopoulos, A. Pei´c, S. Abermann, M. Postl, E.J.W. List-Kratochvil, and R. Resel, **Effect of Thermal Annealing in Vacuum on the Photovoltaic Properties of Electrodeposited Cu_2O-Absorber Solar Cell**, EPJ Photovoltaics, Vol. 5, pp. 1-6, (2014).

[36] Y. Kawano, J. Chantana and T. Minemoto, **Impact of Growth Temperature on the Properties of SnS Film Prepared by Thermal Evaporation and its Photovoltaic Performance**, Current Applied Physics, Vol. 15, Issue 8, pp. 897-901, (2015).

[37]A. El-Shaer, M.T.Y. Tadros, and M.A. Khalifa, **Fabrication of Homojunction Cuprous Oxide Solar Cell by Electrodeposition Method**, Nature and Science, Vol.13, No.5, pp.1-22, (2015).

[38] N. K. Samani, Z.De. Tafti, H. A. Bioki ,M. B. Zarandi and S. Shayegh, **Annealing Effect on Structural and Optical Constants of SnS Thin Films for Solar Cells Application**, Optik, Vol. 131, pp. 231–241, (2017).

[39] F.J. Hamood, Q. M. hadi, K.H. Abass and M.K. Mohammed, **Influence of Annealing Temperature on Structural and Optical Properties of SnS:Ag Thin Film for Solar Cell Application**, International Journal of Engineering and Technology,Vol.7, No. 4.36, (2018).

[40] S.S. Hegde, A.G. Kunjomana , P. Murahari , B.K. Prasad and K. Ramesh, **Vacuum Annealed Tin Sulfide (SnS) Thin Films for Solar Cell Applications**, Surfaces and Interfaces,Vol.10, pp. 78-84, (2018).

[41] Z. D. Tafti, M. B. Zarandi and H.A. Bioki, **Thermal Annealing Influence Over Optical Properties of Thermally Evaporated SnS/CdS Bilayer Thin Films**, Journal of Optoelectronical Nanostructures,Vol.4, Issue 1, pp.87-98, (2019).

[42] J.Y. Cho, S.Y. Kim, R. Nandi, J. Jang, H-S. Yun, E. Enkhbayar, J. H. Kim, D-K. Lee, C-H. Chung, J.H. Kim, and J. Heo**, Achieving Over 4% Efficiency for SnS/CdS Thin-Film Solar Cells by Improving Heterojunction Interface Quality,** Journal of Materials Chemistry A, Issue 39, pp.1-10, (2020).

[43] A.N. Tuama, K. H. Abass and M. A. Agam**, Fabrication and Characterization of Cu_2O:Ag/Si Solar Cell via Thermal Evaporation Technique,** International Journal of Nanoelectronics and Materials, Vol.13, No.3, pp.601-614, (2020).

[44] C. Jayathilaka, L. S. R. Kumara, K. Ohara, C. Song, S. Kohara, O. Sakata, W. Siripala and S. Jayanetti, **Enhancement of Solar Cell Performance of Electrodeposited Ti/n-Cu_2O/p-Cu_2O/Au Homojunction Solar Cells by Interface and Surface Modification**, Crystals, Vol. 10, pp.1-14, (2020).

[45] T. D. Nguyen , V. T. Dang , N. M.Hung , V. K. Arepalli , J. Kim , M. Raj and T.T. O. Nguyen, **Synthesis of Ag-Embedded SnS Films by the RF Method for Photovoltaic Applications**, Surfaces and Interfaces, Vol.25, No.101151, pp. 1-6, (2021).

[46] S. Kawanishi, I. Suzuki, S. R. Bauers, A. Zakutayev, H. Shibata, H. Yanagi, and T. Omata, **SnS Homojunction Solar Cell with n-Type Single Crystal and p-Type Thin Film**, Solar. RRL, 5, pp. 1-7, (2021).

[47] S.A. Zaki, M.I. Abd-Elrahman , A.A. Abu-Sehl, M. Almokhtar, A.S. Soltan and N. M. Shaalan, **Solar Cell Fabrication from Semiconducting Binary Tin Sulfide Alloy on Si Substrate**, Solar Energy, Vol. 228, pp. 206–215, (2021).

[48] D. Alagarasan, S. Varadharajaperumal, K. D. A. Kumar, R. Naik, S. Umrao, M. Shkir, S. AIFaify and R. Ganesan, **Influence of Nanostructured SnS Thin Films for Visible Light Photo Detection**, Optical Materials, Vol.121, p.111489, (2021).

[49] R. Balakarthikeyan, A. Santhanam , Aslam Khan , Ahmed M. El-Toni, Anees A. Ansari, A. Imran, M.Shkir and S. Al Faify, **Performance Analysis of SnS Thin Films Fabricated Using Thermal Evaporation Technique for Photodetector Applications**, Optik**,** Vol.244, p.167460, (2021).

[50] K. H. Abass, A. Adil, A. J.Alrubaie, B. H. Rabee, A. M. Kadim, S. H. Talib, K.A. Mohammed and A. S. Jassim, **Fabrication and Characterization of p-SnS/n-Si Solar Cell by Thermal Evaporation Technique and the Effect of Ag-doped on Its Efficiency**, International Journal of Nanoscience, Vol.22, Issue 1,p. 2350003, (2023).

[51] M. Abdurrahman, F.W. Burari, M. A. Haruna, I.Aminu, T.Abdullahi, O.W. Olasoji, M. Shehu, H.Y. Shuaibu, M.T. Garba and J. Mohammed, **An Affordable Fabrication and Synthesis of Novel Bi/Cu_2O/Bi Hetero-Structure Pec Solar Cell,** Science World Journal Vol. 18, No.1, pp.14-19, (2023).

[52] R.W. Berry, P.M. Hall and T. Harris, **Thin Film Technology**, New York, (1979).

[53] K.Seshan , **Handbook of Thin-Film Deposition Processes and Techniques: Principles , Methods, Equipment and Applications second edition**, Noyes / William Publications, (2002).

[54] O.S. Heavens, **Thin film physics**, John wiley and sons , New York, (1970).

[55] C. christopher ibeh, **Thermoplastic Materials Properties Manufacturing Methods, and Applications**, CRC Press Taylor and Francis Group, (2011).

[56] A. Rockett, **The Materials Science of Semiconductors,** Springer Science and Business Media, LLC, New York, (2008).

[57] H. R. Abdulridha**, High Reflectance Nanolayers Prepared from (Al-Ni-Cr) Alloy for Laser Resonator via Thermal Evaporation Technique,** M.Sc. Thesis, College of Science, University of Babylon, (2021).

[58] L. Vossen , W. Kern and W.Kern , **Thin Film Processes II**, Gulf Professional Academic press limited United Kingdom, (1991).

[59] H.R. A. Mohammed, **High Reflectance Nanolayers Prepared from (Al-Ni-Cr) Alloy for Laser Resonator via Thermal Evaporation Technique,** M.Sc. Thesis, University of Babylon, Iraq, (2020).

[60] S.Masudy-Panah, **Fabrication and Characterization of CuO Based Heterojunction Solar Cells**, Ph.D. Thesis, Nanyang Technological University, Singapore, (2015).

[61] M. Birkholz, P. F. Fewster and C.Genzel, **Thin Film Analysis by X-Ray Scattering**, WILEY-VCH Verlag GmbH and Co. KGaA, Germany, (2006).

[62] J. J. Quinn and K. S. Yi, **Solid State Physics Principles and Modern Applications**, Springer-Verlag Berlin Heidelberg, Germany, (2009).

[63] B.D.Cullity, **Elements of X-Ray Diffraction**, Addison-Wesley, Publishing Company, (1970).

[64] S.R. Elliott, **Physics of Amorphous Materials**, Long Man Group Limited, English, (1983).

[65] A. H. O. Alkhayatt and S. K. Hussian, **Fluorine Dopant Concentration Effect on the Structural and Optical Properties of Spray Deposited Nanocrystalline ZnO Thin Films**, Surf. Interfaces, Vol.8, pp.176–181, (2017).

[66] R. D. Prabu, S. Valanarasu, V. Ganesh, M.Shkir, S. Al-Faify, A. Kathalingam, S.R. Srikumare and R. Chandramohan, **An Effect of Temperature on Structural, Optical, Photoluminescence and Electrical Properties of Copper Oxide Thin Films Deposited by Nebulizer Spray Pyrolysis Technique**, Materials Science in Semiconductor Processing,Vol.74,pp.129–135, (2018).

[67] C. Kittel, **Introduction to Solid State Physics**, **8th ed.**, Wiley and Sons Inc., United State of America, (2005).

[68] T. Allen, S. Rutherford, S. Murray, S. Reipert, and M.Goldberg**, Scanning Probe and Scanning Electron Microscopy**, Elsevier Science ,USA, (2006).

[69] N. A. N. Abokhumra, **Preparation and Study the Physical Properties of ZnO Thin Films for Photodetector Applications,** Ph.D. Thesis, College of Science, University of Babylon, (2015).

[70] R. N. Jagtap and A. H. Ambre, **Overview Literature on Atomic Force Microscopy (AFM): Basics and its Important Applications for Polymer Characterization**, Indian Journal of Engineering and Materials Sciences, Vol. 13, pp. 368-384, (2006).

[71] M. Lanza, **Conductive Atomic Force Microscopy: Applications in Nanomaterials**, Wiley-VCH Verlag GmbH and Co. KGaA, Weinheim, Germany, (2017).

[72] K.L. Chopra, **Thin Film Devices Application**, Plenum Press, New York, (1983).

[73] C. Mwolfe, N. Holouyak and G. B. Stallman, **Physical Properties of Semiconductor**, Prentice Hall, New York, (1989).

[74] B.G. Stereeman, **Solid State Electronic Devices**, **2nd ed.**, Practice Hall, Inc. Engle Wood Cliffs, N.J, (1980).

[75] J.I. Pankove, **Optical Process in Semiconductors**, Dover Publishing, Inc., New York. (1971).

[76] L. Kazmarski and A. Clark, **Polycrystalline and Amorphous Thin Films and Device** , Edited by Lawrence Academic Press, New York , (1980).

[77] J. Tauce**, Amorphous and Liquid Semiconductors**, Plenum, London and New York, (1974).

[78] O. Stenzel, **The Physics of Thin Film Optical Spectra An Introduction,** springer Springer-Verlag Berlin Heidelberg , (2005).

[79] B.S.Mitchell , **An Introduction to Materials Engineering and Science for Chemical and Materials Engineers**, John Wiley and Sons, Inc., (2004).

[80] M. Fox, **Optical Properties of Solids**, Oxford University press, (2007).

[81] S.M. Sze and K.K. Ng, **Physics of Semiconductor Devices 3rded.**, John Wiley and Sons, Inc. ,(2007).

[82] D.A. Neamen**, Semiconductor Physics and Devices Basic Principles**, McGraw-Hill Companies, Inc., New York, (2003).

[83] I.M. Dharmadasa, **Advanced in Thin Films Solar Cell**, CRC Press Tayler and Frances Group, LLC.,U.S.A, (2012).

[84] P. S. Kireev, **Semiconductors Physics,** Moscow: Translated from Russian by M. Samokhvalov, MIR Puplishers, (1978).

[85] J. Poortmans and V. Arkhipov**, Thin Film Solar Cells Fabrication, Characterization and Applications,** John Wiley and Sons Ltd, England, (2006).

[86] C. Hu and R. M. White**, Solar Cells From Basics to Advanced Systems** McGraw-Hill, Inc., United State, (1983).

[87] S. Kalogirou, **Solar Energy Engineering: Processes and Systems**, Academic Press, Amsterdam, pp. 469–517, (2009).

[88] S. Bapanapalli, **CdS/CdTe Thin Film Solar Cells with Zinc Stannate Buffer Layer**, M.Sc. Thesis, College of Engineering, University of South Florida, (2005).

[89] N. Amin and T. Isaka, **Effect of Substrate Temperatures on CdSe:Sn Thin Films**, Journal Application Physics, Vol.38, p.1698 (2000).

[90] R. S. Popovic, **Hall Effect Devices**, Institute of physics publishing, Bristol and Philadelphia, (2004).

[91] H. D. Young, **University Physics**, **8th ed.,** Addison–Wesley Publishing Company, (1991).

[92] D. Bonnell, B. Huey and D. Carroll, **In-Situ Measurement of Electric Fields at Individual Grain Boundaries in TiO_2,** Solid State Ionics, Vol.75, pp. 35-42, (1995).

[93] A.J. Steckl and S.P. Sheu, **Solid state electronics**, Vol. 23, pp. 715–720, (1980).

[94] I. Z. Alferov, "**Semiconductor heterostructures** physical processes and applications" , Printed in RSSA, (1989).

[95] J. Piprek, **Semiconductor optoelectronic device: introduction to the physics and simulation**, Academic Press, San Diego, Calif, U.S.A, (2003).

[96] K.N. Jha and N.D. Taneja, **Vacuum Deposition Plant for Thin Film Circuit**, IETE Journal of Research, Vol.12, No. pp. 478-483, (1966).

[97] R. Guinebretière, **X-ray Diffraction by Polycrystalline Materials**, John Wiley and Sons, United States, (2013).

[98] S. K. Sharma, D. S. Verma, L. U.Khan, S. Kumar and S. B.Khan, **Handbook of Materials Characterization**, Springer International Publishing AG, Switzerland, (2018).

[99] R. K.M. Jasim**, Substrate Temperature Effect on Some Physical Properties of SnS Thin Films Prepared by Chemical Spray Pyrolysis,** M.Sc. Thesis, College of Science, University of Babylon, (2022).

[100] H. J. Ali, **The Electrical and Optical Properties of Annealed Cd_2SnO_4 Thin Films Prepared by Chemical Spray Pyrolysis Technique**, M.Sc.Thesis, Al-Mustansiriyah University, College of Science, Physics Departement , (2010).

[101] W. Q. Yang, A. L. Stott, and M. S. Beck, **High Frequency and High Resolution Capacitance Measuring Circuit for Process Tomography**, IEE Proc. Circuits, Devices Syst., Vol. 141, No. 3, pp. 215–219, (1994).

[102] F. A. Akgul, G. Akgul, N. Yildirim, H. E. Unalan and R. Turan, **Influence of Thermal Annealing on Microstructural, Morphological, Optical Properties and Surface Electronic Structure of Copper Oxide Thin Films**, Materials Chemistry and Physics, Vol. 147, pp. 987-995, (2014).

[103] T. Daniel, U. Uno, K. Isah and U. Ahmadu, **Tuning of SnS Thin Film Conductivity on Annealing in an Open Air Environment for Transistor Application**, East Eur. J. Phys., Vol. 2, pp. 94-103, (2020).

[104] M. Devika, N. K. Reddy, K. Ramesh,K. R. Gunasekhar, E. S. R. Gopal and K. T. R. Reddy, **Influence of Annealing on Physical Properties of Evaporated SnS Films,** Semicond. Sci. Technol., Vol. 21, pp. 1125–1131, (2006).

[105] K. Dhanabalan, A.T. Ravichandran, A.Vasuhi, R. Chandramohan, P. Karthick and S. Mantha, **Effect of Annealing Based on the Structural, Optical, Morphological and Antibacterial Activities of Copper Oxide Thin Films by SILAR Technique**, Int. J. Thin Film. Sci. Tec, Vol. 11, No. 1, pp. 65-72, (2022).

[106] Z. D.Tafti, H. Amrollahi Bioki, M. B. Zarandi, **The Effect of Annealing on the Structural and Optical Constants of SnS/ZnS Bilayer Thin Film Prepared by Vacuum Evaporation**, International journal of advanced scientific and technical research, Issue 5 Vol. 1, pp.1-20, (2015).

[107] A. Hojabri, F. Hajakbari, N. Soltanpoor and M. S. Hedayati, **Annealing Temperature Effect on the Properties of Untreated and Treated Copper Films with Oxygen Plasma**, J Theor. Appl. Phys., Vol. 8, No.132, pp.1-7, (2014).

[108] M. H. Oudah, M. H. Hasan and A. N. Abd, **Some Physical Properties of Copper Oxide Thin Films Prepared by Electrolysis Method,** World Scientific News, Vol.135, pp. 59-70, (2019).

[109] G. Wisz, P. Sawicka-Chudy, P. Potera, M. Sibiński, R. Yavorskyi, Ł. Głowa, B. Cieniek and M. Cholewa, **Morphology, Composition, Structure and Optical Properties of Thermally Annealed Cu_2O Thin Films Prepared by Reactive DC Sputtering Method,** Molecular Crystals and Liquid Crystals, Vol. 672, No.1, pp. 81–91, (2018).

[110] R. Bunea, A. K. Saikumar and K. Sundaram**, The Effect of Annealing Temperature and Reactive Gases on Optical Properties of Cu_2O Thin Films,** Materials Sciences and Applications, Vol. 12, pp. 182-196, (2021).

[111] C. Rana and S. Saha, **Growth and study of tin sulfide nanocrystals by precipitation technique using trimethylamine**, Materials Today: Proceedings , Vol.11, pp. 667–672, (2019).

[112] S. Han, K. M. Niang, G. Rughoobur, and A. J. Flewitta, **Effects of Post-Deposition Vacuum Annealing on Film Characteristics of p-type Cu_2O and its Impact on Thin Film Transistor Characteristics**, Applied Physics Letters, Vol.109, pp. 1-5, (2016).

[113] F. Yang, Y. Fan, J. Li, H. Fu, G. Xiang, W. Peng, Y. Zhou, Y. Zhao, Z. Zhen, G. Deng and H. Wang**, Effects of Oxygen Flow Rates on the Physical Characteristics of Magnetron Sputtered Single-Phase Polycrystalline Cu_2O Films**, Materials Research, Vol.23, pp.1-6, (2020).

[114] W.-J. Lee and X.-J. Wang, **Structural, Optical, and Electrical Properties of Copper Oxide Films Grown by the SILAR Method with Post-Annealing**, Coatings, Vol.11, No. 864, pp. 1-13, (2021).

[115] H.-J. Jia, S.-Y. Cheng, X.-K. Wu and Y.-L. Yang, **Effect of Anneal Temperature on Electrical and Optical Properties of SnS:Ag Thin Films**, Vol.2, No.3, pp.197-200, (2010).

[116] S S Hegde and K Ramesh, **Advances In Low-Cost And Nontoxic Materials Based Solar Cell Devices,** Journal of Physics: Conference Series,Vol. 2070,pp.1-12, (2021).

[117] S. Riazimehr, M. Belete, S. Kataria, O. Engström, and M.C.Lemme, **Capacitance–Voltage (C–V) Characterization of Graphene–Silicon Heterojunction Photodiodes**, Adv. Optical Mater., Vol.8, Issue13,pp.1-5, (2020).

[118] R. A. Ismail, **Characteristics of p-Cu_2O/n-Si Heterojunction Photodiode made by Rapid Thermal Oxidation,** , Journal of Semiconductor Technology and Science, Vol.9, No.1, pp.51-54, (2009).,

[119] M. M. Hassan, M. A. Fakhri, S. A. Adnan**, Structural Electrical and Detection Properties of Copper Oxide Based on Optoelectronic Device,** Materials Science and Engineering, Vol. 454, pp.1-7, (2018).

[120] M. Sugiyama, K.T.R. Reddy, N. Revathi, Y. Shimamoto , Y. Murata, **Band Offset of SnS Solar Cell Structure Measured by X-ray Photoelectron Spectroscopy**, Thin Solid Films, Vol. 519, pp. 7429–7431, (2011).

[121] M. Fathy, S. Elyamny , A. A. Bishara, G.D. Roston, and A. B. Kashyout, **SnS Nanocrystalline Thin Films for n-CdS/p-SnS Solar Cell Devices,** J Mater Sci: Mater Electron ,Vol.31, pp.18120–18134,(2020).

[122] R. Jaramillo, V. Steinmann, C. Yang, K. Hartman, R. Chakraborty, J. R. Poindexter, M. L. Castillo, R. Gordon, T. Buonassisi, **Making Record-efficiency SnS Solar Cells by Thermal Evaporation and Atomic Layer Deposition,** Journal of Visualized Experiments, Vol.99, pp.1-20, (2015).

الخلاصة

في هذا العمل تم تحضير أغشية Cu_2O وSnS وCu_2O/SnS و $Cu_2O:SnS$ الرقيقة على ركائز من الزجاج والسليكون بتقنية التبخير الحراري وتحت ضغط (1×10^{-7}) mbar ولدنت بدرجة حرارة 200 درجة مئوية ولمدة ساعتين. تم دراسة وتحليل الخصائص التركيبية والبصرية والكهربائية للأغشية المحضرة قبل وبعد عملية التلدين.

نتائج حيود الأشعة السينية (XRD) تشير إلى ان تركيب جميع الأغشية الرقيقة المحضرة هي متعددة التبلور وان أغشية Cu_2O الرقيقة تمتلك طور مكعب (Cubic) وان أغشية SnS الرقيقة لها طور (Orthorombic) .وجد ان قيمة معدل الحجم البلوري لأغشية Cu_2O الرقيقة تزداد من (12إلى 16) نانومتر كما يمكن ملاحظة وجود انخفاض في معدل الحجم الحبيبي لباقي الاغشية حيث انخفضت من (14 إلى13) نانومتر و (14 إلى 11) نانومتر و (16 إلى 12) نانومتر لأغشية SnS و Cu_2O/SnS و$Cu_2O:SnS$ الرقيقة على التوالي.

صور المجهر الالكتروني الماسح لانبعاث المجال(FESEM) لأغشية Cu_2O الرقيقة تشير إلى إن حجم الجسيمات (البلورات) يزداد بعد عملية التلدين بينما تقل لاغشية SnS وCu_2O/SnS و$Cu_2O:SnS$ الرقيقة . إن طبوغرافية سطح الأغشية الرقيقة يبدو ناعم نسبيا ومطلي بانتظام وأظهرت نتائج مجهر القوة الذرية (AFM) ان سطح الاغشية المحضرة على أرضية من الزجاج ذات بنية سطح صقيله.

سجلت أطياف معامل الامتصاص والنفـاذية في مدى الطول الموجي (300-1100) نانومتر والتي أظهرت أن حافة الامتصاصص لأغشية Cu_2O الرقيقة أزيحت نحو الاطوال الموجية الأطول بزيادة درجة الحرارة بعد عملية التلدين. كما ان حافات الامتصاص لأغشية SnS وCu_2O/SnS و$Cu_2O:SnS$ الرقيقة أزيحت نحو الاطوال الموجية الأقصر.

ان فجوة الطاقة للانتقال المباشر المسموح لأغشية Cu_2O المحضرة انخفضت من (2.57 إلى 2.15) الكترون فولت بعد التلدين عند 200 درجة مئوية بينما زادت قيمة فجوة الطاقة لاغشية SnS من (1.53إلى 1.8) الكترون فولت و قيمة فجوة الطاقة لأغشية

Cu_2O/SnS ازدادت من (1.75 إلى 1.80) الكترون فولت بعد عملية التلدين كما ان فجوة الطاقة لأغشية $Cu_2O : SnS$ الرقيقة ازدادت من (3.66 إلى 3.86) الكترون فولت على التوالي. بالإضافة الى ذلك تم دراسة تأثير التلدين على الثوابت البصرية (كمعامل الامتصاص ومعمل الخمود). نتائج قياسات هول تباينت ما بين الزيادة والنقصان لمعلمات هول كتركيز حاملات الشحنة ومعامل هول والتحركية بعد عملية التلدين.

ان خصائص سعه - جهد بينت ان المفرق الهجين من (النوع الفجائي) وان أعلى قيمة لجهد البناء الداخلي كانت للخلية الشمسية SnS/Si بمقدار(0.21) فولت. تم قياس خصائص تيار- جهد (I-V) للخلايا الشمسية عند الاضاءة عند الشدة ($100\ mW/cm^2$) حيث بينت النتائج ان مقدار كفاءة الخلية الشمسية $Cu_2O/n\text{-}Si$ هو%(3.37) اما الخلية الشمسية $SnS/n\text{-}Si$ و$Cu_2O/SnS/n\text{-}Si$ لها كفاءة بمقدار %(6.27) و%(4.62) على التوالي. اما اعلى قيمة لكفاءة الخلية الشمسية كانت لنموذج $Cu_2O:SnS/n\text{-}Si$ بمقدار

% (7.44) وقيمة تيار الدائرة القصيرة كان (24) ملي امبير و وكانت فولتية الدائرة المفتوحة (500) ملي فولت ومقدارعامل الملئ 0.99.

جمهورية العراق
وزارة التعليم العالي والبحث العلمي
جامعة بابل/ كلية العلوم
قسم الفيزياء

تصنيع خلية شمسية متعددة الطبقات على ركيزة n-Si

أطروحة مقدمة إلى مجلس كلية العلوم في جامعة بابل وهي جزء من متطلبات نيل درجة دكتوراه فلسفة في الفيزياء

من قبل

ايناس عبدالله زغير طه

بكالوريوس علوم فيزياء ٢٠٠٥

ماجستير علوم فيزياء ٢٠١٥

بإشراف

الأستاذ الدكتور
عبد العزيز عبيد موسى العكيلي

الأستاذ الدكتور
خالد حنين عباس حسن

١٤٤٥هـ

٢٠٢٣م